Sigurdsson, H., Leckie, R.M., Acton, G.D., et al., 1997
Proceedings of the Ocean Drilling Program, Initial Reports, Vol. 165

6. SITE 1001[1]

Shipboard Scientific Party[2]

HOLE 1001A

Position: 15°45.427′N, 74°54.627′W (lower Nicaraguan Rise)

Date occupied: 0745 hr, 2 February 1996

Date departed: 0030 hr, 8 February 1996

Time on hole: 136.75 hr (5 days, 16 hr, 45 min)

Seafloor depth (drill-pipe measurement from rig floor, mbrf): 3271.0

Total depth (drill-pipe measurement from rig floor, mbrf): 3793.8

Distance between rig floor and sea level (m): 11.4

Water depth (drill-pipe measurement from sea level, m): 3259.6

Penetration (mbsf): 522.8

Coring totals:
Type: RCB; No: 56; Cored: 522.80 m; Recovered: 286.23 m (54.8%)

Formation:
Clayey nannofossil mixed sediment and ooze; calcareous chalk with clay; chert; limestone with clay; basalt

Oldest sediment cored:
Depth (mbsf): 485.0
Nature: Limestone with clay and ash
Age: middle Campanian

HOLE 1001B

Position: 15°45.418′N, 74°54.626′W (lower Nicaraguan Rise)

Date occupied: 0030 hr, 8 February 1996

Date departed: 0145 hr, 11 February 1996

Time on hole: 72.75 hr (3 days, 45 min)

Seafloor depth (drill-pipe measurement from rig floor, mbrf): 3271.0

Total depth (drill-pipe measurement from rig floor, mbrf): 3759.3

Distance between rig floor and sea level (m): 11.6

Water depth (drill-pipe measurement from sea level, m): 3259.4

Penetration (mbsf): 488.3

Coring totals:
Type: RCB; No: 32; Cored: 301.20 m; Recovered: 201.14 m (66.8%)

Formation:
Clayey nannofossil mixed sediment and ooze; calcareous chalk with clay; chert; limestone with clay; basalt

Oldest sediment cored:
Depth (mbsf): 485.6
Nature: Limestone with clay and ash
Age: middle Campanian

Principal results: Site 1001 is located in an area of the lower Nicaraguan Rise where the Neogene sediments are thin, and where a continuous Upper Cretaceous–Paleogene sedimentary sequence overlying basaltic basement was expected. The interval between the widespread Caribbean seismic reflectors A″ (lower Eocene cherts) and B″ (Upper Cretaceous basalt) had been cored, but poorly recovered at Deep Sea Drilling Project (DSDP) Site 152, located ~40 km to the east-northeast, at the base of the Hess Escarpment (Edgar, Saunders, et al., 1973). At a water depth of 3259 m, Site 1001 is 640 m shallower than Site 152; it is located on the Hess Escarpment. The principal objectives at Site 1001 were (1) to recover a complete Cretaceous/Tertiary (K/T) boundary sequence, (2) to address topics of ancient ocean paleoceanography, including the tropical record of the late Paleocene thermal maximum (LPTM) and the nature of orbital forcing during the Maastrichtian and Paleocene, and (3) to recover igneous basement and test models of the formation of the Caribbean Oceanic Plateau. Most of the Paleogene and Cretaceous section was double-cored, including the conformable basalt/limestone contact. Basalt of probable mid-Campanian age (~77 Ma) was penetrated at 485.4 mbsf and 37.4 m of the basalt was cored.

A 165.7-m Neogene section, spanning the middle Miocene to Pleistocene, is separated from the underlying Paleogene–Cretaceous section by a pair of unconformities in Section 165-1001A-18R-4. Middle Miocene nannofossil ooze unconformably overlies 28 cm of middle Eocene chalk. A second unconformable contact is marked by a chert layer where the thin middle Eocene chalk overlies lower Eocene chalk. The duration of these hiatuses is approximately 30 and 8 m.y., respectively.

Four lithologic units are recognized at this site. Unit I is divided into four subunits: Subunit IA (6.4–112.2 mbsf; Pleistocene–upper Miocene) consists of clayey nannofossil mixed sediment to nannofossil ooze with clay. Subunit IB (112.2–131.7 mbsf; upper Miocene) is a clayey nannofossil ooze with foraminifers and is marked by a sharp increase in carbonate content and increased induration. Subunit IC (131.7–153.2 mbsf; upper–middle Miocene) is composed of nannofossil ooze with clay to nannofossil clay and is distinguished from the intervals above and below by the highly variable carbonate contents and magnetic susceptibility. Subunit ID (153.2–165.7 mbsf; middle Miocene) contains nannofossil ooze with clay to clayey nannofossil ooze; this interval is distinctly more carbonate-rich than Subunit IC and has much lower and less variable values of magnetic susceptibility.

Lithologic Unit II corresponds with the Paleocene–Eocene section. The distribution of chert is the principal feature used to divide Unit II into two subunits. Subunit IIA (165.7–304.6 mbsf; middle and lower Eocene–upper Paleocene) is primarily composed of calcareous chalk with foraminifers to mixed sedimentary rock with clay. This subunit is interbedded with numerous chert and volcanic ash layers. Subunit IIB (304.6–352.1 mbsf; upper–lower Paleocene) lacks the cherts of Subunit IIA; is more clay-rich, especially in the lower Paleocene; and is further distinguished by the presence of thin interbedded foraminiferal-rich sand layers. The dominant lithologies of Subunit IIB are calcareous chalk with clay to claystone and some ash layers.

The K/T boundary interval was recovered in Holes 1001A and 1001B (Sections 165-1001A-38R-CC and 39R-1; Section 165-1001B-18R-5). Comparison of the Formation MicroScanner (FMS) data and the recovered sediments indicates that 15–20 cm of the boundary deposit may not have been recovered. Remarkably, however, several clay-rich units between the basal Paleocene and upper Maastrichtian limestones were re-

[1]Sigurdsson, H., Leckie, R.M., Acton, G.D., et al., 1997. *Proc. ODP, Init. Repts.,* 165: College Station, TX (Ocean Drilling Program).
[2]Shipboard Scientific Party is given in the list preceding the Table of Contents.

covered. A 1.7- to 4.0-cm, light gray, highly indurated limestone of earliest Paleocene age (planktonic foraminifer Zone P0/Pα, undifferentiated), similar to the limestone recovered earlier at Site 999, overlies the package of clay-rich strata constituting the bulk of the recovered boundary deposit at Site 1001. The topmost layer of the boundary deposit is a 3.5-cm-thick, massive clay. This unit contains rare grains of shocked quartz and overlies a 3.5-cm-thick smectitic claystone with dark green spherules. The spherules are up to 2 mm in diameter and may represent altered tektites from the K/T impact event. The base of the boundary deposit is a 1- to 2-cm-thick smectitic clay layer with shaly cleavage. This clay contains light-colored speckles, up to 1 mm in diameter. In addition to these three distinctive clay layers, two loose pieces of polymict micro-breccia were recovered from the top of Core 165-1001A-39R. These contain angular clasts (<6 mm) of claystone and limestone in an unconsolidated matrix of smectitic clay. This lithology may represent fragments of a thicker poorly recovered unit at this site. The total boundary deposit has an inferred thickness of approximately 25 cm at this location.

The Upper Cretaceous sedimentary section is represented by lithologic Unit III, which is divided into two subunits. A marked increase in carbonate content delimits the change from lower Paleocene mixed sedimentary rocks and claystones to Maastrichtian limestone. Subunit IIIA (352.1–472.9 mbsf; basal Paleocene–mid-Campanian) consists of calcareous limestone and claystone with interbedded foraminiferal-rich sand layers. Ash layers become thicker and more frequent in the lower part of Subunit IIIA. Subunit IIIB (472.9–485.4 mbsf; mid-Campanian) is characterized by a significant reduction in carbonate content and a dramatic increase in the abundance of altered volcaniclastic material, including common andesitic to silicic ash fall layers and several thick ash turbidites. The lower part of this unit contains angular to subangular fragments of basaltic lapilli and hyaloclastite breccia that grade downcore into a conformable basement contact consisting of sediment-poor basaltic lapilli and basalt.

Lithologic Unit IV (485.4–522.8 mbsf; mid-Campanian), the igneous basement, consists of a succession of 12 formations, which likely represent individual pillow lavas and sheet flows. Some of the flows have thick hyaloclastite breccia tops and massive columnar interiors.

Several lines of evidence support the hypothesis that the volcanic edifice cored at Site 1001 subsided rapidly in mid-Campanian time. Vesicles in the basalt are relatively large, suggesting water depths significantly shallower than the present. Benthic foraminifers from limestone lenses between the basalt flows suggest outer neritic to upper bathyal paleodepths, whereas a rapidly deepening-upward trend is suggested on the basis of benthic foraminifer assemblages in the overlying limestones and ash turbidites. In addition, the volcanic edifice was likely located near the paleoequator as suggested by the very shallow paleomagnetic inclinations obtained from the basalt and overlying sediments.

A carbonate-poor, clay-rich interval in the uppermost Paleocene is very similar to a correlative interval cored at Site 999. Both sites contain volcanic ash layers within the distinctive laminated to weakly bioturbated deposit. We attribute the character of this interval to the rapid and short-lived oceanographic changes of the LPTM. The interval was cored and recovered twice at Site 1001 (Sections 165-1001A-27R-2 and 165-1001B-6R-3).

Ash layers representing three episodes of volcanism in the Caribbean were found in the Paleogene–Upper Cretaceous of Site 1001. One episode in the latest Paleocene–early Eocene time is likely related to the explosive volcanism documented at Site 998 and attributed to the Cayman Ridge arc. A second smaller peak of volcanism occurred in the early Paleocene, and it is perhaps contemporaneous with the activity recorded at Site 999 on the Kogi Rise and attributed to the Central American arc. A third short-lived episode occurred in mid-Campanian time, perhaps associated with the activity of central volcanoes on the Caribbean Oceanic Plateau.

The middle/upper Miocene boundary interval at Site 1001 is distinguished by highly variable carbonate contents and magnetic susceptibility, and correlates with the "carbonate crash" interval recognized at Sites 998, 999, and 1000. However, in contrast with these earlier sites, the interval of reduced carbonate values persists about 1 m.y. longer at Site 1001.

BACKGROUND AND OBJECTIVES

Site 1001 is located on the Hess Escarpment, a strikingly linear, 1000-km-long tectonic feature that separates the lower Nicaraguan Rise from the Colombian Basin (Fig. 1). The site is approximately 40 km west-southwest of DSDP Site 152, which penetrated a Paleogene and Upper Cretaceous sedimentary section and basaltic basement, but yielded poor core recovery. Site 1001 was selected for drilling in part because of the thin Neogene sediment cover, as it offers an opportunity to recover well-preserved Paleogene sediments at relatively shallow depths, as well as the opportunity to recover a K/T section and igneous basement that may represent the Caribbean Oceanic Plateau (Edgar, Saunders, et al., 1973; Holcombe et al., 1990).

The relief of the northeast-trending Hess Escarpment ranges up to 3 km. Major erosional channels and embayments, associated with sediment transport from the lower Nicaraguan Rise into the Colombian Basin, incise the escarpment. Estimates of the age of the Hess Escarpment vary: Burke (1988) and Burke et al. (1984) considered the escarpment as the active northern strike-slip boundary of the Caribbean Plate in the Campanian (~80 Ma), with left-lateral movement between the Nicaraguan Rise and the Caribbean Plate, whereas Pindell and Barrett (1990) place initiation of movement much later, at about middle Eocene time (~49 Ma). Case and Holcombe (1977) proposed that a diffuse zone of rifting and related volcanism has existed between the Hess Escarpment and the Pedro Fracture Zone on the Nicaraguan Rise since the Miocene, and that this has been a zone of intra-plate deformation. Recent single-channel seismic surveys provide new evidence of the timing of motion on the Hess Escarpment. They show that the faulting that generated the escarpment must have began between B″ and A″ (i.e., between 80 and 49 Ma), based on the occurrence of a sediment-filled, faulted half-graben at the base of the escarpment (see "Seismic Stratigraphy" section, this chapter). Because Site 1001 is located on an intermediate shelf on the escarpment, it provides an opportunity to date local tectonic activity, as indicated by hiatuses or other evidence in the sedimentary record.

Basement drilling at Site 1001 has the potential of addressing some paradoxical findings at DSDP Site 152. Basalts recovered at that site were described as weathered, altered, and highly vesicular and amygdaloidal (Edgar, Saunders, et al., 1973), which are all features typical of lava flows. Yet the lower Campanian limestone occurring with the basalt was described as being metamorphosed, and limestone that occurs within the basalt was described as xenoliths. On the basis of these features, the basalt was described as being of Campanian age, which gave rise to the idea of an igneous episode on the Caribbean Plate postdating the main outpouring of the Large Igneous Province by 8–10 m.y. (Donnelly et al., 1990). Because of the proximity of Sites 152 and 1001, the recovery of a substantial basement section could provide an important test of the age relations between basement and the overlying sediments on this part of the Caribbean Oceanic Plateau as well as provide information about the mode of emplacement of the basalts.

Basalts recovered at DSDP Site 152 have a somewhat unusual chemical composition when compared with other basalts analyzed from the Caribbean Oceanic Plateau (Donnelly et al., 1973). They are relatively light-rare-earth depleted, unlike the mid-ocean ridge basalt (MORB) -like and flat rare-earth element pattern exhibited by the other basalts recovered on Leg 15, possibly suggesting different mantle reservoirs. The Site 152 basalts are also enriched in K, Th, and Rb, but this feature could be attributed to their relatively high state of alteration.

Site 1001 is approximately 380 km southwest of Haiti, where one of the best K/T boundary sections occurs in the Beloc region of the

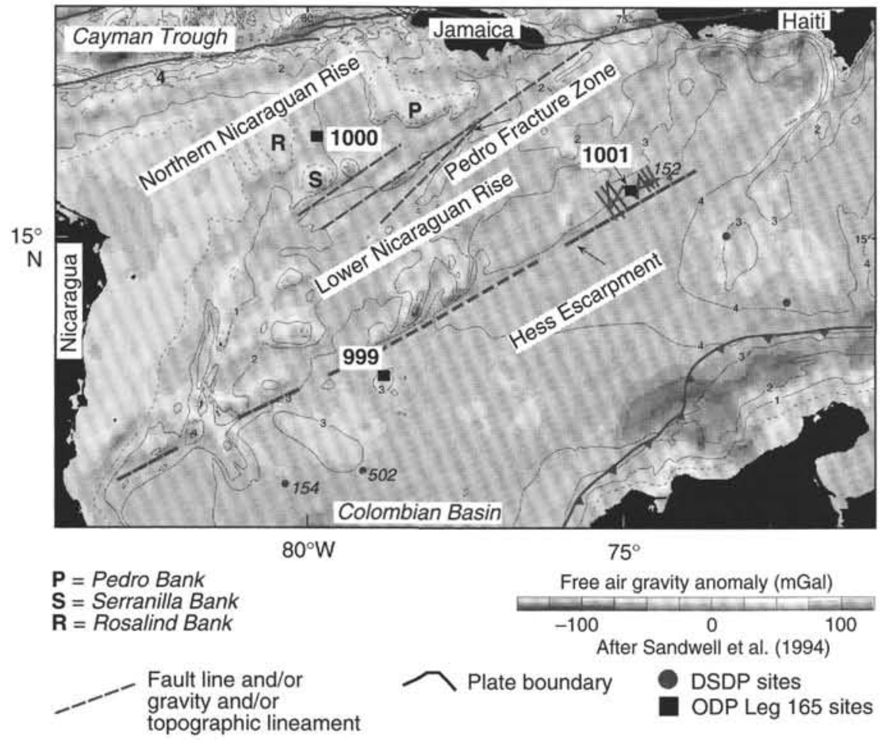

Figure 1. General map of the western Caribbean (Rosencrantz, unpubl. data; also Droxler et al., 1995), Colombian Basin, and Nicaraguan Rise, clearly separated by the Hess Escarpment. Locations of Site 1001, as well as Sites 999 and 1000, are shown. The extent of the *Maurice Ewing* 9417 site survey is also indicated in the northeast corner of the Colombian Basin.

southwest peninsula, with an ejecta deposit up to 1 m in thickness and containing well-preserved impact glass spherules (Sigurdsson et al., 1991). Both the Beloc section and Site 1001 were located southeast of the Chicxulub crater at the time of impact, probably 800–900 km from the source. In the Haiti sections, three sedimentary units are present: a basal impact glass spherule ballistic fallout unit, overlain by a gravity flow deposit with tektites and sediment rip-up clasts, and at the top an iridium-rich smectitic clay unit of late-stage fallout material.

Drilling at DSDP Site 152 demonstrated that pelagic carbonate sedimentation mixed with only minor amounts of clay was the dominant sediment type from the Campanian to the early Eocene in this region of the Caribbean. The carbonate content remains high (>80%) throughout the Late Cretaceous and into the Paleogene (Edgar, Saunders, et al., 1973), suggesting that the sediments were deposited above the lysocline, and that the sediments were deposited at depths shallower than in the adjacent basins. This site has been described as richest in carbonates and as including the best preserved and most diverse early Paleogene–Late Cretaceous planktonic foraminifer assemblages obtained in the Caribbean area (Premoli Silva and Bolli, 1973). Because of the relatively great age of the cored succession and its location, Site 1001 also has the potential of extending the record of volcanic ash fallout in the Caribbean, both in time and in space, as the site is located farther east from the putative Central American sources than other sites drilled during Leg 165.

SEISMIC STRATIGRAPHY

Site 1001 is located at 15°45.4′N, 74°54.6′W in 3259.6 m of water depth on the rim of the Hess Escarpment, which defines the extreme southeastern edge of the lower Nicaraguan Rise, about 250 km south of Haiti. Site 1001 was drilled about 35 km west-southwest of DSDP Site 152, which is located at the base of the Hess Escarpment at a water depth of 3899 m, about 640 m deeper than Site 1001 (Fig. 1).

The Hess Escarpment is a 1000-km, northeast-trending, linear, prominent bathymetric break that separates the lower Nicaraguan Rise from the adjacent Colombian Basin (Fig. 1). Holcombe et al. (1990) have interpreted the Hess Escarpment to represent a Late Cretaceous, very early deformation event within the Caribbean's history, whereas Burke et al. (1984) have postulated left-lateral movement along the Hess Escarpment as the Caribbean Basin crust and the Nicaraguan Rise translated between the Yucatan block and South America from 80 to 53 Ma. The Hess Escarpment is also commonly thought to represent a major strike-slip fault related to Tertiary Caribbean tectonics (Holcombe et al., 1990).

Although the lower Nicaraguan Rise is relatively poorly surveyed, it is characterized as a region of highly variable relief and has a complex history that involves extensive deformation, including faults, ridges, troughs, and young volcanoes (La Providencia and San Andres Islands). On the basis of the overall depth of the lower Nicaraguan Rise and on evidence from seismic refraction, the crust has been regarded as of oceanic origin, similar to the crust in the Colombian Basin to the south (Ewing et al., 1960; Edgar et al., 1971; Holcombe et al., 1990). It was probably formed in the Pacific Ocean during the Mesozoic (~88 Ma) as an oceanic plateau associated with the Galapagos hot spot; thus, its character is fundamentally different than the northern Nicaraguan Rise (NNR; Holcombe et al., 1990). The highly disturbed character of this province may be the result of wrench faulting between the stable NNR to the northwest along the Pedro Fracture Zone and the Colombian Basin crust to the south along the Hess Escarpment (Holcombe et al., 1990; Fig. 1).

Before drilling began at Site 1001, the sediment cover and basement of the lower Nicaraguan Rise had only been recovered by short piston cores and dredges. DSDP Site 152, although it was not drilled on the lower Nicaraguan Rise itself, but on the base of the Hess Escarpment, was used before Leg 165 to estimate the nature, composition, and age of the basement and the sediment cover of the lower Nicaraguan Rise. At Site 152, 471.5 m of sedimentary cover was penetrated and partially cored before drilling 7 m of basaltic basement (Edgar, Saunders, et al., 1973; Fig. 2). The 59 m of sediments and rocks recovered at Site 152 yield a general stratigraphic and sedimentologic evolution of the area and some information regarding the nature of the basement. The sediment cover consists dominantly of for-

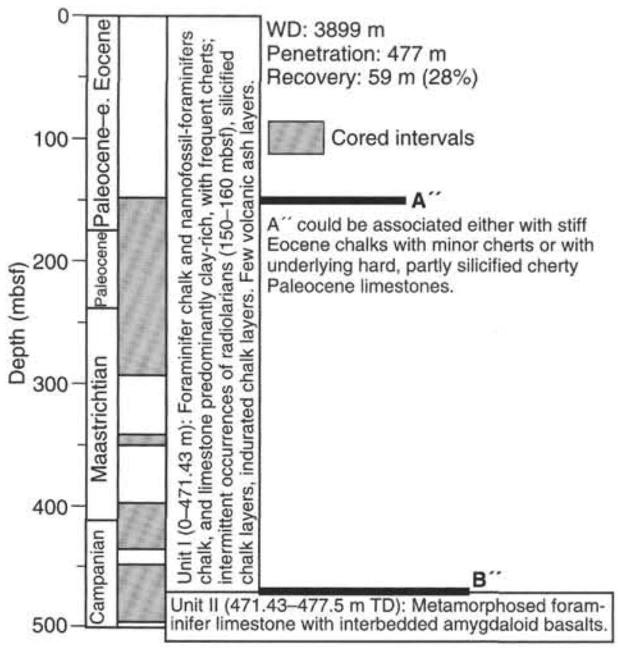

Figure 2. Stratigraphic and lithologic description of DSDP Site 152, illustrating the relationship between the two major Caribbean reflectors A″ and B″ and the lithology recovered at DSDP Site 152.

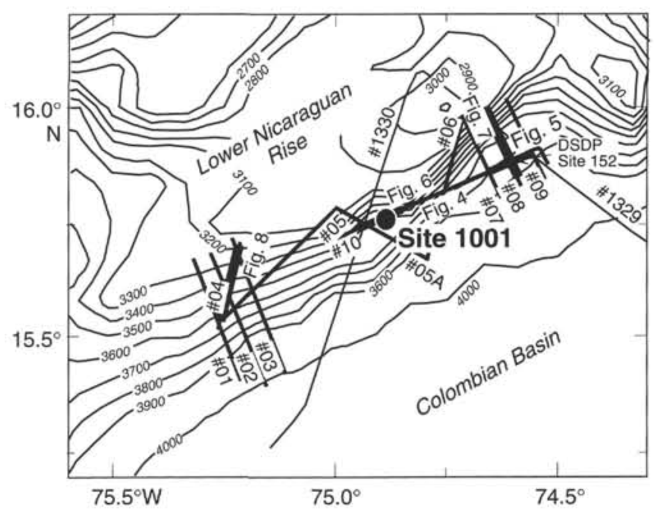

Figure 3. Track chart of two recent seismic surveys by the *Maurice Ewing* (EW9417 and EW9501). Site 1001 and DSDP Site 152 are located on or in close proximity to single-channel Lines E9417-10, 08, and 5A and two multichannel seismic lines, EW9501-1329 and 1330. Site 1001 is situated on a shoulder in the upper part of the Hess Escarpment, 35 km south-southwest relative to DSDP Site 152, where reflectors A″ and B″ were clearly identified and covered by a relatively thin Neogene sedimentary sequence.The locations of seismic lines illustrated in Figures 4 through 8 are also shown.

aminiferal chalks, nannofossil foraminiferal chalks, well-indurated chalk layers, clay-rich limestones, and intermittent occurrences of radiolarian-rich chalks with cherts, silicified chalk and limestone layers, and a few ash layers. The basement was described as "metamorphosed" foraminiferal limestones with interbedded amygdaloidal basalts. The sediment record extends from the Campanian to at least the middle Tertiary; it includes the important basinwide seismic reflector A″ (Edgar, Saunders, et al., 1973), which could be associated with either stiff Eocene chalks with minor chert or with hard partially silicified cherty Paleocene limestones. The other basinwide reflector, B″, was associated with the contact between basaltic basement and Campanian pelagic limestones. Both of these important Caribbean reflectors have been identified earlier on seismic lines in this area of the Hess Escarpment.

The Site 1001 area (the Hess Escarpment, lower Nicaraguan Rise) was surveyed with a grid of digital SCS, Hydrosweep swath bathymetry, analog 3.5-kHz, gravity, and magnetic data during a transit of the *Maurice Ewing* cruise EW9417 from Panama to Tampa at the end of 1994 (Fig. 3; "Underway Geophysics and Pre-Site Surveys" section, "Explanatory Notes" chapter, this volume; Droxler, 1995; Droxler et al., 1995). A regional multichannel seismic, gravity, magnetic, and Hydrosweep survey of the Venezuelan Basin, Beata Ridge, and Hess Escarpment was conducted aboard the *Maurice Ewing* cruise EW9501 during February and March 1995 (Diebold et al., 1995). Two lines (1329 and 1330) crossed the Hess Escarpment within 3 and 5 km of Site 1001 and DSDP Site 152, respectively, and intersected SCS lines collected during EW9417 (Fig. 3).

Bathymetric data using Hydrosweep across the Hess Escarpment illustrates the high degree of erosion that has occurred along the escarpment itself (Droxler et al., 1995). Its overall regional linearity disappears within the local morphology. Irregular, mostly west-northwest- and north-northwest-trending deep canyons and valleys dissect the northeast-trending bathymetric break of the Hess Escarpment. Also for the first time, the DSDP Site 152 location is clearly visualized within one of the reentrant canyons on a little terrace along a steep north-northeast-trending slope, oriented with a 45° angle to the northeast direction of the Hess Escarpment.

High-resolution seismic profiles, collected across and along the Hess Escarpment, clearly imaged the two prominent Caribbean reflectors B″ and A″ (Figs. 4–7). As mentioned above, drilling results at Site 152 (Edgar, Saunders, et al., 1973) show that B″ corresponds to the top basalt flows, interlayered with "metamorphosed" Campanian foraminiferal limestones, and that A″ corresponds to either Eocene chalks with minor cherts or hard, partly silicified cherty Paleocene limestones (Fig. 2). The seismic unit bounded between B″ and A″ is characterized by high-amplitude parallel reflectors in the zone south-southwest of Site 152 and by relatively transparent, high-frequency seismic facies in the area of Site 152. This latter seismic facies was partially recovered in Site 152; it appears to correspond to a relatively unaltered Paleogene and Upper Cretaceous sedimentary section and, as in the Colombian and Venezuelan Basins, it seems to be composed mostly of pelagic limestones, chalks, and clays deposited in an open-marine environment. Both main reflectors A″ and B″ are displaced within the area of the survey by as much as 0.6 to 1.2 s two-way traveltime (TWT) along a series of faults that have directly influenced the complex morphology of the seafloor (Figs. 4–8). Sets of west-north-west-, north-northwest-, and north-northeast-trending faults are observed on seismic profiles. Their orientation is estimated when faults in the sub-seafloor correspond to major relatively linear bathymetric features on the Hydrosweep maps. Faults appear to be subvertical on the interpreted seismic lines because of the high vertical exaggeration (11×) of the seismic profiles (Figs. 4–8). Both reflectors B″ and A″ are observed at the base and on the rim of the Hess Escarpment and, therefore, extend at least as far as the margin of the lower Nicaraguan Rise.

The location of Site 1001 was selected, based on the interpretation of SCS Lines EW9417-10 and EW9417-5A, at shotpoint 1500 on SCS Line EW9417-10, 2.5 km northeast of the crossing between SCS Line EW9417-10 with EW-9417-5A, and multichannel seismic Line EW9501-1330 (Figs. 3, 9). Site 1001 is situated on a shoulder in the upper part of the Hess Escarpment, 35 km south-southwest relative to DSDP Site 152, where both A″ and B″ were clearly identified and covered by a relatively thin Neogene sedimentary sequence (Figs. 4–6). Site 1001 is located on the northern side of a canyon, a tributary to a larger north-northwest-trending canyon, dissecting the upper reaches of the Hess Escarpment (Fig. 9). Examination of SCS Line

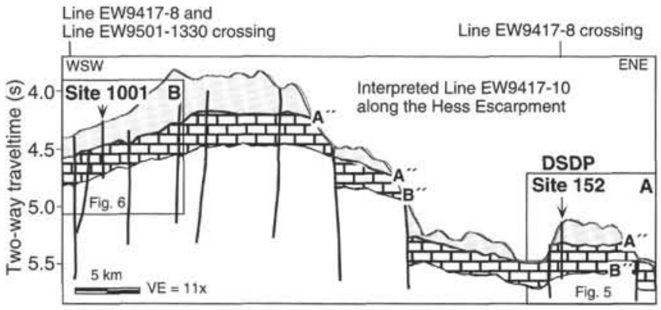

Figure 4. Interpretation of single-channel seismic Line E9417-10, joining Site 1001 and to the east-northeast DSDP Site 152, along the orientation of the Hess Escarpment. Note the almost constant thickness of seismic Unit B (Campanian to middle Eocene in age), defined between reflectors B″ and A″. Detailed interpretation of portions of Line EW9417-10 in the vicinity of DSDP Site 152 and Site 1001 are shown in Figures 5 and 6. VE = vertical exaggeration.

EW9417-10, which crosses Site 1001, reveals three distinct seismic units (Figs. 4, 6), defined by the occurrence of the two major Caribbean reflectors A″ and B″. At Site 1001, seismic Unit A extends from the seafloor at 4.275–4.490 s TWT (Reflector A″). Seismic Unit B extends from 4.490 to 4.720 s TWT (Reflector B″). Reflector A″, separating Unit B from overlying Unit A, is characterized by a clear set of continuous high-amplitude reflections. The thickness of Unit A varies greatly within the survey area. Unit A is the thickest on the upper rim of the Hess Escarpment in the areas between canyons and gullies, but relatively thin, and in some cases nonexistent, within the canyon and gully floor and along steep cliffs and slopes, where the underlying Unit B crops out (Fig. 7). In contrast, the thickness of Unit B remains relatively constant in the area between Site 1001 and DSDP Site 152 and this observation is well illustrated in Line EW-9417-10 along the Hess Escarpment (Fig. 4) and in Line EW-9417-8 across the Hess Escarpment (Fig. 7). The increasing sedimentary thickness in the upper half of Unit B along a growth fault in a large north-northwest-trending graben in the area west-southwest of Site 1001 is an exception to the relatively constant thickness of Unit B (Fig. 8).

On Line EW9417-10 in the area of Site 1001, the seismic character of Unit A differs on both sides of a fault that displaces the seafloor and separates the base of the canyon fill on its west-southwest side from the canyon slope on its east-northeast side. The canyon fill is characterized by two packages of transparent seismic facies, separated by a package of irregular higher amplitude reflections (Fig. 6). On the other hand, the canyon slope through which Site 1001 was drilled is characterized by a drapelike facies with subparallel high-frequency reflections mimicking the morphology of the seafloor. This drape facies covers a series of three wedgelike seismic packages defined farther to the east-northeast of Site 1001 on Line E9417-10, and pinches out toward the site (Fig. 6). These three seismic packages have been faulted and folded along with the underlying seismic Units B and C, and were subject to intense erosion. The second of these three packages might be represented by a thin slump deposit at Site 1001 (see "Lithostratigraphy" section, this chapter), squeezed between the drape facies of Unit A and the underlying Unit B.

Unit B extends from 4.490 (Reflector A″) to 4.720 (Reflector B″) s TWT and is characterized by a seismic package of well-defined, high-amplitude, parallel reflectors. The Unit B thickness (230 ms) remains somewhat constant, and its seismic facies relatively uniform, throughout the entire survey in the region between Site 1001 and DSDP Site 152, though the strong, well-developed parallel reflectors at Site 1001 become slightly weaker and somewhat more transparent in the area adjacent to Site 152. Unit B is strongly faulted and somewhat folded. Subvertical faults displace Unit B and underlying Unit C (basement).

Unit C is defined as the basement from the overlying Unit B by a set of one to two very high-amplitude, laterally continuous reflectors (B″). Although Unit C behaves in most of the survey area like an acoustic basement in the high-resolution single seismic E9417 lines, internal, very high-amplitude reflections within Unit C are still observed.

At Site 1001, seismic Unit A corresponds to 165.7 m of Pleistocene to middle Miocene pelagic oozes (lithologic Unit I; see "Lithostratigraphy" section, this chapter). Seismic Unit B corresponds to 186.4 m of middle Eocene to lower Paleocene calcareous chalks with some chert (lithologic Unit II), and 133.3 m of basal Paleocene to mid-Campanian (including a stratigraphically complete K/T boundary in the upper most of part of the unit) clayey calcareous limestones, calcareous limestones, and clayey mixed sedimentary rock (lithologic Unit III). Reflector A″ corresponds to the downhole transition from ooze to chalk (fully recovered) and coincides with an erosional unconformity, which brings overlying middle Miocene nannofossil ooze with clays directly in contact with middle and lower Eocene calcareous chalk with nannofossils and clays. Reflector B″, the lower contact of seismic Unit B (or lithologic Subunit IIIB) corresponds to the transition from volcanic basement into sedimentary rocks (see "Lithostratigraphy" and "Igneous Petrology and Volcanology" sections, this chapter). Reflections observed within the upper part of seismic Unit C may correspond to stratified complexes of different lava flows.

Based upon the initial interpretation of the high-resolution seismic grids and Hydrosweep data and their integration with the drilling results at DSDP Site 152 and especially at Site 1001, our observations demonstrate that continuous faulting has occurred along the Hess Escarpment since the Late Cretaceous. Some tectonic activity is also very recent, since in many instances, faults displaced the seafloor. As shown on Line EW9417-08 (Fig. 8), faulting was active during the deposition of sediment in a faulted half graben between reflectors B″ (~80 Ma) and A″ (~53 Ma). In addition, because the A″ and B″ reflectors are faulted in most of the seismic lines, the last tectonic activity along these faults had to be younger than ~53 Ma, possibly as young as early Miocene, because the sedimentary sequence draping the major unconformity (A″) at Site 1001 is middle Miocene in age. An early Miocene tectonic phase in the Caribbean is certainly compatible with the major episode of Central American Arc volcanism that was observed at Sites 998, 999, and 1000, which peaked at 18–19 Ma. Also, because the seafloor topography appears to be highly influenced by faulting, the tectonic overprint is expected to be rather recent. Although the tectonic activity has slowed down since the early Miocene, recent tectonic activity still occurs along the Hess Escarpment, as the seafloor in many instances is clearly displaced by faults (e.g., Fig. 6).

OPERATIONS

Even with all propulsion motors back on line, the brisk trade winds slowed the vessel to an average speed of 10.1 kt on the 291-nmi transit from Site 1000. We arrived on site early Friday morning, 2 February 1996, to begin drilling operations.

Hole 1001A

Hole 1001A was spudded and cored with the RCB system because our primary objectives were the lithified rocks below a suspected abbreviated Neogene section and because there was insufficient time to piston core the unlithified sediments and then spud another hole with the RCB system. We used the subsea video camera as an aid to observe the bit contact with the seafloor and to obtain a mudline core. This accurately defined the water/seafloor interface, though only a small amount of ooze was recovered in Core 165-1001A-1R. Core recovery varied from 0.5% to 22% for the first six cores (Table

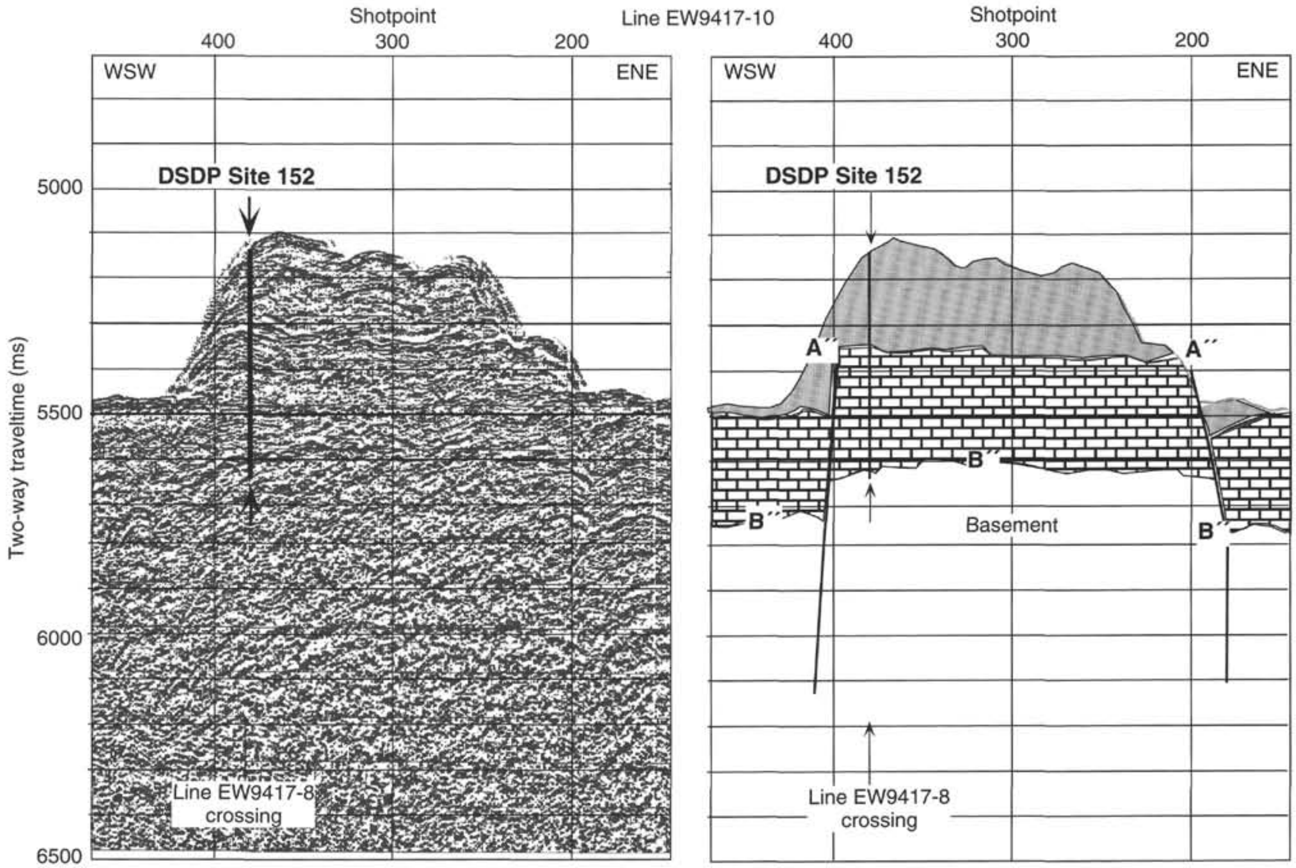

Figure 5. Interpretation of Line EW9417-10 in the vicinity of DSDP Site 152.

1). Bit rotation was started at the top of Core 165-1001A-8R (64.2 mbsf), and by a depth of 93 mbsf (top of Core 165-1001A-11R), the lithology became competent enough to core effectively. Recovery for Cores 165-1001A-11R through 18R ranged from 80% to 102%, but dropped off rapidly after encountering a major unconformity at 165.68 mbsf (at Section 165-1001A-18R-4, 88 cm), where middle Miocene ooze overlies middle and lower Eocene chalk and limestones with numerous, thin chert layers. Recovery through the hard limestones and chert ranged from 0% to 57%, but improved significantly below 303 mbsf where the chert layers were absent to very sparse. Some of the highest recovery intervals were at the K/T boundary (Core 165-1001A-38R) and at the basement contact (Core 165-1001A-52R), the latter of which was of exceptionally good quality.

Coring ceased in Hole 1001A after cutting four cores below the basement contact. The hole was circulated clean and a wiper trip was made to 112 mbsf. Approximately 10 m of fill was identified in the bottom of the hole during initial logging operations (see "Downhole Measurements" section, this chapter); this was circulated with water and then bentonite mud.

After logging operations were completed, the drill string was returned to the surface and a new RCB bit was installed for Hole 1001B.

Hole 1001B

Hole 1001B is located approximately 30 m to the south of Hole 1001A. Two spot RCB cores were collected, at 25.3 and 150.3 mbsf, as the hole was being drilled down to 206.5 mbsf, where continuous coring operations began. In general, core recovery was similar to that obtained in Hole 1001A for similar depth intervals. The interval cored, however, was offset by 2 m in depth from that of Hole 1001A in hope of recovering intervals missed in Hole 1001A and to position the K/T boundary interval within the core liner, rather than in the core catcher. This strategy was very successful as we not only collected the K/T boundary where planned, but also managed to recover another Paleocene/Eocene boundary section and another excellent basement/sediment contact. Coring ceased at a depth of 488.3 mbsf (2 m into basement) owing to time constraints.

LITHOSTRATIGRAPHY

The 522.8-m-thick sequence recovered at Hole 1001A ranges in age from Late Cretaceous to Pleistocene, and consists of pelagic sediment and sedimentary rocks with varying amounts of clays and volcanic ash, and a succession of basaltic lavas at the base. The igneous basement was reached at a depth of 485.4 mbsf in Holes 1001A and 1001B. Site 1001 contains a K/T boundary interval at approximately 352 mbsf. High density measurements (5-cm sample spacing) of color reflectance (see Appendix tables on CD-ROM, back pocket, this volume) and magnetic susceptibility, in addition to shipboard data on carbonate content and standard sedimentological criteria (percent microfossils and minerals in smear slides, depositional textures, sedimentary structures, and bulk-rock X-ray diffraction [XRD] analyses), form the basis for dividing the recovered sedimentary sequence into three lithologic units (I–III) and a number of subunits (Fig. 10). The basement forms a fourth lithologic unit (IV), which is discussed in the "Igneous Petrology and Volcanology" section (this chapter).

Description of Lithologic Units

Unit I

Intervals: Cores 165-1001A-2R through 18R-4, 90 cm; Cores 165-1001B-1R and 2R

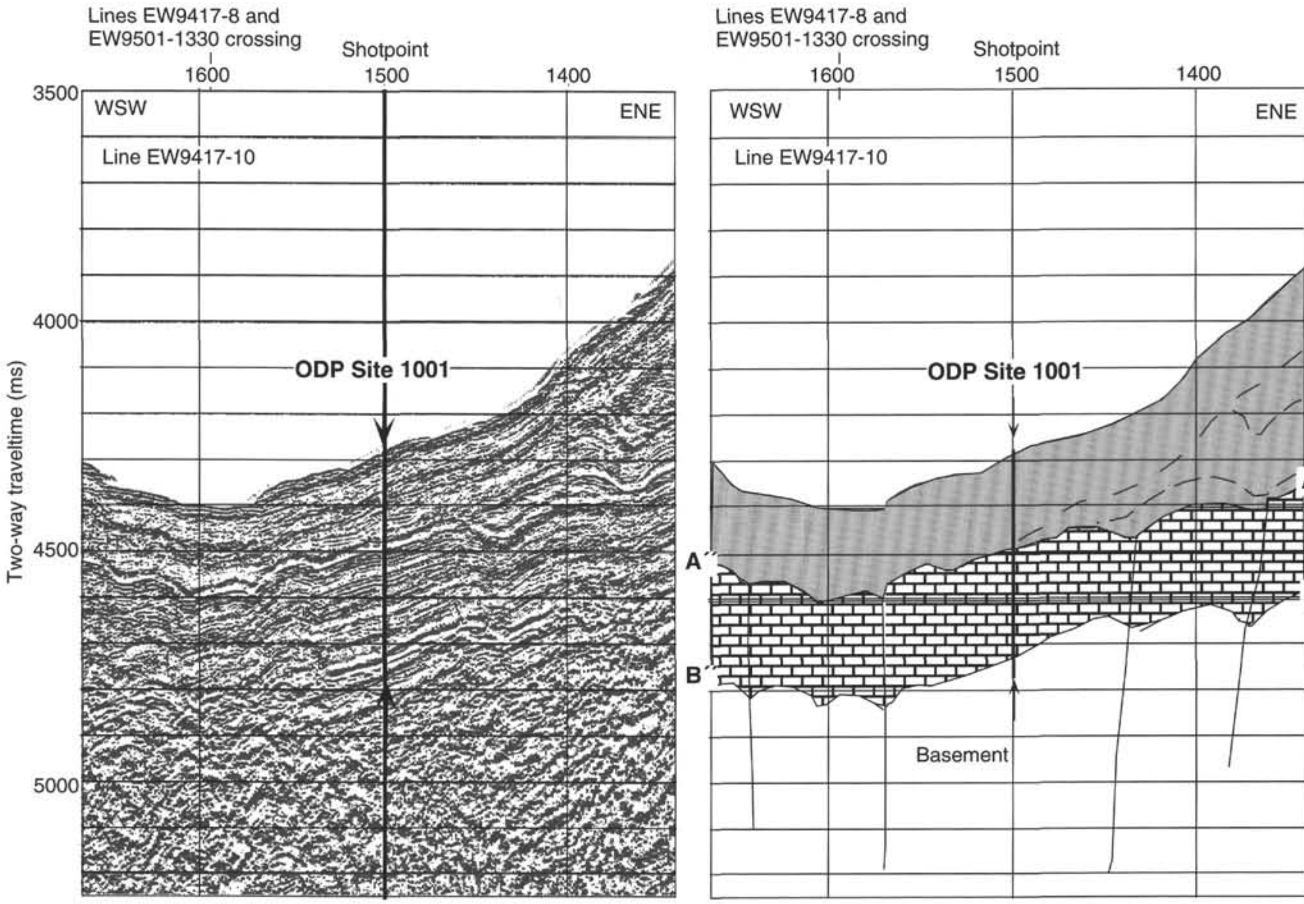

Figure 6. Interpretation of Line EW9417-10 in the vicinity of Site 1001.

Age: Pleistocene to middle Miocene
Depths: 0–165.7 mbsf, Hole 1001A; 25.3–35.0, 150.3–160 mbsf, Hole 1001B

Unit I consists of 165.7 m of pelagic sediments that overlie a double unconformity separating middle Miocene from middle Eocene and lower Eocene strata at Site 1001 (Fig. 10). In total, about 38 m.y. of section is missing at these unconformities (see "Biostratigraphy" section, this chapter).

Subunit IA

Intervals: Cores 165-1001A-2R through 12R; Core 165-1001B-1R
Age: Pleistocene to late Miocene
Depth: 0–112.2 mbsf, Hole 1001A; 25.3–35.0 mbsf, Hole 1001B

Use of the rotary core barrel (RCB) to drill the soft sediments of the Neogene section at Site 1001 resulted in generally poor recovery (~37%), hampering complete lithologic description of the upper 100 mbsf. Sediments of Subunit IA appear to consist largely of a gradational mixture of nannofossil clayey mixed sediment, clayey nannofossil mixed sediment with foraminifers, clayey nannofossil ooze, and nannofossil ooze with clay and foraminifers. These sediments are generally light yellowish brown to light olive brown or gray in color, massive, and moderately bioturbated; they show little other evidence of visual sedimentary structures. Shipboard carbonate measurements suggest an average carbonate content of about 60% in the upper part (6.4–75 mbsf) of the subunit, with a range in measured values from 55% to 68%, and in the lower part of the subunit (75–112.2 mbsf) an average of 52%, ranging from 42% to 65%. Broken pteropod shells found in Section 165-1001A-7R-2 indicate intervals where carbonate preservation may be greatly enhanced. The non-clay component of these sediments is composed of calcite, quartz, and trace quantities of feldspars. The clay mineral component is dominantly composed of smectite and trace quantities of kaolinite, chlorite, and possibly illite (Table 2; Fig. 11). Pyrite, although a minor component of the sediment, is persistent in its occurrence throughout the subunit. It is usually found either disseminated or as burrow infillings, except in Section 165-1001A-6R-1, 43 cm, where a 1-cm-diameter pyrite nodule was observed. Turbidites are rare in the described section and appear only as a few, relatively thin, graded foraminiferal sands in Cores 165-1001A-2R and 3R.

Subunit IB

Intervals: Core 165-1001A-13R through Section 165-1001A-15R-1, 20 cm
Age: late Miocene
Depth: 112.2–131.7 mbsf, Hole 1001A

Sediments of this subunit are predominantly clayey nannofossil ooze, nannofossil ooze with clay, and nannofossil ooze with foraminifers and clay. The downhole transition to sediments of Subunit IB is marked by a relatively sharp jump in carbonate contents, to values consistently greater than about 70%; by a distinct increase in color reflectance in the 550 nm (green) wave band; and by a drop in measured magnetic susceptibility (Fig. 10). Sediments of Subunit IB are also distinguished by evidence of increasing induration, with the oozes being generally firm and, in some intervals, approaching chalk in their degree of lithification. This relative increase in induration is evident in the much higher rate of sediment recovery (~91%) compared with that from the overlying Subunit IA.

Subunit IB sediments are almost uniformly massive, moderately bioturbated, and light olive gray to olive gray in color. The bulk min-

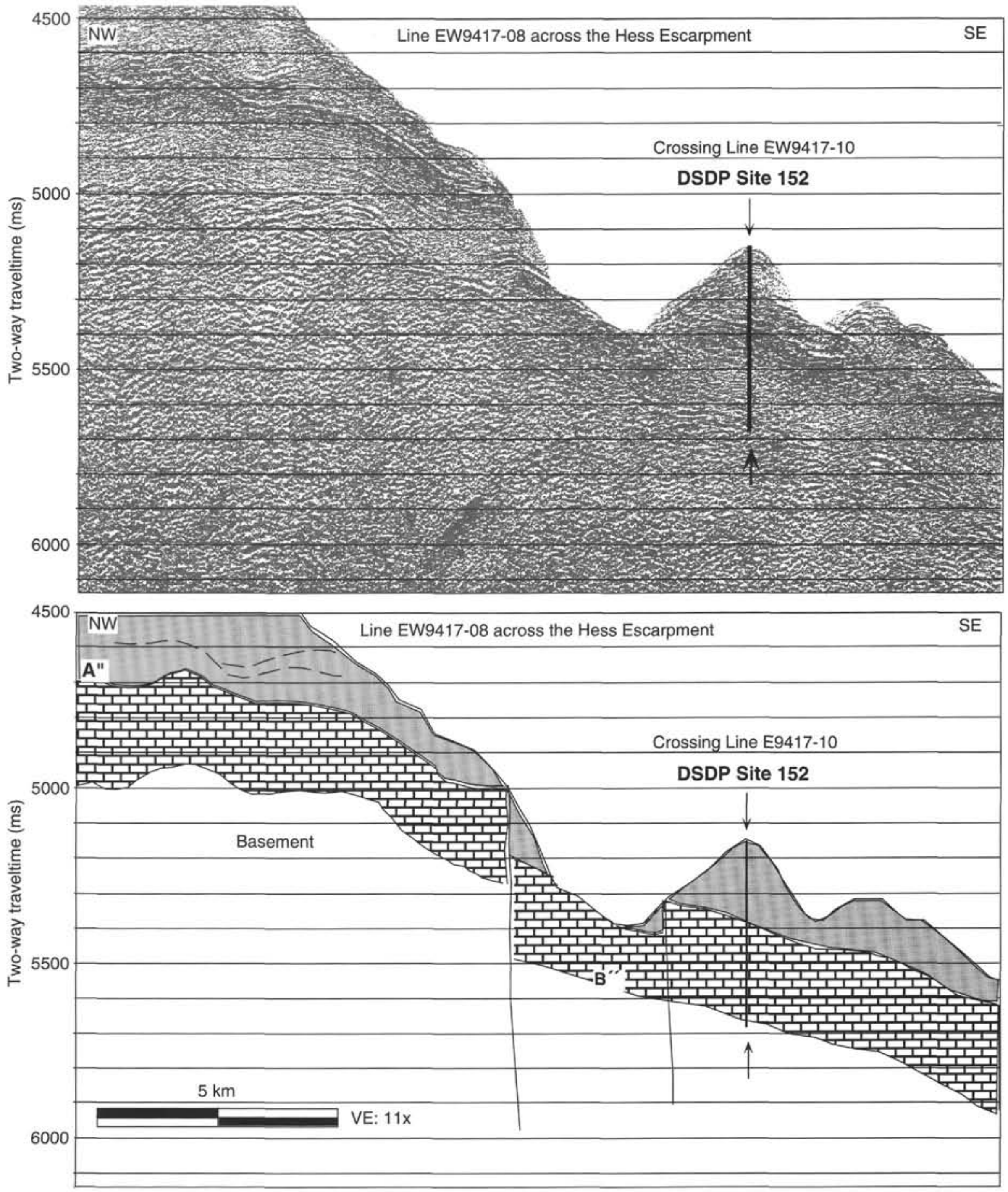

Figure 7. Interpretation of Line EW9417-08 across the Hess Escarpment and through the location of DSDP Site 152. VE = vertical exaggeration.

eralogy of this subunit is essentially similar to that of Subunit IA, although illite is now less than the limit of detection, and the relative abundance of quartz is probably slightly lower (Fig. 11). Pyrite is common in disseminated form on the surface of the split cores and as aggregates in burrows.

Subunit IC

Intervals: Sections 165-1001A-15R-1, 20 cm, through 165-1001A-17R-2, 100 cm; Sections 165-1001B-2R-1 through 2R-2
Age: late to middle Miocene
Depth: 131.7–153.2 mbsf, Hole 1001A; 150.3–153.3 mbsf, Hole 1001B

Sediments of Subunit IC consist of an interbedded mixture of nannofossil ooze with clay, clayey nannofossil ooze, and nannofossil clay, largely distinguished from each other by their color and variable carbonate contents. The top of the subunit is marked by a steep downhole decrease in carbonate content, from values in excess of 70% to values close to 30%, and by a corresponding increase in whole-core magnetic susceptibility and a more subtle decrease in color reflec-

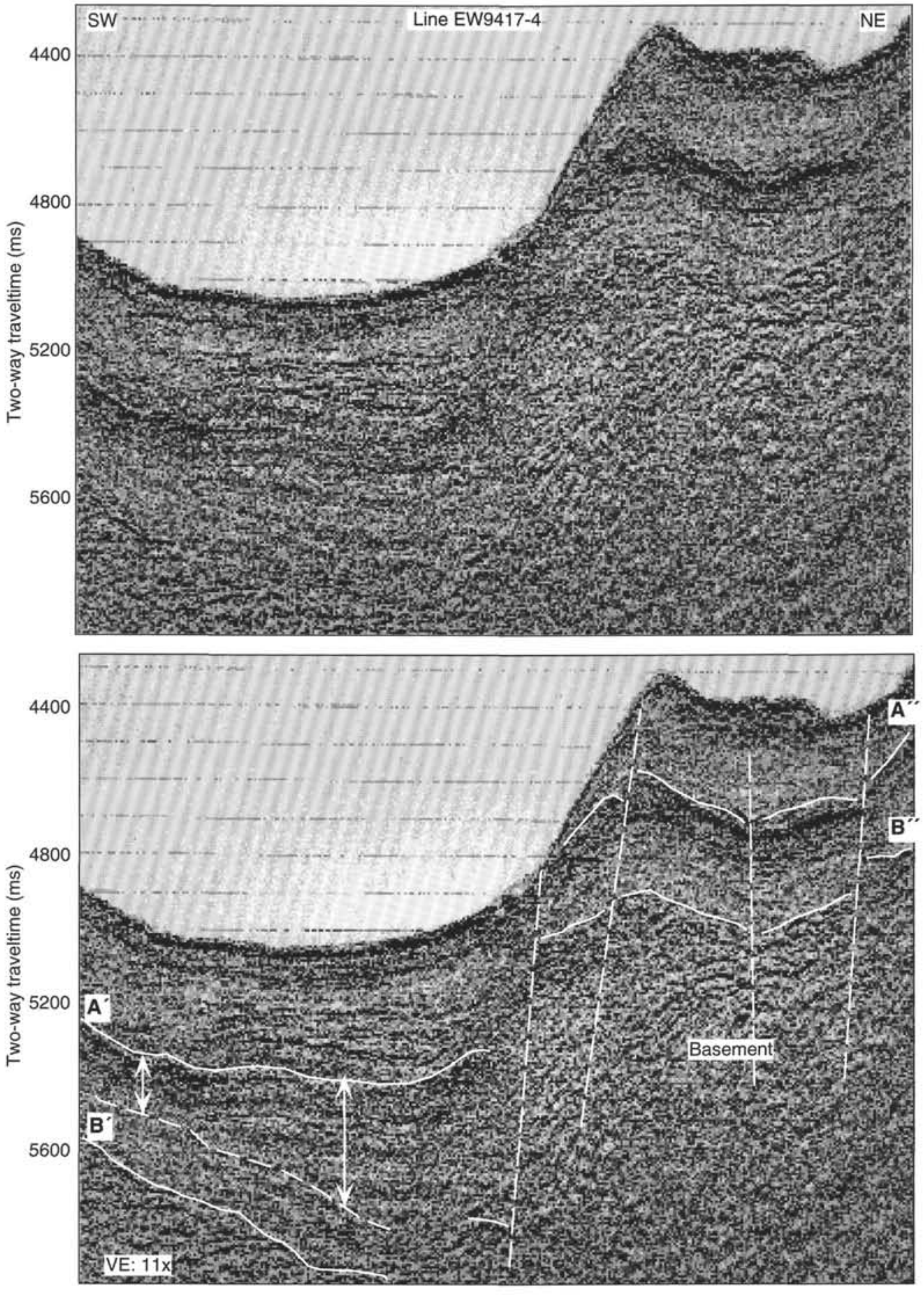

Figure 8. Interpretation of Line EW9417-04 across a major north-northwest-trending canyon showing its relation with a half graben, which was formed and filled along a growth fault sometime during seismic Unit B. Initiation of the graben could have occurred sometime in the Late Cretaceous or early Cenozoic. VE = vertical exaggeration.

tance at the "green" (550 nm) wavelength (Fig. 10). The base of the subunit is marked by an increase in carbonate content to values similar to Subunit IB, an increase in the reflectivity of the sediment, and a pronounced drop in magnetic susceptibility values. Subunit IC, which straddles the middle/late Miocene boundary, includes the carbonate crash previously documented at Sites 998, 999, and 1000.

Sediments of this subunit are generally fine-grained, homogeneous, and moderately bioturbated throughout. With the increased clay content of these sediments, the color darkens noticeably, ranging from light yellowish brown and light gray to light olive brown and olive brown. The overall proportion of smectitic clay and quartz increases within this subunit relative to Subunit IB, although this signal is partly obscured by fluctuations in carbonate content of up to 60% (Fig. 12), which also typify this interval. In addition to smectite, traces of chlorite and kaolinite are also present. Pyrite appears to be only a minor component of the sediments and is primarily restricted to the

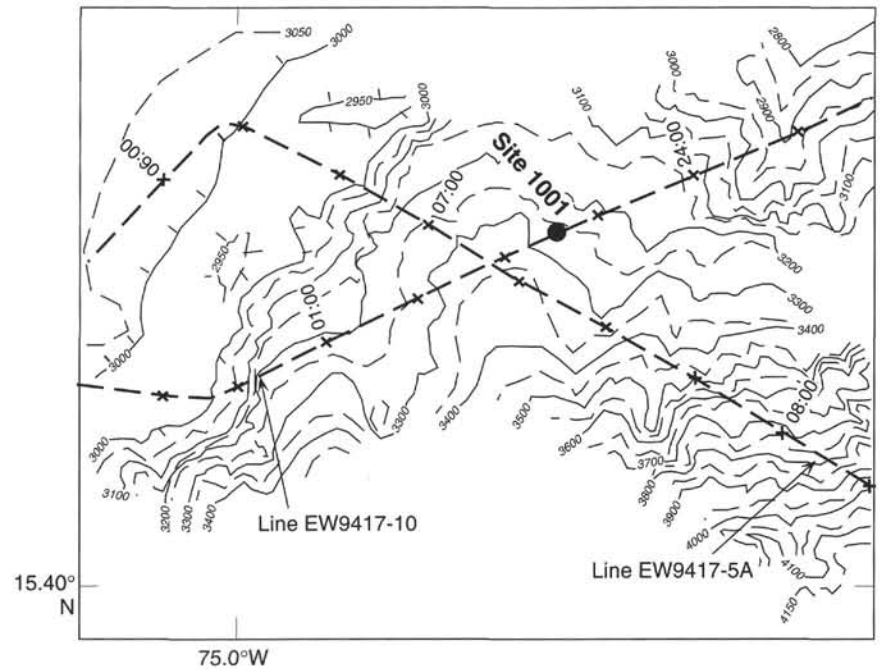

Figure 9. Detailed bathymetric map (based upon the EW9417 Hydrosweep survey) of the area where Site 1001 is located on the northern side of a canyon, a tributary to a larger north-northwest-trending canyon, dissecting the upper reaches of the Hess Escarpment.

occasional pyritized burrow. Induration levels are comparable with those in the overlying Subunit IB, with sediments generally quite firm and becoming increasingly "chalk-like" in the higher carbonate intervals.

Subunit ID

Intervals: Sections 165-1001A-17R-2, 100 cm, through 18R-4, 90 cm; Sections 165-1001B-2R-3 through 165-1001B-2R-CC
Age: middle Miocene
Depth: 153.2–165.7 mbsf, Hole 1001A; 153.3–160 mbsf, Hole 1001B

Subunit ID consists of a relatively thin interval of sediments, made up largely of interbedded nannofossil oozes with clay and clayey nannofossil oozes. The downward transition to this subunit from Subunit IC is marked by a sharp rise in carbonate content, by an increase in color reflectance, by decreases in magnetic susceptibility to their lowest values in all of Unit I, and by a sharp reduction in the relative abundance of quartz and clay minerals. The base of Subunit ID is marked by a prominent hiatus that separates the middle Miocene sediments of Unit I from the underlying middle and lower Eocene calcareous chalks and cherts of Unit II.

Nannofossil oozes in the upper part of Subunit ID are generally light gray to olive gray in color, but take on a light greenish gray to greenish gray color below about Section 165-1001A-17R-3, 55 cm, which may reflect subtle redox changes in the sediment. The oozes tend to be fine grained, very homogeneous in texture, and well indurated, almost to levels that are more appropriately called chalk. The background sediments are composed predominantly of calcite, but minor quantities of quartz are also present, as are trace quantities of clay minerals, feldspar(?), and clinoptilolite. Within the minor clayey nannofossil ooze lithology, the mineralogy is similar to that of Subunit IC (e.g., XRD Sample 165-1001A-18R-2, 81–82 cm).

Bioturbation is slight to moderate, with well-preserved *Zoophycos* burrows observed at several levels in Core 165-1001A-18R. Sections 5 and below in Core 165-1001A-17R are moderately to heavily disturbed, either by the coring of slumped or redeposited material, or possibly as a result of the drilling itself. The recovery of disturbed sediment in Section 165-1001B-2R-CC at approximately the same depth level tends to support arguments for a slump.

Unit II

Intervals: Sections 165-1001A-18R-4, 90 cm, through 165-1001A-38R-7, 99 cm; Core 165-1001B-3R through Section 165-1001B-18R-4, 60 cm
Age: middle Eocene to early Paleocene
Depth: 165.7–352.1 mbsf, Hole 1001A; 206.5–352.1 mbsf, Hole 1001B

Lithologic Unit II at Site 1001 consists of calcareous chalks containing varying proportions of nannofossils, foraminifers, and clay, grading downhole into mixed sedimentary rocks. Unit II ranges in age from middle Eocene to late Paleocene. The upper boundary of Unit II is defined by the downhole transition from ooze to chalk, and coincides with an unconformity that brings overlying middle Miocene nannofossil ooze with clay directly into contact with middle Eocene calcareous chalk with nannofossils and clay (Fig. 13). The lower boundary of Unit II is defined by the contact between mixed sedimentary rocks and claystones with calcareous chalk, and an increase in carbonate content to more than 85%. The lower boundary also coincides with an increase in the 550-nm wavelength color reflectance and a decrease in magnetic susceptibility values (Fig. 10).

Unit II is divided into two subunits (IIA and IIB). The subdivision is based upon carbonate values, chert distribution, and variations in color reflectance and magnetic susceptibility data (Fig. 10).

Subunit IIA

Intervals: Section 165-1001A-18R-4, 90 cm, through Core 165-1001A-33R; Core 165-1001B-3R through Section 165-1001B-13R-2
Age: middle Eocene to late Paleocene
Depth: 165.7–304.6 mbsf, Hole 1001A; 206.5–304.6 mbsf, Hole 1001B

Lithologies of Subunit IIA consist of calcareous chalk, calcareous chalk with nannofossils and clay, calcareous chalk with foraminifers, calcareous chalk with clay, and clayey calcareous chalk. The contacts between lithologies are transitional, and intervals of any given lithology typically range in thickness from the centimeter to decimeter scale. Chert layers, an important feature of Subunit IIA, are absent in

Table 1. Coring summary, Site 1001.

Core no.	Date (Feb. 1966)	Time (UTC)	Depth (mbsf)	Cored (m)	Recovered (m)	Recovery (%)
165-1001A-						
1R	2	2100	0.0–6.4	6.4	0.03	0.5
2R	2	2230	6.4–16.1	9.7	0.79	8.1
3R	2	2310	16.1–25.7	9.6	1.98	20.6
4R	2	2350	25.7–35.3	9.6	0.67	7.0
5R	3	0025	35.3–44.9	9.6	1.43	14.9
6R	3	0105	44.9–54.6	9.7	2.11	21.7
7R	3	0145	54.6–64.2	9.6	4.01	41.8
8R	3	0230	64.2–73.8	9.6	7.60	79.1
9R	3	0310	73.8–83.4	9.6	3.46	36.0
10R	3	0400	83.4–93.0	9.6	3.08	32.1
11R	3	0440	93.0–102.6	9.6	8.70	90.6
12R	3	0525	102.6–112.2	9.6	8.09	84.3
13R	3	0600	112.2–121.8	9.6	9.80	102.0
14R	3	0635	121.8–131.5	9.7	7.81	80.5
15R	3	0710	131.5–141.0	9.5	9.24	97.2
16R	3	0800	141.0–150.7	9.7	8.50	87.6
17R	3	0840	150.7–160.3	9.6	9.83	102.0
18R	3	0920	160.3–168.0	7.7	6.34	82.3
19R	3	1030	168.0–170.0	2.0	0.37	18.5
20R	3	1215	170.0–179.6	9.6	1.40	14.6
21R	3	1415	179.6–189.2	9.6	1.60	16.6
22R	3	1545	189.2–198.8	9.6	0.38	4.0
23R	3	1650	198.8–208.4	9.6	1.19	12.4
24R	3	1830	208.4–218.0	9.6	2.32	24.1
19R	3	1030	168.0–170.0	2.0	0.37	18.5
20R	3	1215	170.0–179.6	9.6	1.40	14.6
21R	3	1415	179.6–189.2	9.6	1.60	16.6
22R	3	1545	189.2–198.8	9.6	0.38	4.0
23R	3	1650	198.8–208.4	9.6	1.19	12.4
24R	3	1830	208.4–218.0	9.6	2.32	24.1
25R	3	1945	218.0–227.6	9.6	2.44	25.4?
26R	3	2100	227.6–237.2	9.6	2.61	27.2
27R	3	2215	237.2–246.9	9.7	5.34	55.0
28R	3	2350	246.9–256.5	9.6	2.56	26.6
29R	4	0130	256.5–266.1	9.6	3.34	34.8
30R	4	0300	266.1–275.7	9.6	0.00	0.0
31R	4	0445	275.7–285.4	9.7	0.04	0.4
32R	4	0930	285.4–294.9	9.5	5.45	57.3
33R	4	1045	294.9–304.6	9.7	4.54	46.8
34R	4	1200	304.6–314.2	9.6	8.81	91.8
35R	4	1315	314.2–323.8	9.6	9.77	102.0
36R	4	1430	323.8–333.4	9.6	8.46	88.1
37R	4	1600	333.4–343.1	9.7	9.90	102.0
38R	4	1800	343.1–352.7	9.6	9.13	95.1
39R	4	1945	352.7–362.3	9.6	6.81	70.9
40R	4	2100	362.3–372.0	9.7	5.61	57.8
41R	4	2230	372.0–381.6	9.6	9.04	94.1
42R	5	0005	381.6–391.2	9.6	7.66	79.8
43R	5	0135	391.2–400.8	9.6	7.40	77.1
44R	5	0330	400.8–410.4	9.6	9.07	94.5
45R	5	0520	410.4–420.0	9.6	5.01	52.2
46R	5	0700	420.0–429.6	9.6	5.16	53.7
47R	5	0900	429.6–439.2	9.6	5.80	60.4
48R	5	1100	439.2–448.8	9.6	3.93	40.9
49R	5	1300	448.8–458.4	9.6	4.54	47.3
50R	5	1515	458.4–468.0	9.6	7.87	82.0
51R	5	1730	468.0–477.7	9.7	5.80	59.8
52R	5	2000	477.7–487.3	9.6	9.19	95.7
53R	5	2330	487.3–494.0	6.7	4.91	73.3
54R	6	0610	494.0–503.6	9.6	8.43	87.8
55R	6	1020	503.6–513.2	9.6	3.31	34.5
56R	6	1545	513.2–522.8	9.6	3.57	37.2
Coring totals				522.8	286.23	54.7
165-1001B-						
****Drilled from 0.0 to 25.3 mbsf****						
1R	8	1230	25.3–35.0	9.7	3.77	38.8
*****Drilled from 35.0 to 150..3 mbsf****						
2R	8	1615	150.3–160.0	9.7	8.46	87.2
*****Drilled from 160.0 to 206.5 mbsf****						
3R	8	2230	206.5–216.0	9.5	1.73	18.2
4R	8	2345	216.0–225.6	9.6	1.99	20.7
5R	9	0115	225.6–235.3	9.7	3.43	35.3
6R	9	0300	235.3–244.9	9.6	4.23	44.0
7R	9	0430	244.9–254.5	9.6	9.05	94.3
8R	9	0555	254.5–264.1	9.6	5.97	62.2
9R	9	0720	264.1–273.7	9.6	2.95	30.7
10R	9	0840	273.7–283.4	9.7	3.84	39.6
11R	9	1010	283.4–292.9	9.5	5.34	56.2
12R	9	1130	292.9–302.6	9.7	9.00	92.8
13R	9	1300	302.6–312.2	9.6	9.72	101.0
14R	9	1415	312.2–321.8	9.6	8.69	90.5
15R	9	1530	321.8–331.4	9.6	7.16	74.6
16R	9	1700	331.4–341.1	9.7	9.49	97.8
17R	9	1900	341.1–348.0	6.9	5.90	85.5
18R	9	2115	348.0–356.3	8.3	6.26	75.4
19R	9	2300	356.3–362.3	6.0	3.71	61.8
20R	10	0030	362.3–372.0	9.7	8.45	87.1
21R	10	0200	372.0–379.6	7.6	8.46	111.0
22R	10	0340	379.6–389.2	9.6	9.32	97.1
23R	10	0515	389.2–398.8	9.6	9.28	96.6
24R	10	0650	398.8–408.4	9.6	5.39	56.1
25R	10	0830	408.4–418.0	9.6	6.67	69.5
26R	10	1030	418.0–427.6	9.6	5.01	52.2
27R	10	1230	427.6–437.2	9.6	5.88	61.2
28R	10	1430	437.2–446.8	9.6	2.35	24.5
29R	10	1630	446.8–457.4	10.6	3.73	35.2
30R	10	1845	457.4–468.0	10.6	7.22	68.1
31R	10	2100	468.0–478.7	10.7	8.72	81.5
32R	10	2345	478.7–488.3	9.6	9.93	103.0
Coring totals				301.2	201.10	66.8
Drilled				187.1		
Total				488.3		

Note: An expanded version of this coring summary table that includes lengths and depths of sections, location of whole-round samples, and comments on sampling disturbance is included on CD-ROM in the back pocket of this volume.

Subunit IIB (Fig. 14). The boundary between the two subunits has been selected to coincide with the core containing the lowest occurrence of chert. Overall recovery within Subunit IIA is poor, possibly as a consequence of the abundance of chert layers. As a result, color, magnetic susceptibility, and carbonate measurements are not continuous. No significant trends are apparent in the available color and magnetic susceptibility data. Carbonate contents range between 32% and 84% (Fig. 10).

The upper boundary of Subunit IIA coincides with a middle Eocene/middle Miocene unconformity spanning approximately 30 m.y. (see "Biostratigraphy" section, this chapter). The sequence of sediments immediately beneath the boundary includes a second, minor unconformity (~8 m.y.), which brings middle Eocene white calcareous chalk with nannofossils (interval 165-1001A-18R-4, 90–116 cm) directly into contact with lower Eocene light greenish gray calcareous chalk with clay and nannofossils (Fig. 13). A 5-cm-thick, greenish gray chert layer occurs at the contact between the two Eocene lithologies.

Smear-slide data indicate that the major constituents of Subunit IIA are nannofossils and foraminifers with some clay minerals. The XRD results from the noncarbonate bulk rock fraction of Subunit IIA contrast strongly with those of overlying Unit I. The terrigenous/volcanic component of Unit I (smectite and quartz, together with traces of feldspar, chlorite, and kaolinite) is replaced by the intermittent occurrence of opal CT and by traces of clinoptilolite. Quartz is present in negligible quantities, and clays are only present in relatively minor amounts (clay types are indistinguishable). The main lithologies of Subunit IIA are generally massive and moderately bioturbated. Chert layers form distinctive and discrete packages, generally 5–10 cm thick, with boundaries clearly defined by sharp and undulatory contacts and color changes (Fig. 15). The chertification front seems to follow bioturbation patterns and results in irregular morphologies within the chert layers. Log data, such as density, resistivity, and microresistivity (Formation MicroScanner) indicate that the maximum chert frequency and layer thickness is between 167 and 200 mbsf, which corresponds to the interval with poorest recovery (see "Downhole Measurements" section).

A distinctive sedimentological feature observed in Subunit IIA is a claystone interval, occurring in Cores 165-1001A-27R and 165-1001B-6R (Fig. 16). Biostratigraphic data indicate that this event falls within the uppermost Paleocene (see "Discussion," below) and suggests a correlation with a similar feature recovered at Site 999.

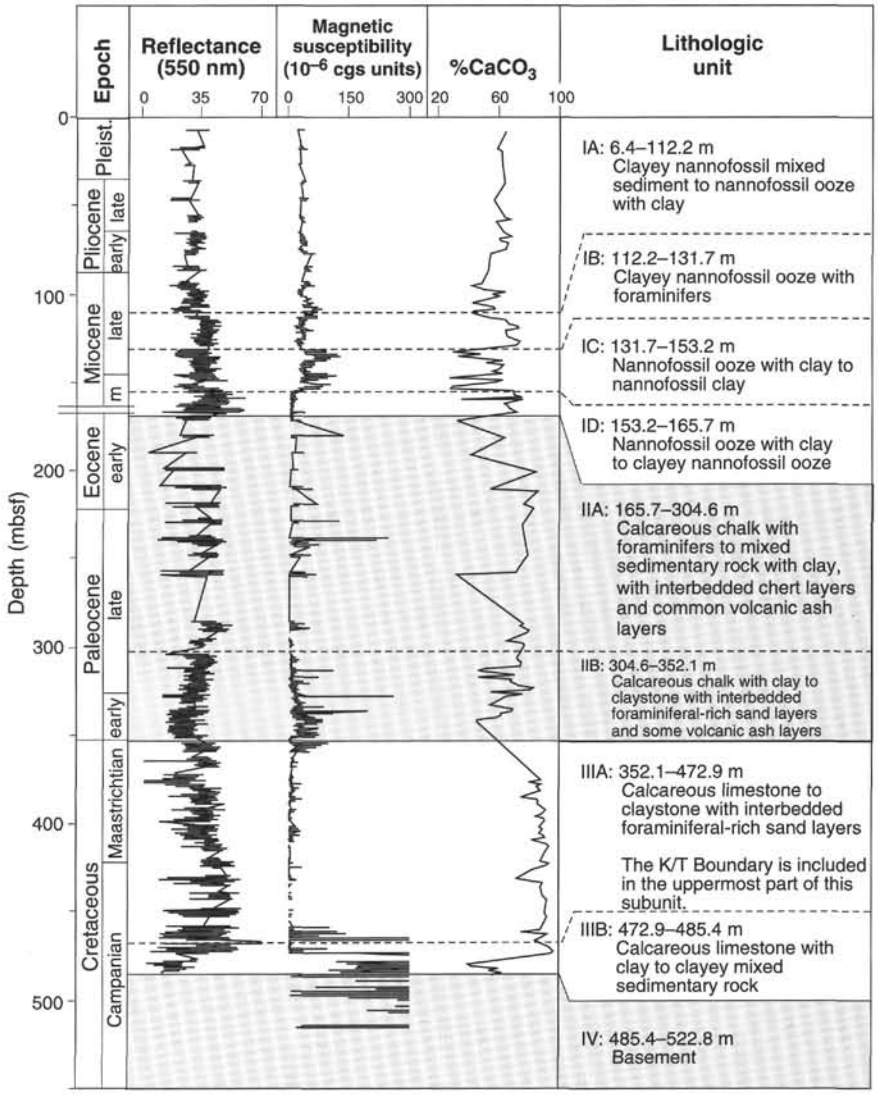

Figure 10. Lithostratigraphic units of Site 1001 (Hole 1001A) and their relationship to downcore variations in color reflectance, magnetic susceptibility, and $CaCO_3$ data.

The spacing of samples for carbonate analysis within the claystone interval is too coarse to show the extent of this event on the carbonate content curve. Its boundaries (Fig. 17), however, show a sharp increase in multisensor track (MST) values that coincide with this event. Log data also indicate maximum values in magnetic susceptibility as well as a peak in the natural gamma-ray counts (see "Downhole Measurements" section, this chapter).

Ash layers are present within Subunit IIA as a minor lithology and consist of fresh and altered glass shards. Significant variations in the frequency of ash layers occur throughout Subunits IIA and IIB, and represent major episodes of explosive volcanism from sources to the west of Site 1001 (see "Igneous Petrology and Volcanology" section, this chapter). The layers are gray to greenish gray to dark gray and occur as layers with sharp basal contacts and bioturbated tops, or as dispersed, bioturbated zones.

Subunit IIB

Intervals: Core 165-1001A-33R through Section 165-1001A-38R-7, 99 cm; Sections 165-1001B-13R-2 through 165-1001B-18R-4, 60 cm

Age: late to early Paleocene

Depth: 304.6–352.1 mbsf, Hole 1001A; 304.6–352.1 mbsf, Hole 1001B

The main lithologies of Subunit IIB consist of light gray, bluish gray, and greenish gray calcareous chalk with clay and light gray mixed sedimentary rock interbedded with light brownish gray claystone. The calcareous chalk with clay is late Paleocene in age (Cores 165-1001A-33R through 37R), and the mixed sedimentary rocks and claystones are of early Paleocene age (Core 165-1001A-38R). The calcareous chalk with clay is massive and moderately bioturbated; they commonly contain wispy laminations. Across several intervals there are centimeter-scale clayey calcareous limestones. Carbonate contents range from 45% to 82.5% (Fig. 10). The mineralogy of the background sediment, as determined by XRD, is similar to that of Subunit IIA. Opal-CT is present in the background sediment (Sample 165-1001A-34R-1, 68–70 cm), showing the transitional nature of the cherts/silicified limestones(?) in Subunit IIA with the sediments of Subunit IIB. The remaining two XRD samples taken from Subunit IIB are from a minor lithology, clayey calcareous limestone, and contain abundant quartz and smectitic clay.

Centimeter-thick foraminiferal sands, similar to those observed at Site 999, are interbedded with the calcareous chalks with clay. These sand-rich layers were observed in the interval between approximately 290 and 470 mbsf, encompassing Subunits IIB and IIIA, and reach maximum thicknesses within Subunit IIA between 304 and 333 mbsf

Table 2. Bulk-rock XRD analyses for Hole 1001A.

				Mineralogy									
									Clays				
Unit	Subunit	Core, section, interval (cm)	Depth (mbsf)	Calcite	Quartz	Opal CT	Feldspar	Zeolites (clinoptilolite?)	Presence/ absence	Chlorite	Kaolinite	Illite	Smectite
I	A	2R-1, 49–51	6.89	P	P		Tr		P	Tr	Tr	Tr?	P
		6R-1-2, 103–104	45.93	P	P		Tr		P	Tr?	Tr?	Tr?	P
		8R-2, 129–130	66.99	P	P		Tr		P	Tr?	Tr?	Tr?	P
		9R-2, 80–81	76.1	P	P		Tr		P	Tr?	Tr?	Tr?	P
		12R-3, 54–56	106.14	P	P		Tr		P	Tr	Tr		P
	B	14R-4, 55–56	126.85	P	P		Tr?		P	Tr	Tr		P
	C	16R-1, 61–62	141.61	P	P		Tr		P	Tr	Tr		P
		17R-1, 49–50	151.19	P	P		Tr		P	Tr	Tr		P
	D	18R-2, 81–82	162.61	P	P		Tr?		P	Tr	Tr		P
		18R-3, 53–54	163.83	P	P		Tr	Tr	Tr				
II	A	19R-1, 28–29	168.28	P	Tr?	P	Tr	Tr					
		20R-1, 48–49	170.48	P	P	P							
		23R-1, 9–10	198.89	P	Tr								
		24R-2, 34–35	210.24	P			Tr?	Tr?	Tr?				
		26R-1, 115–116	228.75	P				Tr	Tr				
		28R-2, 18–19	248.58	P		P	Tr?		Tr				
		32R-1, 80–81	286.2	P	Tr?	P			Tr?				
	B	34R-1, 68–70	305.28	P	P	P	Tr?		<LOD				
		36R-1, 49–50	324.29	P	P				P				
		36R-3, 114–115	327.94	P	P				P				
III	A	40R-2, 69–70	364.49	P	P				Tr				
		44R-4, 90–92	406.08	P	P				Tr				
		50R-2, 124–125	461.14	P	P			P	P				

Note: P = present, Tr = trace, Tr? = questionable trace, LOD = level of detection.

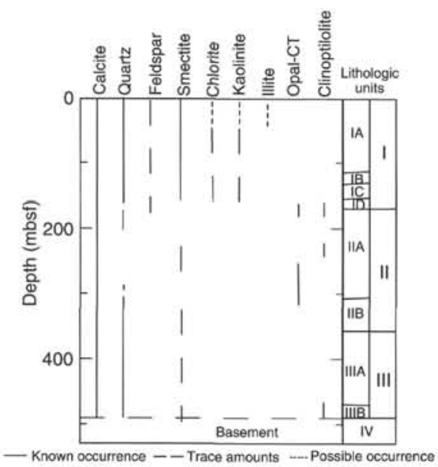

Figure 11. Downcore variations of major minerals in sediments from Site 1001 (Holes 1001A and 1001B), based on XRD bulk sediment analyses.

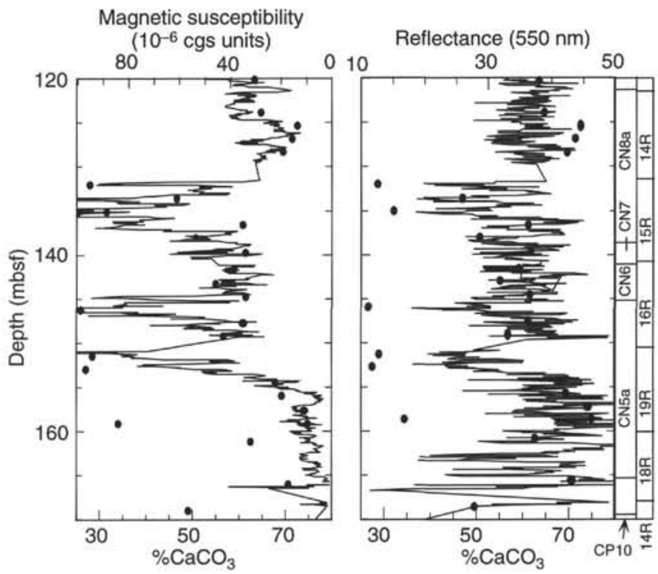

Figure 12. Variations in magnetic susceptibility and color reflectance (solid lines), and carbonate content (solid circles) data in Hole 1001A in the middle/late Miocene carbonate crash interval. Nannofossil biostratigraphic zones are shown in the right-hand column.

(Fig. 18). Their upper and lower boundaries are characterized by an abrupt grain-size change, but are not erosive. Often a less than 1-cm-thick, clay-rich interval bounds both the top and base of the sandy layers. Smear-slide data indicate that the sandy layers consist of a mixture of foraminifers, crystalline carbonate grains, some radiolarians, and clay minerals. The above sedimentological observations indicate that, like the layers recovered at Site 999, they were probably formed by intensified winnowing conditions and/or by an increased flux of foraminifers to the sediment.

Unit III

Intervals: Sections 165-1001A-38R-7, 99 cm, to 52R-6, 70 cm; Sections 165-1001B-18R-4, 60 cm, to 32R-6, 54 cm
Age: earliest Paleocene to mid-Campanian
Depth: 352.1–485.4 mbsf, Hole 1001A; 352.1–486.2 mbsf, Hole 1001B

Lithologic Unit III at Site 1001 is the first sedimentary sequence overlying volcanic basement and consists of clayey calcareous limestone, calcareous limestone with clay, and clayey mixed sedimentary rock. It includes a nearly complete K/T boundary in the uppermost part of the unit (Holes 1001A and 1001B). The upper boundary is defined by the occurrence of a 4.0-cm, light gray, highly indurated limestone of earliest Paleocene age that forms part of the K/T boundary sequence at this site. At the base of the unit, the contact between sed-

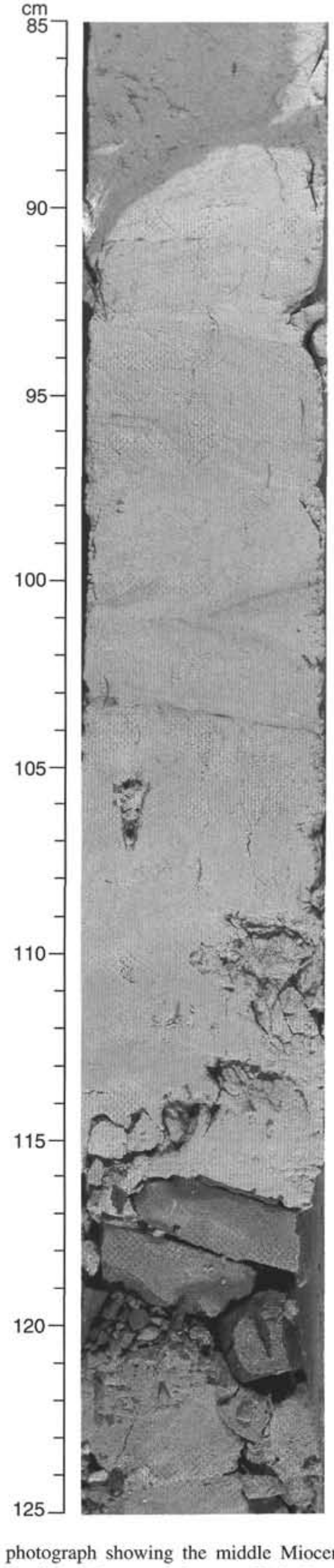

Figure 13. Core photograph showing the middle Miocene/middle Eocene (~30 m.y.) unconformity at the contact between Units I and II (interval 165-1001A-18R-4, 88–91 cm) and the middle Eocene/early Eocene unconformity (~8 m.y.) occurring beneath the contact, which occurs at 116 cm in interval 165-1001A-18R-4, 85–125 cm.

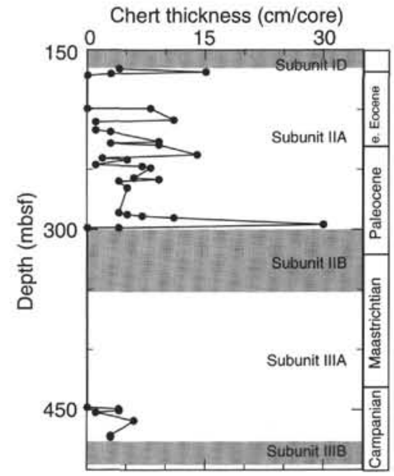

Figure 14. Distribution of chert layers within sedimentary units from Hole 1001A.

iment and basement was fully recovered twice and consists of greenish calcareous limestone intermixed with angular to subangular fragments of basaltic lapilli and breccia that grade downcore into sediment-poor basaltic lapilli and lava flows (Fig. 19).

The major lithologies are interbedded with numerous thin (1–2 cm), clay-rich intervals and, less frequently, with volcanic ash layers and volcanic ash turbidites. In addition, thin (1–5 cm) intervals of foraminifer-rich sediment with relatively sharp contacts are found in the upper part of the unit. Unit III has been divided into two subunits (IIIA and IIIB), based on variations in carbonate content, magnetic susceptibility, and abundance of volcaniclastic sediment (Fig. 10).

Subunit IIIA

Intervals: Sections 165-1001A-38R-7, 99 cm, to 51R-4, 70 cm; Sections 165-1001B-18R-4, 60 cm, to 31R-5, 0 cm
Age: earliest Paleocene to mid-Campanian
Depth: 352.1–472.9 mbsf, Hole 1001A; 352.1–473.7 mbsf, Hole 1001B

The sediments of Subunit IIIA are dominantly light gray to greenish gray clayey calcareous limestone and calcareous limestone with clay. It is distinguished from Unit II by higher carbonate contents, reduced magnetic susceptibility, and lower clay contents (Fig. 10). The upper contact is taken as a thin (4.0 cm) light gray limestone of earliest Paleocene age in Sections 165-1001A-38R-CC and 165-1001B-18R-5. This limestone directly overlies a clay-rich interval that makes up part of the K/T boundary sequence at this site (see below for detailed description).

The main limestone lithology is thick bedded, massive, and moderately bioturbated; it is characterized by greenish gray wispy laminations as well. These laminations appear to be the result of burrow compaction and the concentration of clay minerals along the boundaries of individual burrows (perhaps incipient stylolites?). The major components of Subunit IIIA include fine-grained recrystallized calcite, foraminifer fragments, and nannofossils. Bulk-rock XRD analysis of the background sediments reveals that, in addition to calcite, quartz is also present in minor quantities, as are trace quantities of zeolites (clinoptilolite) and clays (the clay types are indistinguishable). There is a moderate increase in the relative abundance of clay and clinoptilolite in XRD Sample 165-1001A-50R-2, 124–125 cm, possibly as a result of the increased thickness and abundance of the volcanic ashes near the base of Subunit IIIA and basement (Unit IV). Carbonate content ranges from 35% to 93% (Fig. 10). Subunit IIIA contains rare chert nodules in Core 154-1001A-49R.

A distinctive feature of the limestone is the regular occurrence of clay-rich intervals that average about 1–3 cm in thickness (Fig. 20).

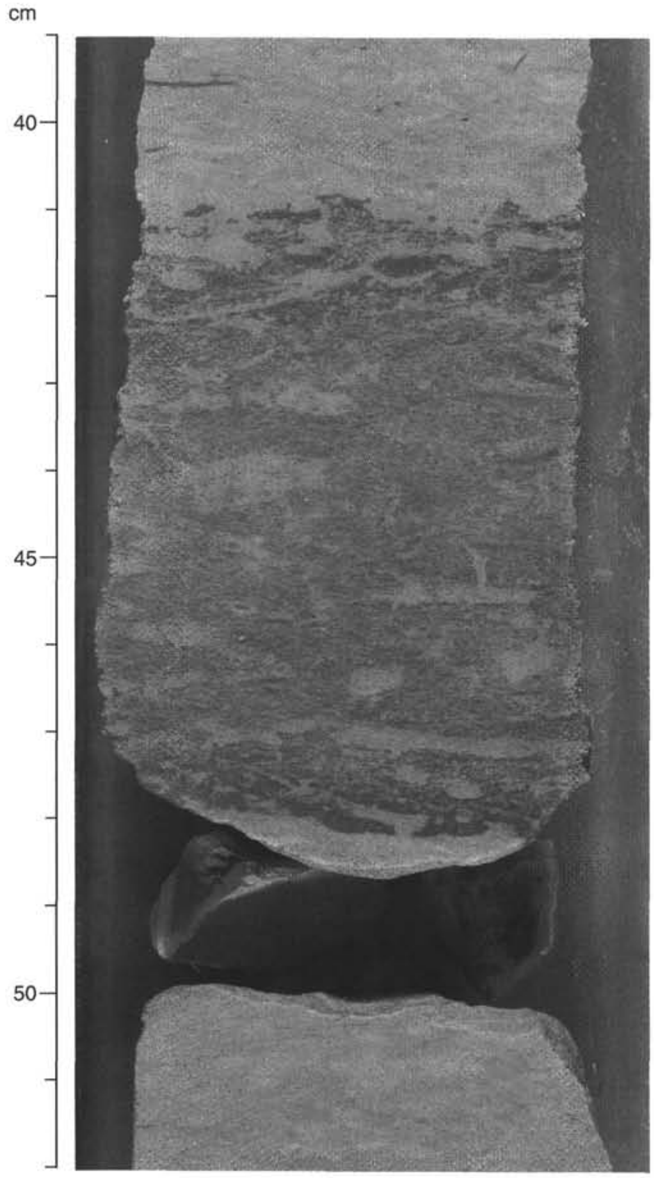

Figure 15. Core photograph showing typical chert layer within Subunit IIA (165-1001A-27R-1, 39–52 cm).

These bands are similar to those observed in part of Subunit IIB (Fig. 20) and lithologic Unit V at Site 999, and are interpreted as representing Milankovitch cyclicity in carbonate accumulation. In addition, there are also thin interbeds of foraminifer-rich sediment that range from 1 to 5 cm in thickness. Often these beds have sharp upper and lower contacts, although gradational contacts are also observed. These beds occur predominantly between 352 and 440 mbsf in Subunit IIIA (Fig. 18).

Volcanic ash layers constitute an important minor component of Subunit IIIA. They occur as gray to dark gray layers with sharp basal contacts and bioturbated tops. Some layers show gradational basal and upper contacts as a result of extensive bioturbation. Most layers consist of abundant altered volcanic glass (smectitic clay) and minor amounts of phenocryst minerals such as feldspar, biotite, and amphibole. The abundance and thickness of ash layers increases downcore in Subunit IIIA (see "Igneous Petrology and Volcanology," this section). In Core 165-1001A-50R, there are three ash deposits that each exceed 20 cm in thickness. Some of these layers exhibit sharp internal contacts defined by changes in grain size and may represent

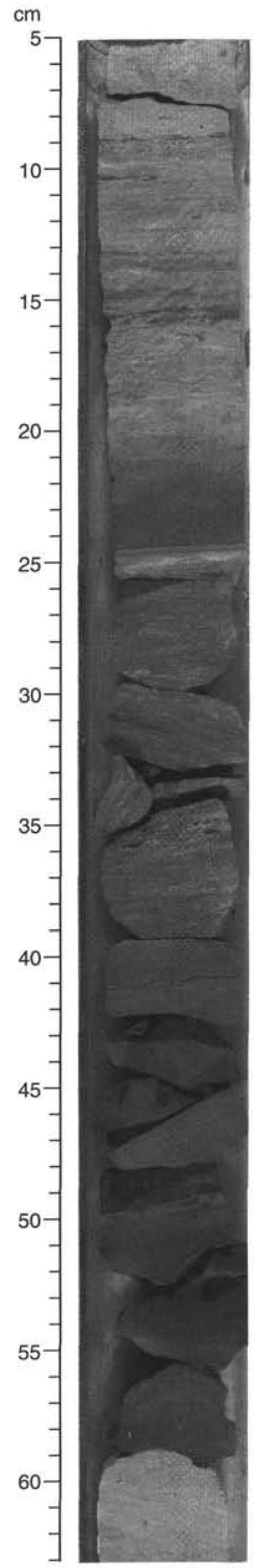

Figure 16. Core photograph showing the claystone interval within 165-1001A-27R-2, 5–63 cm.

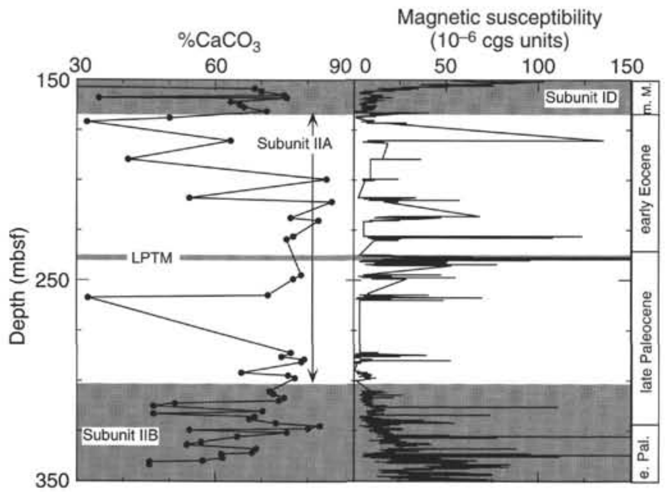

Figure 17. Downcore variations in carbonate content and magnetic susceptibility data within Unit II. LPTM = late Paleocene thermal maximum (see text for further details).

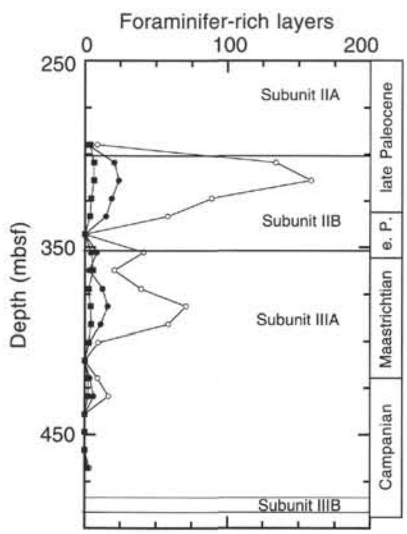

Figure 18. Downhole variations in the number (solid circles), thickness of sand bed (cm; open circles), and average thickness (cm; solid squares) of sandy foraminifer-rich layers in Units II and III.

several closely spaced eruptions. Alternatively, these grain-size variations may reflect redeposition of volcanic ash by sediment gravity flows.

Cretaceous/Tertiary Boundary Sequence

Shipboard biostratigraphic studies indicate that the K/T boundary lies within the uppermost part of Subunit IIIA in Sections 165-1001A-38R-CC and 165-1001B-18R-5. Figure 21 is a core photograph of Section 165-1001A-38R-CC. At the base is a 1-cm-thick, dark greenish gray, massive smectitic clay layer with shaly cleavage. This layer contains small, up to 1-mm-diameter, light-colored speckles. Directly above this layer is 3.5 cm of bluish green gray claystone with small darker green spheroids, approximately 1 mm in diameter. This layer is massive and mottled in appearance. The spheroids in this layer may be altered tektites from the K/T impact event (see "Summary and Conclusions" section, this chapter). Overlying the "tektite" layer is a massive 3.5-cm interval of medium gray to greenish gray claystone. This layer has a shaly cleavage similar to the basal greenish gray smectitic clay layer. Smear slides of sediment from this layer contain rare grains of shocked quartz (see "Summary and Conclusions" section, this chapter). The K/T boundary sequence is capped by a 4-cm-thick highly indurated light gray limestone dated as earliest Paleocene (see "Biostratigraphy" section, this chapter).

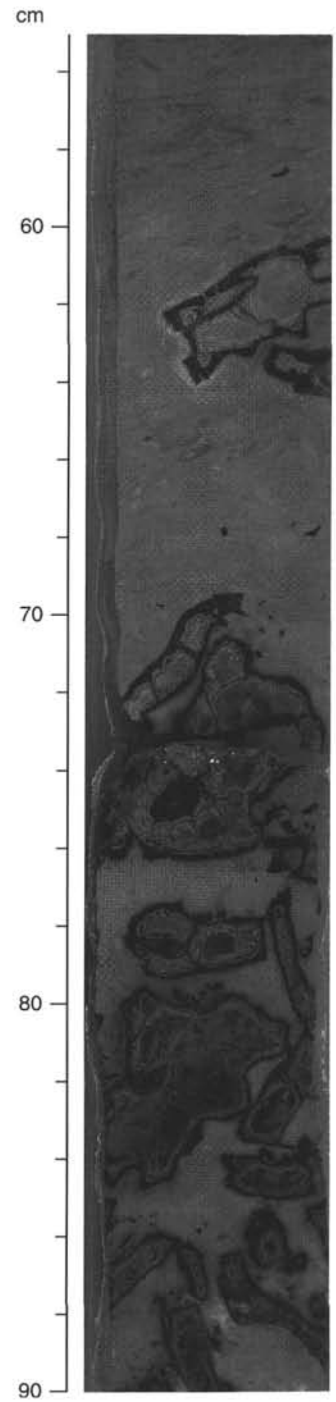

Figure 19. Contact between sediment of Subunit IIIB and volcanic basement (Unit IV). Calcareous limestone grades downward into a basaltic lapilli unit consisting of angular to subangular clasts of altered basalt with remnant quenched rims. Note the sediment infilling between basalt clasts at the boundary (165-1001A-52R-6, 55–90 cm).

Subunit IIIB

Intervals: Sections 165-1001A-51R-4, 70 cm, to 52R-6, 70 cm; Sections 165-1001B-31R-5, 0 cm, to 32R-6, 54 cm

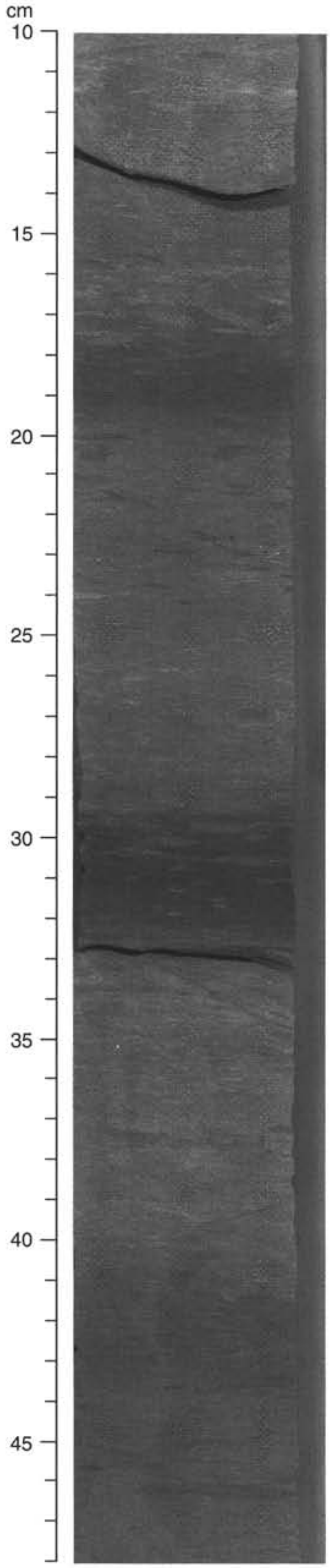

Figure 20. Calcareous limestone of Subunit IIB with thin interbeds of clay-rich sediment (165-1001A-38R-4, 10–48 cm). Note the relatively uniform thickness and spacing of the layers.

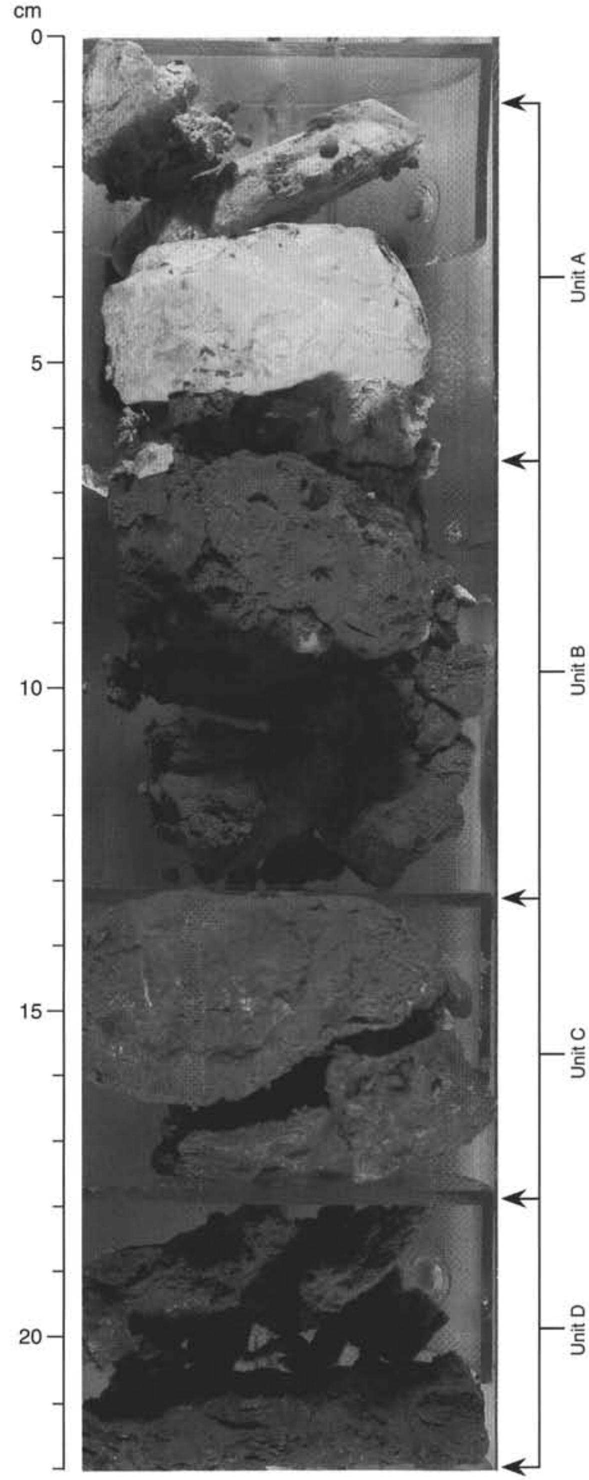

Figure 21. The K/T boundary deposit in Section 165-1001A-38R-CC, 0–22 cm. At the base is a 1-cm-thick dark greenish gray, massive smectitic clay layer with shaly cleavage (Unit D). Directly above this layer is 3.5 cm of bluish green gray claystone with small darker green spheroids, approximately 1 mm in diameter (Unit C). This layer is massive and mottled in appearance. This may represent altered tektites from the K/T impact event. Overlying the "tektite" layers is a massive, 3.5-cm interval of medium gray to greenish gray claystone with shaly cleavage (Unit B). The sequence is capped by a highly indurated light gray limestone dated as earliest Paleocene (Unit C).

Age: mid-Campanian
Depth: 472.9–485.4 mbsf, Holes 1001A; 473.8–486.2 mbsf, Hole 1001B

Subunit IIIB consists of alternating layers of greenish gray calcareous limestone with clay and greenish gray clayey mixed sedimentary rock. The major lithologies occur as thick- to medium-bedded layers with gradational contacts. Alternation of these lithologies give the subunit a crudely stratified appearance. For the most part, the layers are massive and moderately bioturbated. Compaction of burrows, as in Subunit IIIA, has led to the development of wispy laminations. The major components of these limestones and mixed sedimentary rocks include recrystallized carbonate grains, foraminifer fragments, and clay minerals.

Subunit IIIB is distinguished from Subunit IIIA by a significant reduction in carbonate contents and a dramatic increase in the abundance of altered volcaniclastic material (Fig. 10). The volcaniclastic material is present as sand- to granule- and pebble-sized particles of dark greenish gray clay dispersed within the background sediment. These particles are angular to subangular and generally increase downcore toward the sediment-basement contact. Volcanic ash layers are common in Subunit IIIB and range up to 6 cm thick. They are dark gray and often bioturbated, and contain predominantly altered volcanic glass and crystals of feldspar and amphibole. Ash fall layers are not present in the two sections above the volcanic basement. In Section 165-1001A-31R-5, there are five medium-bedded sequences of dark gray to black volcanic ash layers with sharp bases and bioturbated tops. The layer at 65–95 cm depth contains 15 distinct fining-upward sequences, each with a sharp base. Minor cross-bedding occurs in some of the other layers in this section, and the layer at 132- to 148-cm depth exhibits convolute laminations. These features indicate redeposition of volcaniclastic material by sediment gravity flows. The layers contain abundant altered volcanic glass and sand-sized feldspar phenocrysts. In addition, red oxidized lithic fragments up to 1 mm in diameter are a distinctive component within the coarse base of some of the layers. The characteristics of these layers suggest input of fine-grained mafic volcaniclastic material from a nearby shallow water or emergent volcanic center (see "Igneous Petrology and Volcanology" section, this chapter).

The lower contact of Subunit IIIB records the transition from volcanic basement into sedimentary rock. In the upper part of the basement, there is a lava flow with an overlying basalt lapilli and breccia layer consisting of angular to subangular basalt clasts with remnant chilled margins (see "Igneous Petrology and Volcanology" section, this chapter). Moving up the section, there is a transition from basaltic lapilli with infilling of white calcite to dominantly calcareous limestone, with suspended clasts of basalt up to several centimeters in length (Fig. 19). Thus, the top of the lapilli unit is very poorly sorted and characterized as matrix supported. Sediments overlying the contact in Sections 165-1001A-52R-5 and 52R-6 have a distinctive reddish hue.

Discussion

Drilling in Holes 1001A and 1001B penetrated 522.8 m of section, extending from the Pleistocene into the Campanian. The oldest material collected is older than 76 Ma and consists of basaltic basement (see "Igneous Petrology and Volcanology" section, this chapter). Excellent recovery of the basement-sediment interface was achieved in both Holes 1001A and 1001B. The contact consists of a basaltic lapilli unit that has been infilled with carbonate sediment. In the interval above the basement (Subunit IIIB), carbonate deposition was accompanied by the influx of abundant volcaniclastic material. Some of this was deposited by tephra fallout, whereas other layers were produced by sediment gravity flows. The latter contain a distinctive mafic lithology with hyaloclastite grains, fragments of rounded microcrystalline basalt, and red oxidized lithics. These components are consistent with derivation from a shallow-water or emergent volcanic source that was relatively proximal to the site. The facies association of hyaloclastite and silicic tephra falls is similar to that observed adjacent to modern oceanic islands associated with hotspot activity. Influx of this material decreased rapidly between 77 and 75 Ma (see "Igneous Petrology and Volcanology" section, this chapter).

For the remainder of the Campanian Stage and throughout the Maastrichtian (Subunit IIIA), the site experienced deposition of carbonate with regular intervals of more clay-rich sediment. The strongly cyclic nature of this record suggests Milankovitch orbital forcing of carbonate depositional patterns. An important aspect of Site 1001 is the recovery of a stratigraphically nearly complete K/T boundary sequence. In Holes 1001A and 1001B, a claystone interval is present between upper Maastrichtian limestone and basal Paleocene limestone. The claystone interval consists of three fairly distinct units (Fig. 19). At the base is a dark greenish gray claystone with a distinctive shaly cleavage. This grades upward into a bluish green claystone with 1-mm-diameter spheroids of smectitic clay. This unit likely correlates with tektite fall units of the K/T boundary (see "Summary and Conclusions" section, this chapter). The uppermost part of the K/T sequence consists of a medium gray, massive claystone. This unit contains shocked quartz, and we speculate that it is likely to be enriched in iridium.

Following deposition of calcareous limestone with clay, there was a brief episode of carbonate-poor sedimentation in the earliest Paleocene (base of Subunit IIB). A similar, lower Paleocene carbonate-poor interval was recovered at Site 999. Progressively more carbonate-rich sedimentation, alternating with thin claystone laminations, started in the early late Paleocene and continued without significant breaks throughout deposition of Subunit IIA. One exception was a short interval of decreased carbonate deposition, which resulted in the deposition of a thin claystone layer in the latest Paleocene. The timing of this event suggests a correlation with a similar feature observed at Site 999, and by analogy, is interpreted to be related to a dramatic short-term warming event, referred to as the late Paleocene thermal maximum (LPTM; Zachos et al., 1993).

During the interval between the latest Campanian and the early late Paleocene, pelagic calcareous chalks occasionally accumulated thin (centimeter scale) foraminifer-rich sand layers with relatively sharp upper and lower contacts (Fig. 18), as previously recognized at Site 999. Radiolarians form a significant component of the layers at Site 999, but they are very rare in the layers recovered at Site 1001, possibly because of dissolution and consequent formation of chert. These layers are interpreted to represent the winnowing of bottom sediments by deep current activity. Formation of these features may have been facilitated by the existence of a deep passage linking the Pacific and Caribbean areas and the existence of enhanced bottom currents during this time.

Chert layers are abundant within Subunit IIA and are a distinctive character of the sedimentary sequence recovered at Site 1001. Their stratigraphic occurrence is consistent with the distribution of siliceous microfossils in the region. In fact, Caribbean sediments younger than early to middle Miocene generally lack siliceous microfossils, whereas older strata commonly contain them (Riedel and Sanfilippo, 1973). At Site 152, abundant chert layers were recovered and subdivided on the basis of color into three major types (Edgar, Saunders, et al., 1973). The better recovery achieved at Site 1001 and the imaging of chert layers with the log data constrain the distribution of silicified layers with depth.

Two major pulses of volcanic ash deposition, culminating in the early Paleocene and in the early Eocene (see "Igneous Petrology and Volcanology" section, this chapter) were superimposed on pelagic deposition of carbonate sediment during deposition of Unit II. This activity led to the accumulation of several discrete ash fall layers, ranging in thickness from less than 1 cm to up to 32 cm.

Slightly above the level approximating the middle/upper Miocene boundary interval, sediments at Site 1001 record a pronounced decrease in carbonate deposition that correlates to the carbonate crash previously documented at Sites 998, 999, and 1000. A substantial reduction in carbonate accumulation rates (see "Sedimentation Rates" section, this chapter) and poor preservation of calcareous microfossils in smear slides and washed paleontology samples suggest that carbonate dissolution and a shoaling of the lysocline and CCD are responsible for the observed patterns. Figure 12 shows the carbonate data plotted alongside the magnetic susceptibility data, using the refined stratigraphic framework based on nannoplankton biostratigraphy. The initial abrupt drop in carbonate content used to identify the boundary between lithologic Subunits IC and ID occurs within calcareous nannofossil Zone CN5 and is matched by a decrease in magnetic susceptibility and a decrease in the color reflectance in the green 550-nm wavelength (Fig. 12). In contrast to Sites 998 through 1000, low carbonate values (<40%) persist until somewhere after 9.5 Ma in calcareous nannofossil Zone CN8, whereas the latest age of low carbonate values at the previous sites was reported in calcareous nannofossil Zone CN7 at approximately 10–10.5 Ma. The sediment sequence deposited during nannofossil Zone CN7 is condensed when compared to the previous sites. Further shore-based studies of this interval, and comparisons with sites elsewhere that record this profound change in the carbonate system (e.g., Leg 138 sites in the eastern equatorial Pacific; Lyle et al., 1995), should help to identify the origins of the middle/late Miocene carbonate crash.

BIOSTRATIGRAPHY

The biostratigraphy at Site 1001 reveals a compressed Neogene section, truncated at its base by a double unconformity in Section 165-1001A-18R-4. A 28-cm interval of white chalk, assignable to the middle Eocene nannofossil Subzone CP13c, extends from 165.68 to 165.96 mbsf, and separates the middle Miocene from the lower Eocene section. These unconformities represent a total loss of section equivalent to ~38 m.y. Biostratigraphic data place the LPTM between 238.40 and 239.55 mbsf and the K/T boundary between 352.36 and 352.96 mbsf. The limestone/basalt contact is in the *Globotruncana ventricosa* Zone (planktonic foraminifers) and nannofossil Zone CC21. This nannofossil assignment suggests that the age of the limestone/basalt contact is 76.0–77.0 Ma.

Calcareous Nannofossils

We prepared standard smear slides in every core-catcher section recovered. After preliminary stratigraphy was performed on these levels, slides were made of one sample per section, close to the standard nannofossil datums in the Cenozoic section (see "Explanatory Notes" chapter, this volume; Table 2). Observations were limited to core-catcher samples in the Upper Cretaceous section. Approximately 200 slides were observed. Theoretically, the depth uncertainty of events is about 1.5 m in the highly recovered portion of Cenozoic section of Hole 1001A. Practically, this uncertainty increases significantly in poorly recovered parts of the Pleistocene, Pliocene, Eocene, and Paleocene. Poor preservation in the latter two stages and in the Upper Cretaceous also inhibits the precise determination of events. Poor preservation and recovery have led to significant disparities in depths of events between Holes 1001A and 1001B. The nannofossil datums determined at Site 1001 are compiled in Table 3, and the zonal boundaries of Okada and Bukry (1980) and Sissingh (1977) are illustrated in Figure 68. In this figure, zonal boundaries are taken from Hole 1001A, except in the upper Paleocene, where recovery was substantially better in Hole 1001B.

Preservation is generally moderate to good from the Pleistocene through the middle Miocene, and nannofossils are abundant (Core 165-1001A-1R to Section 165-1001A-18R-4; Cores 165-1001B-1R and 2R). A minor amount of etching occurs in most samples. Nannofossils are common to abundant in the middle and lower Eocene and the upper part of the upper Paleocene (Sections 165-1001A-18R-4 to 28R-CC; Sections 1001B-3R-1 to 7R-CC) and moderate etching and minor overgrowth occurs in this part of the section. Rare, heavily etched, and moderately overgrown nannofossils characterize the remainder of the Paleocene (Cores 165-1001A-29R to 38R and 165-1001B-8R to 18R) with a downward decrease in abundance and deterioration in preservation. Nannofossils are virtually absent in the two cores above the K/T boundary (Cores 165-1001A-36R to 38R and 165-1001B-16R to 18R). Preservation in the Upper Cretaceous section is moderate to poor with moderate etching and overgrowth, and rare to few nannofossils are observed. Slightly improved preservation was observed in thin claystone bands and in sediments in the two cores above basement (Cores 165-1001A-51R and 52R and 165-1001B-31R and 32R), where clay contents increased.

Neogene

Nannofossil biostratigraphy indicates that the Pleistocene to middle Miocene section at Site 1001 is separated from the Paleogene section by two unconformities that lie in Section 165-1001A-18R-4. The Neogene section was deposited at moderately high sedimentation rates, averaging 14 m/m.y. in the Pleistocene to upper Miocene and decreasing to less than 7 m/m.y. in the middle Miocene. Poor recovery prevents determination of the completeness of sections, and several events are often clustered at the same core break (Table 3); however, most of the Cenozoic zones and subzones of Okada and Bukry (1980) can be recognized (Fig. 68; Table 3). A moderate amount of reworking is observed sporadically throughout the section. The presence of *Cyclicargolithus floridanus, Discoaster variabilis,* large (6–8 µm) specimens of *Reticulofenestra pseudoumbilicus, Sphenolithus moriformis,* and *S. heteromorphus* in samples of Pliocene and Pleistocene age indicates that this reworking is from an early to middle Miocene source. Reworking also hinders precise determination of biostratigraphic events, particularly the last occurrences (LOs) of *Sphenolithus* spp. and *R. pseudoumbilicus,* both of which are commonly reworked. We determined these two events by noting the level below which abundance increased significantly and occurrence became continuous. In the case of *R. pseudoumbilicus,* reworked specimens from the Miocene tend to be larger (6–8 µm) than those close to the LO of this species (5–6 µm).

The uppermost sample recovered (Sample 165-1001A-1R-CC) lies in Subzone CN14b, below the first occurrence (FO) of *Emiliania huxleyi,* but above the last occurrence (LO) of *Pseudoemiliania lacunosa.* The Pleistocene and upper Pliocene zonal markers of Okada and Bukry (1980) and the biohorizons of Takayama and Sato (1987) and Sato et al. (1991) are clustered in individual samples due to poor recovery. *Reticulofenestra asanoi* and large (5–6 µm) specimens of *Gephyrocapsa* were observed in one sample each (Samples 165-1001A-3R-1, 70 cm, and 4R-CC, respectively). The LO of *Helicosphaera sellii* was found to lie between Samples 165-1001A-3R-CC and 4R-CC. Several events lie between Samples 165-1001A-4R-CC and 5R-1, 70 cm, including the FOs of *Gephyrocapsa oceanica* and *G. caribbeanica* and the LOs of *Calcidiscus macintyrei* and *Discoaster brouweri.* The Pliocene/Pleistocene boundary also lies in this interval. Numerous specimens of *D. brouweri* (and other discoasters) were observed above this level; however, they are considered to be reworked. Sample 165-1001A-5R-CC was found to contain *Discoaster pentaradiatus, D. tamalis,* and *D. surculus;* thus, the LOs of these species lie between this sample and 165-1001A-5R-1, 70 cm.

The LOs of common *Sphenolithus* spp. (mostly *S. abies*) and *R. pseudoumbilicus* lie between Samples 165-1001A-8R-1, 70 cm, and 8R-2, 70 cm, and between Samples 165-1001A-8R-3, 70 cm, and 8R-4, 70 cm, respectively. Poor recovery in Core 165-1001A-10R prevented division of Zone CN10 as no specimens of *Ceratolithus acutus* were observed and the FO of *C. rugosus* lies within this interval.

Table 3. Nannofossil datums, absolute ages, and depths at Site 1001.

			Hole 1001A		Hole 1001B	
Event	Zone (base)	Age (Ma)	Core, section, interval (cm)	Depth (mbsf)	Core, section, interval (cm)	Depth (mbsf)
B *Emiliania huxleyi*	CN15	0.248	Above uppermost sample			
T *Pseudoemiliania lacunosa*	CN14b	0.408	1R-CC to 2R-CC	3.61		
T *Reticulofenestra asanoi*		0.88	2R-CC to 3R-1, 70	12.00		
B *Gephyrocapsa parallela*	CN14a	0.94	3R-1, 70, to 3R-CC	17.38		
B *Reticulofenestra asanoi*		1.17	3R-1, 70, to 3R-CC	17.38		
T large *Gephyrocapsa* spp.		1.23	3R-CC to 4R-CC	22.23		
T *Helicosphaera sellii*		1.26	3R-CC to 4R-CC	22.23		
B large *Gephyrocapsa* spp.		1.48	4R-CC to 5R-1, 70	31.19		
B *Gephyrocapsa oceanica*		1.64	4R-CC to 5R-1, 70	31.19		
T *Calcidiscus macintyrei*		1.64	4R-CC to 5R-1, 70	31.19		
B *Gephyrocapsa caribbeanica*	CN13b	1.71	4R-CC to 5R-1, 70	31.19		
T *Discoaster brouweri*	CN13a	1.95	4R-CC to 5R-1, 70	31.19		
T *Discoaster pentaradiatus*	CN12d	2.36	5R-1, 70, to 5R-CC	36.36		
T *Discoaster surculus*	CN12c	2.51	5R-1, 70, to 5R-CC	36.36		
T *Discoaster tamalis*	CN12b	2.82	5R-1, 70, to 5R-CC	36.36		
T *Sphenolithus* spp.		3.62	8R-1, 70, to 8R-2, 70	65.65		
T *R. pseudoumbilicus*	CN12a	3.83	8R-3, 70, to 8R-4, 70	68.65		
T *Amaurolithus* spp.	CN11	4.50	9R-2, 69, to 9R-CC	76.63		
B *Ceratolithus rugosus*	CN10c	5.046	10R-2, 69, to 10R-CC	86.04		
T *Ceratolithus acutus*		5.046	10R-2, 69, to 10R-CC	86.04		
B *Ceratolithus acutus*	CN10b	5.089	10R-2, 69, to 10R-CC	86.04		
T *Discoaster quinqueramus*	CN10a	5.537	11R-1, 70, to 11R-2, 70	94.45		
B *Amaurolithus* spp.	CN9b	7.392	12R-CC to 13R-1, 70	111.80		
B *Discoaster berggrenii*	CN9a	8.281	13R-7, 70, to 13R-CC	121.95		
T *Discoaster hamatus*	CN8a	9.635	15R-5, 70, to 15R-6, 70	138.95		
B *Discoaster hamatus*	CN7	10.476	15R-CC to 16R-1, 70	141.22		
B *Catinaster coalitus*	CN6	10.794	16R-2, 70, to 16R-3, 70	143.95		
T *Cyclicargolithus floridanus*		13.23	17R-CC to 18R-1, 109	161.39		
B *Discoaster lodoensis*	CP10	52.0	19R-CC to 20R-CC	169.89		
T *Fasciculithus tympaniformis*		55.3	26R-CC to 27R-1,79	234.10	5R-CC to 6R-1, 29	232.31
B *Discoaster multiradiatus*	CP8	56.2	29R-CC to 31R-CC	267.79	8R-CC to 9R-1, 10	262.29
B *Discoaster mohleri*	CP6	57.5	31R-CC to 32R-1, 6	280.60	11R-2, 30 to 11R-3, 28	285.94
B *Heliolithus kleinpellii*	CP5	58.4	33R-1, 113, to 33R-2, 110	296.77	12R-1, 0 to 12R-2, 0	293.65
B *Fasciculithus tympaniformis*	CP4	59.7	36R-2, 149, to 36R-4, 17	327.63	15R-4, 62 to 15R-5, 98	327.70
B *Fasciculithus* spp.		59.9	36R-2, 149, to 36R-4, 17	327.63	15R-5, 98 to 15R-CC	328.72
B *Sphenolithus primus*		60.6	36R-4, 17, to 36R-5, 21	329.24	16R-1, 45 to 16R-2, 4	332.45
B *Cruciplacolithus primus*		64.8	37R-8, 30, to 38-CC, 0	348.07	17R-4, 62 to 17R-CC	346.26
T Cretaceous spp.	CP1a	65.0	38-CC, 0, to 38-CC, 33	352.19	17R-CC to 18R-CC	350.50
B *Micula murus*		66.2	40R-CC to 41R-CC	373.75	19R-CC to 20R-CC	365.38
T *Quadrum trifidum*		71.3	45R-CC to 46R-CC	420.29	25R-CC to 26R-CC	419.04
T *Aspidolithus parcus*		74.5	48R-CC to 49R-CC	448.24	28R-CC to 29R-3, 23	444.65
T *Eiffellithus eximius*	CC23*	75.0	49R-CC to 50R-CC	459.81	29R-3, 23 to 29R-CC	450.12
B *Quadrum trifidum*	CC22	76.0	51R-CC to 52R-3, 149	478.00	30R-CC to 31R-CC	470.67

Notes: T = top of species range (last appearance datum), B = base of species range (first appearance datum). * = secondary marker is used to define zone. This entire table also appears on CD-ROM (back pocket).

The Miocene/Pliocene boundary correlates with this coring gap. The section immediately below this interval of poor recovery lies in Zone CN9 based on the occurrence of common, well-preserved specimens of *Discoaster quinqueramus.* The base of this zone, defined by the FO of *D. berggrenii,* is more difficult to detect as the central knob is less prominent in the earliest specimens of this species. We saw few specimens of *Discoaster loeblichii,* the FO of which defines the base of Subzone CN8b, and therefore cannot divide Subzones CN8a and CN8b in Hole 1001A. Very few, small specimens of *Discoaster hamatus* in Samples 165-1001A-15R-6, 70 cm, and 15R-CC indicate a Zone CN7 of reduced thickness, and a potential unconformity at the top of this interval.

The lowest Neogene sediments in Hole 1001A are placed in Zone CN5 based on the absence of *Catinaster coalitus* and *Sphenolithus heteromorphus;* a few specimens of *S. heteromorphus* occur in isolated samples and are thought to be reworked. In Hole 1001B, the lowest Neogene sample observed was from Section 165-1001B-2R-CC and contains abundant specimens of *Sphenolithus belemnos* and only one specimen of *S. heteromorphus,* indicating correlation to Zone CN2. The remainder of the nannofossil assemblage, abundant *Cyclicargolithus floridanus,* common *Cyclicargolithus abisectus,* and *Discoaster deflandrei,* is consistent with this age. Observations of slumping in this core and the presence of a foraminiferal assemblage indicative of Zone N12 suggest that the nannofossils have been reworked into younger material equivalent to Zone CN5. As the latter interval zone is based on the absences of *C. coalitus* and *S. heteromorphus,* it is difficult to detect in a spot-cored record.

Paleogene

The Neogene section is separated from the Paleogene by two unconformities, which lie at 88–90 and 116 cm in Section 165-1001A-18R-4. In this section, light green chalk of middle Miocene age (Zone CN5; 0–88 cm) unconformably overlies a 28-cm interval of white chalk of middle Eocene age. Samples from this chalk contain *Nannotetrina fulgens,* but no *Chiasmolithus gigas* or *Reticulofenestra umbilicus.* Based on these observations, this interval could correlate to either Subzone CP13a or CP13c, but the latter subzone is indicated by the occurrence of specimens of *Reticulofenestra* between 8 and 11 µm in diameter with large openings. These morphotypes are commonly observed in the interval just below the FO of *R. umbilicus* in Subzone CP13c (e.g., Backman and Hermelin, 1986). Immediately below the white chalk at 116 cm is a 1–2 cm layer of chert that caps a tan chalk of early Eocene (Zone CP10) age. This age is indicated by the occurrence of *Discoaster lodoensis,* and the absence of *Coccolithus crassus* and *D. sublodoensis.* In summary, Section 165-1001A-18R-4 contains two unconformities, which represent gaps of approximately 30 and 8 m.y.

Recovery in the underlying Eocene section is extremely poor due to the occurrence of common intervals of chert and siliceous limestone. However, available biostratigraphy indicates a sedimentation rate of 19 m/m.y. The interval between Sample 165-1001A-18R-4, 117 cm, and 19R-CC lies in Zone CP10, based on the occurrence of *Discoaster lodoensis.* The absence of this species and the occurrence of a diverse array of discoasters including *D. salisburgensis, D. ele-*

gans, D. barbadiensis, and *D.* cf *D. diastypus* suggest that the interval between Samples 165-1001A-20R-CC and 26R-CC and the interval between Samples 165-1001B-3R-CC and 5R-CC lie in Zone CP9. No specimens of *Tribrachiatus* were observed at Site 1001. In other locations, the ranges of *T. bramlettei* and *T. contortus* are restricted to Zone CP9. The FO of the former species defines the base of this zone, and the LO of *T. contortus* defines the base of Subzone CP9b. The absence of these species has also been noted in other tropical pelagic lower Eocene sequences such as Sites 865 (Bralower and Mutterlose, 1995) and 999. The base of Zone CP9 is also defined by the FO of *D. diastypus;* however, this species can only be strictly identified in side view (e.g., Aubry, 1988), and determination of its range will require further investigation.

The Paleocene/Eocene boundary cannot be identified on the basis of nannofossil biostratigraphy (e.g., Aubry et al., 1988), but it lies above the LO of *Fasciculithus* spp., which correlates with the upper part of Zone CP8 (e.g., Backman, 1984; Aubry et al., 1996). This event lies between Samples 165-1001A-26R-CC and 27R-1, 79 cm, and Samples 165-1001B-5R-CC and 6R-1, 29 cm. The LPTM interval (Zachos et al., 1993) is thought to correlate to the prominent claystone in Sections 165-1001A-27R-2 and 165-1001B-6R-4. Smear slides in this claystone include rare, highly etched nannofossils, indicating a major change in carbonate dissolution, carbonate productivity, or terrestrial flux.

The Paleocene section was deposited at highly variable sedimentation rates, between approximately 4 and 19 m/m.y. We had some difficulty determining the FO of *Discoaster multiradiatus* at Site 1001. In Holes 1001A and 1001B, an early form of this species transitional with the ancestral *Discoaster megastypus* has a range that extends below the FO of *Discoaster mohleri* into Zone CP5. This form, which has a minute distal shield prominent in cross-polarized light, has previously been included in *D. multiradiatus* (e.g., Perch-Nielsen, 1985; Aubry, 1984, 1989). We restrict definition of *D. multiradiatus* to specimens without distal shields. We could not determine the base of Zone CP7 (e.g., Fig. 68), as *D. nobilis* is rare in samples from the upper Paleocene. The bases of Zones CP6, CP5, and CP4 can be precisely determined in both holes by the FOs of *D. mohleri, Heliolithus kleinpellii,* and *Fasciculithus tympaniformis,* respectively. Deteriorating preservation and extremely impoverished nannofloras prevented subdivision of the remainder of the lower Paleocene. No specimens of *Ellipsolithus macellus* were observed below the uppermost Paleocene, and thus the base of Zone CP3 could not be determined. Both *Sullivania danica* and *Cruciplacolithus tenuis* are very rare, preventing accurate determination of the base of Zone CP2 and Subzone CP1b. The only event that can be determined is the FO of *Cruciplacolithus primus.* However, no samples were observed above the core catchers in Cores 165-1001A-38R and 165-1001B-18R; thus, the range of this species (Table 3) must be viewed as preliminary. Reworked Cretaceous species (*Cribrosphaerella ehrenbergii, Cretarhabdus surirellus, Cylindralithus* sp., *Micula decussata,* and *Watznaueria barnesae*) occur sporadically throughout the lower Paleocene.

Cretaceous

Because of reworking and the absence of sampling in the boundary interval, the K/T boundary, which can be approximated by the last in situ occurrence of Cretaceous nannofossils, cannot be precisely determined at this time. However, reworked nannofossils within the boundary clay (layer B) yield a mixture of assemblages of at least two different ages. One assemblage derives from the Santonian–Campanian and includes *Eiffellithus eximius* and *Aspidolithus parcus,* among other species. The other includes *Nannoconus steinmannii* and *Rucinolithus terebrodentarius,* suggesting an age range between late Hauterivian and early Aptian. This latter assemblage indicates that at least part of the fine fraction was derived from distant sources, along the continental margin of Central America, or possibly the Yucatan.

The Upper Cretaceous section was deposited at average rates of 11 m/m.y. Nannofossil preservation improves in the Upper Cretaceous chalk and limestone, and the ranges of *Micula murus, Quadrum trifidum,* and *Quadrum gothicum* have been determined confidently, although only core-catcher samples have been observed (Table 3). *Micula murus* has been observed in Sections 165-1001A-39R-CC, and 40R-CC, and in Sections 165-1001B-18R-CC and 19R-CC, indicating a relatively expanded upper Maastrichtian section. The Campanian/Maastrichtian boundary, which can be approximated by the LO of *Q. trifidum,* lies between Samples 165-1001A-45R-CC and 46R-CC and between Samples 165-1001B-25R-CC and 26R-CC (Fig. 68). The Upper Cretaceous assemblage is of low diversity, and several zonal markers, including *Nephrolithus frequens* (FO defines base of Zone CC26), *Reinhardtites levis* (LO defines base of Zone CC25), and *Tranolithus orionatus* (LO defines base of Zone CC24) either have not been observed or are very rare. The base of Zone CC23, defined by the LO of *Reinhardtites anthophorus,* can be approximated by the FO of *Eiffellithus eximius* (Bralower and Siesser, 1992) between Samples 165-1001A-49R-CC and 50R-CC and Samples 165-1001B-29R-3, 23 cm, and 29R-CC. The oldest sediments cored in both Holes 1001A and 1001B lie just below the FO of *Quadrum trifidum,* which occurs between Samples 165-1001A-51R-CC and 52R-3, 149 cm, and 1001B-30R-CC and 31R-CC. The presence of *Quadrum gothicum* in samples taken several decimeters above basement in Hole 1001A indicate correlation to mid-Campanian Zone CC21 (Fig. 68), the age of which ranges from 76 to 77 Ma (Erba et al., 1995).

Planktonic Foraminifers

At Hole 1001A, foraminifer studies were primarily limited to core-catcher samples. Exceptions were Sections 165-1001A-39R-2, and 54R-5, which were sampled to constrain biostratigraphically the K/T boundary and basement age. In general, the occurrence data of planktonic foraminiferal zonal markers correlate well between Holes 1001A and 1001B.

Preservation through the Neogene section is very good down to Section 165-1001A-7R-CC. Below this level, preservation abruptly declines. The poor preservation manifests itself as an increase in the abundance of test fragments. Lithification becomes much more pronounced in the Paleogene and Upper Cretaceous section, and planktonic foraminifers can only be recovered from samples by increasingly brutal extraction techniques (i.e., hydraulic crushing and ultrasonification before washing).

Neogene

The FO of *Truncorotalia truncatulinoides* marks the base of Zone N22 (2.0 Ma) between Samples 165-1001A-4R-CC and 5R-CC. Other occurrence data that are constrained in this zone include the LO of *Globigerinoides obliquus,* located between Samples 165-1001A-3R-CC and 4R-CC (1.3 Ma), and the LO of *Globigerinoides extremus* between Samples 165-1001A-4R-CC and 5R-CC (1.9 Ma). *Truncorotalia tosaensis* is only observed in Sample 165-1001A-6H-CC. This single occurrence places the base of Zone N21 between Sections 165-1001A-6H-CC and 7H-CC. The base of Zone N20 (3.6 Ma) is marked by the FO of *Menardella miocenica* between Samples 165-1001A-7R-CC and 8R-CC. The LO of *Hirsutella margaritae,* which should be at the same level as the FO of *M. miocenica,* is instead between Samples 165-1001A-8R-CC and 9R-CC at this site. Other lower Pliocene events are found in their proper sequence; however, because of the thinness of the section, many events are found between the same two core catchers (Table 4).

The uppermost Miocene datum is the FO of *Sphaeroidinella dehiscens* between Samples 165-1001A-10R-CC and 11R-CC. This da-

Table 4. Planktonic foraminifer datums, absolute ages, and depths at Site 1001.

Event	Zone (base)	Age (Ma)	Hole 1001A Core, section, interval (cm)	Hole 1001A Depth (mbsf)	Hole 1001B Core, section, interval (cm)	Hole 1001B Depth (mbsf)
LO *Globigerinoides obliquus*		1.3	3R-CC to 4R-CC	22.23		
LO *Globigerinoides extremus*		1.9	4R-CC to 5R-CC	31.55		
FO *Truncorotalia truncatulinoides*	N22	2.0	4R-CC to 5R-CC	31.55		
LO *Menardella miocenica*		2.3	4R-CC to 5R-CC	31.55		
FO *Pulleniatina obliquiloculata* (Atlantic)		2.3	4R-CC to 5R-CC	31.55		
LO *Menardella pertenuis*		2.6	5R-CC to 6R-CC	41.87		
LO *Menardella multicamerata*		3.0	6R-CC to 7R-CC	52.81		
LO *Dentoglobigerina altispira*		3.0	6R-CC to 7R-CC	52.81		
FO *Menardella pertenuis*		3.5	7R-CC to 8R-CC	65.21		
FO *Menardella miocenica*	N21/N20	3.6	7R-CC to 8R-CC	65.21		
LO *Hirsutella margaritae*		3.6	8R-CC to 9R-CC	74.53		
LO *Globoturborotalita nepenthes*		4.3	8R-CC to 9R-CC	74.53		
LO *Globorotalia plesiotumida*		4.4	8R-CC to 9R-CC	74.53		
FO *Menardella exilis*		4.5	9R-CC to 10R-CC	81.87		
FO *Truncorotalia crassaformis*		4.7	9R-CC to 10R-CC	81.87		
LO *Hirsutella cibaoensis*		5.0	10R-CC to 11R-CC	94.09		
FO *Sphaeroidinella dehiscens*	N19	5.6	10R-CC to 11R-CC	94.09		
FO *Hirsutella margaritae*		6.0	9R-CC to 10R-CC	81.87		
FO *Globigerinoides conglobatus*		6.2	9R-CC to 10R-CC	81.87		
FO *Hirsutella cibaoensis*		7.7	11R-CC to 12R-CC	106.20		
FO *Globigerinoides extremus*		8.0	11R-CC to 12R-CC	106.20		
FO *Candeina nitida*		8.0	13R-CC to 14R-CC	125.81		
FO *Hirsutella juanai*		8.0	13R-CC to 14R-CC	125.81		
FO *Globorotalia plesiotumida*	N18/N17	8.2	13R-CC to 14R-CC	125.81		
FO *Neogloboquadrina acostaensis*	N16	10.0	14R-CC to 15R-CC	135.18		
LO *Paragloborotalia mayeri*	N15	10.3	14R-CC to 15R-CC	135.18		
FO *Globoturborotalita nepenthes*	N14	11.4	14R-CC to 15R-CC	135.18		
LO *Fohsella fohsi*	N13	11.8	15R-CC to 16R-CC	145.12		
FO *Fohsella fohsi*	N12	12.7	16R-CC to 17R-CC	155.02		
FO *Fohsella praefohsi*	N11	14.0	17R-CC to 18R-CC	163.59		
			Unconformity			
LO *Subbotina velascoensis*		53.5	18R-CC to 19R-CC	167.50		
LO *Morozovella velascoensis*	P6a	54.7	25R-CC to 26R-CC	225.32	4R-CC to 5R-CC	223.51
LO *Morozovella acuta*		54.7	19H-CC to 22R-CC	178.98	4R-CC to 5R-CC	223.51
FO *Morozovella gracilis*		54.7 (54.9)	24R-CC to 25R-CC	215.58		
FO *Igorina broedermanni*		54.7	23R-CC to 24R-CC	205.36	4R-CC to 5R-CC	223.51
FO *Morozovella subbotinae*		55.9	29R-CC to 30R-CC	263.12	7R-CC to 8R-CC	256.92
LO *Globanomalina pseudomenardii*	P5	55.9	29R-CC to 31R-CC	262.99	7R-CC to 8R-CC	256.92
LO *Acarinina nitida*		56.3			5R-CC to 7R-CC	241.20
FO *Acarinina soldadoensis*	P4c	56.5	31R-CC to 32R-CC	278.50	9R-CC to 10R-CC	272.30
FO *Morozovella aequa*		56.5	32R-CC to 33R-CC	295.15	9R-CC to 10R-CC	272.30
FO *Globanomalina pseudomenardii*	P4a	59.2	35R-CC to 36R-2, 149–150	325.38	11R-CC to 12R-CC	295.32
FO *Morozovella velascoensis*		60.0	34R-CC to 35R-CC	317.39	13R-CC to 14R-CC	316.61
FO *Igorina albeari*	P3b	60.0	35R-CC to 36R-2, 149–150	325.38	15R-CC to 16R-CC	334.93
FO *Morozovella angulata*	P3a	61.0	35R-CC to 36R-2, 149–150	325.38	15R-CC to 16R-CC	334.93
FO *Igorina pusilla*		61.0	36R-2, 149 to 37R-CC	334.90	14R-CC to 15R-CC	324.93
FO *Praemurica uncinata*	P2	61.2			15R-CC to 16R-CC	334.93
FO *Morozovella praeangulata*		61.2	36R-2, 149 to 37R-CC	334.90		
FO *Praemurica inconstans*		63.0			16R-CC to 17R-CC	343.82
FO *Subbotina triloculinoides*	P1b	64.3	37R-CC to 38R-CC	348.36	16R-CC to 17R-CC	343.82
LO Most Cretaceous taxa	P0/Pα	65.0	38R-CC to 39R-2, 4	352.66	17R-CC to 18R-CC	350.50
FO *Abathomphalus mayaroensis*	*A. mayaroensis*	68.25	43R-CC to 44R-CC	404.24	22R-CC to 23R-CC	393.70
FO *Contusotruncana contusa*		69.6	42R-CC to 43R-CC	393.93	19R-CC to 20R-CC	365.38
FO *Gansserina gansseri*	*G. gansseri*	72.8	46R-CC to 47R-CC	430.28	26R-CC to 27R-CC	428.25
FO *Globotruncana aegyptiaca*	*G. aegyptiaca*	73.8	47R-CC to 48R-CC	439.27	27R-CC to 28R-CC	436.52
LO *Globotruncanita calcarata*	*G. havanensis*	75.2	49R-CC to 50R-CC	459.81	29R-CC to 30R-CC	457.58
FO *Globotruncanita calcarata*	*G. calcarata*	75.7	50R-CC to 51R-CC	470.04	30R-CC to 31R-5, 89–90	469.59
FO *Globotruncana ventricosa*	*G. ventricosa*	79.5	below 51R-CC			

Notes: FO = first occurrence, LO = last occurrence. This entire table also appears on CD-ROM (back pocket).

tum defines the base of Zone N19 at 5.6 Ma. The FOs of *Hirsutella margaritae* and *Globigerinoides conglobatus,* which should be found below the base of Zone N19, instead are found within that zone between Samples 165-1001A-9R-CC and 10R-CC. As at other Leg 165 sites, the FO of *Globorotalia tumida* could not be reliably associated with the base of Zone N18. At Site 1001, the lowest observation of *G. tumida* is in Sample 165-1001A-8R-CC in Zone N19. Because of the sporadic stratigraphic distribution of this marker taxon, we again combined Zones N18 and N17. The base of this combined zone is identified by the FO of *Globorotalia plesiotumida* (8.2 Ma) between Samples 165-1001A-13R-CC and 14R-CC. The FOs of *Hirsutella juanai* and *Candeina nitida* (both 8.0 Ma) are also between Samples 165-1001A-13R-CC and 14R-CC, but the FO of *Globigerinoides extremus* (also 8.0 Ma) lies between Samples 165-1001A-11R-CC and 12R-CC.

The FO of *Neogloboquadrina acostaensis* marks the base of Zone N16 between Samples 165-1001A-14R-CC and 15R-CC. This coincides with the LO of *Paragloborotalia mayeri* and the FO of *Globoturborotalita nepenthes.* Because the latter events define the bases of Zones N15 and N14, respectively, those zones are not distinguishable from Zone N16 at the present level of sample spacing.

The base of Zone N13 is marked by the LO of *Fohsella* species between Samples 165-1001A-15R-CC and 16R-CC. The FO of *Fohsella fohsi* places the base of Zone N12 between Samples 165-1001A-16R-CC and 17R-CC. No specimens of *F. fohsi robusta* or *F. fohsi lobata* were found in samples examined at this site. The oldest Neogene zone identified at this site is Zone N11, which is recognized by the absence of *F. fohsi* and the presence of *Fohsella praefohsi* (14.0 Ma). This zone is truncated by the unconformity between Samples 165-1001A-17R-CC and 18R-CC. This major unconformity spans the early Eocene to middle Miocene record at Hole 1001A.

Paleogene

The youngest Paleogene sediments examined at Site 1001 have been assigned to lower Eocene foraminifer Zone P6a (the 28-cm interval of middle Eocene white chalk in Section 165-1001A-18R-4 was not examined shipboard for planktonic foraminifers). The core-catcher samples from Cores 165-1001A-18R and 165-1001B-3R are both directly below the unconformity. They lack *Morozovella formosa* (its FO marks the base of Subzone P6b) and overlie the LO of *Morozovella velascoensis,* which defines the base of Subzone P6a. The base of Subzone P6a occurs between Samples 165-1001A-25R-6, 12 cm, and 26R-CC and between Samples 165-1001B-4R-CC and 5R-CC. Thus, the Paleocene/Eocene (P5/P6a) boundary is placed at ~225.32 mbsf in Hole 1001A and at ~223.51 mbsf in Hole 1001B.

The base of foraminifer Zone P5 is marked by the LO of *Globanomalina pseudomenardii* between Samples 165-1001A-29R-CC and 30R-CC, and between Samples 165-1001B-7R-CC and 8R-CC. The base of Zone P4 is defined by the FO of *Globanomalina pseudomenardii* between Samples 165-1001A-35R-CC and 36R-2, 149 cm (325.38 mbsf), and between Samples 1001B-11R-CC and 12R-CC (295.32 mbsf). The depth difference probably reflects its solution susceptibility and consequent relative rarity in these samples. In contrast, the depths of the FOs of the more robust species *Acarinina soldadoensis, Igorina albeari,* and *Morozovella angulata,* which mark the bases of Subzones P4c, P3b, and P3a, respectively, occur within 10 m in Holes 1001A and 1001B (Table 4).

Zone P2 was not identified at Site 1001, probably due to the shortness of that zone and the relatively wide spacing of core-catcher samples examined. However, the base of Subzone P1b, defined by the FO of *Subbotina triloculinoides,* lies between Samples 165-1001A-37R-CC and 38R-CC (348.36 mbsf) and between Samples 165-1001B-16R-CC and 17R-CC (343.82 mbsf). The base of Subzone P1a was not identified in our samples, again probably due to a low sedimentation rate, brevity of the zone, and wide sample spacing.

Cretaceous/Tertiary Boundary

As defined by thin-section analyses of planktonic foraminifers, the K/T boundary lies between Samples 165-1001A-38R-CC, 1 cm, and 39R-2, 4 cm. A thin section of the first sample contains a planktonic foraminifer fauna comprised of rare tiny planktonic foraminifers and dominated by *Guembelitria cretacea.* Because of the difficulty of identifying *Parvularugoglobigerina eugubina* in thin section, Sample 165-1001A-38R-CC, 1 cm, is assigned to a combined early Paleocene Zone P0/Pα. In contrast, the thin section from Sample 165-1001A-38R-2, 4 cm, contains abundant and diverse Maastrichtian planktonic foraminifers and is assigned to the Late Cretaceous *Abathomphalus mayaroensis* Zone.

Late Cretaceous

Abathomphalus mayaroensis, the uppermost Cretaceous zonal marker, is rarely observed at Site 1001. Nonetheless, the base of the *A. mayaroensis* Zone lies between Samples 165-1001A-43R-CC and 44R-CC (404.24 mbsf) and between Samples 165-1001B-22R-CC and 23R-CC (393.70 mbsf) based on the FO of the nominate taxon. The base of the *Gansserina gansseri* Zone lies between Samples 165-1001A-46R-CC and 47R-CC (430.28 mbsf) and between Samples 165-1001B-26R-CC and 27R-CC (428.25 mbsf), again based on the FO of the nominate taxon. The base of the *Globotruncana aegyptiaca* Zone is marked by the FO of its nominate taxon between Samples 165-1001A-47R-CC and 48R-CC (439.27 mbsf) and between Samples 165-1001B-27R-CC and 28R-CC (436.52 mbsf).

Free tests of *Globotruncanita calcarata* are extremely rare at Site 1001. Nonetheless, we are able to define the base of the *Globotruncanella havanensis* Zone by the LO of *Globotruncanita calcarata* between Samples 165-1001A-49R-CC and 50R-CC (459.81 mbsf) and between Samples 165-1001B-29R-CC and 30R-CC (457.58 mbsf). The base of the *Globotruncanita calcarata* Zone is marked by the FO of the nominate taxon between Samples 165-1001A-50R-CC and 51R-CC (470.04 mbsf) and between Samples 165-1001B-30R-CC and 31R-5, 89–90 (469.59 mbsf).

Limestone/Basalt Biostratigraphy and Age Estimates

Sediments immediately above basement are assignable to the *Globotruncana ventricosa* Zone, based on the combined absence of *Globotruncanita calcarata* and the presence of the nominate taxon. In Hole 1001A, a thin section was prepared from a sample (Sample 165-1001A-54R-5, 10–14 cm) that included a pocket of limestone within the basalt. Several planktonic foraminifer species, including *G. ventricosa,* were identified. This biostratigraphic evidence suggests that the sediment, which was recovered approximately 10 m below the sediment/basalt contact, is not significantly older than sediments at the top of the basement sequence (79.5–75.7 Ma).

Sample 165-1001B-31R-5, 89–90 cm, was taken from an ash turbidite just above basement. In addition to the marker taxon, *G. ventricosa,* several specimens of *Globotruncanita elevata* were found. According to Robaszynski et al. (1984), the LO of *G. elevata* is below the FO of *G. ventricosa.* It is possible that older material has been reworked in this turbiditic sequence, or that the range of *G. elevata* needs revision. In general, the biostratigraphic evidence from Hole 1001B suggests an age estimate for the basement contact that agrees with that of Hole 1001A.

Benthic Foraminifers

Foraminifers were examined in thin section from several limestones within the basalt, as well as in washed residues from several intervals in the basal limestone overlying the basalt. The fossiliferous limestones within the basalt occur as stringers between the flows. These samples contain rare to few foraminifers in a matrix of micrite. Planktonic specimens outnumber benthic specimens, and biserial planktonic taxa (i.e., *Heterohelix* species) appear to be the most common. In Sample 165-1001A-54R-5, 10–14 cm (499.64 mbsf), several thick-walled benthic foraminifers are present. In addition to the foraminifers, rare radiolarians, sponge spicules, and other unidentified biota were observed in the limestones from within the basalt flows.

The contact between the basalt and the overlying mid-Campanian limestone is in Sample 165-1001A-52R-6, 70 cm (485.4 mbsf). Washed residues from this limestone contain abundant foraminifers. Sample 165-1001A-52R-5, 45–47 cm (483.77 mbsf), contains roughly equal numbers of planktonic and benthic foraminifers, including very numerous small-sized benthic specimens (<250 μm). Preservation of this sample is moderately poor to poor. Characteristic benthic foraminifers include *Gavelinella* sp., *Gyroidinoides, Praebulimina, Dorothia oxycona, Stensioina,* and *Pleurostomella.* The high ratio of benthic to planktonic foraminifers and the composition of the benthic assemblage suggests an outer neritic to upper bathyal depositional paleoenvironment. Sample 1001A-52R-4, 104–106 cm (483.24 mbsf), is slightly better preserved and contains many of the same species of benthic foraminifers. However, planktonic specimens greatly outnumber benthic specimens in this sample and *Stensioina* was not observed. The addition of *Osangularia cordieriana, Gaudryina,* and *Spiroplectammina* further distinguishes this sample from the one below it and suggests a bathyal environment of deposition.

A sample from a turbidite in Sample 165-1001B-31R-5, 89–90 cm (474.55 mbsf), contains a moderately preserved and diverse planktonic foraminiferal assemblage of the *Globotruncana ventricosa* Zone, rare benthic foraminifers of possible mixed neritic and upper bathyal affinities, and echinoderm spines. Characteristic benthic taxa include *Gavelinella, Lenticulina, Pullenia, Gyroidinoides, Praebulimina, Pleurostomella, Osangularia cordieriana, Dorothia oxycona, Oolina, Neoeponides*?, and *Tritaxia*?. Taken together, the preliminary evidence from the basalt and overlying limestone may indicate relatively rapid subsidence of the area following emplacement of the lavas, and/or proximity to a source of redeposited neritic benthic foraminifers.

PALEOMAGNETISM

The remanent magnetization of the archive-half sections of RCB cores from Hole 1001A and 1001B were measured at 10-cm intervals using the pass-through cryogenic magnetometer, except for most of the basalt sections, which were measured at 5-cm intervals. After measuring the natural remanent magnetization (NRM), the sections were partially demagnetized in peak alternating fields (AF) of 20 mT, except for most of the basalt sections, which were partially demagnetized at 10, 20, and 25 mT. Section 165-1001B-18R-5, which contains the K/T boundary, was not split during Leg 165 and therefore was not measured.

The NRM intensities (Fig. 22) range from about 10 to 45 mA/m, with an average of about 25 mA/m above 155 mbsf; they then drop precipitously to values less than 10 mA/m, except for a few spikes. Between 155 and 485 mbsf, there are two intervals with relatively high values: one between 230 and 270 mbsf that corresponds to the volcanic episode in the lower Eocene; and one between 305 and 352 mbsf that corresponds to a Paleocene volcanic episode and to the clay-rich interval above the K/T boundary. The intensity values increase just above basement owing to the occurrence of several thick mid-Campanian volcanic ash layers. Values in the basaltic basement are mainly between 2000 and 6000 mA/m. The susceptibility correlates well with the intensity (Fig. 22), thus showing the same major anomalies as listed above. Furthermore, both susceptibility and intensity can be easily correlated between Holes 1001A and 1001B (see "Physical Properties" section, this chapter).

In the Upper Cretaceous, immediately below the K/T boundary, a significant difference is observed between Holes 1001A and 1001B in the magnitude of both susceptibility and NRM intensity (see Fig. 54); the magnitude of these parameters is two to five times higher in Hole 1001A than in the equivalent intervals of Hole 1001B. A possible explanation for the difference is that fluid flow appears to have been more intense and more reductive in this interval of Hole 1001B. Evidence for this hypothesis consists of the presence of well-developed pale green halos around structural defects and pale green iron precipitates within foraminifer-rich sands in Hole 1001B that were not as obvious in Hole 1001A.

The NRM inclinations, and those measured after 20-mT AF demagnetization, are strongly biased toward high positive inclinations (50°–80°) above the unconformity at 166 mbsf and become gradually shallower from 166 to 200 mbsf, below which they predominately have values between −15° and +30°, particularly the 20-mT inclinations. Thus, like most of the results from the previous sites, the steep directions that occur above 166 mbsf indicate the presence of a strong drilling-induced magnetization. The results from farther downcore, however, show great promise for producing a reliable magnetostratigraphy and for constraining the paleolatitude of the Caribbean Plate through time. For example, the basalt inclinations show abrupt changes, which indicate that separate basalt flows have recorded independent time samples of the geomagnetic field, possibly even recording a reversal of the field (Fig. 23). The basalt and sediment inclinations are quite shallow (Figs. 23, 24), which indicates that the Caribbean Plate was at a low paleolatitude in Late Cretaceous and early Paleocene times. Even after 20- to 25-mT AF demagnetization, however, the sediment and basalt inclinations have a small bias toward positive values. This could be a Brunhes overprint or a drilling overprint. In either case, AF demagnetization in higher fields, or thermal demagnetization, will very likely remove the overprint.

In the upper Paleocene through upper Maastrichtian interval from 285 to 365 mbsf, the overprint is minor and an interpretable magnetostratigraphy is evident (Fig. 24; Table 5), although the interpretations are only preliminary given the gaps in core recovery and the incomplete demagnetization experiments. Even with these caveats, the boundaries for Chrons 26N through 30N are well defined (to within 50 cm), except the short Chron 28N, which was not identified probably because of the slow sedimentation rate in this part of the sedimen-

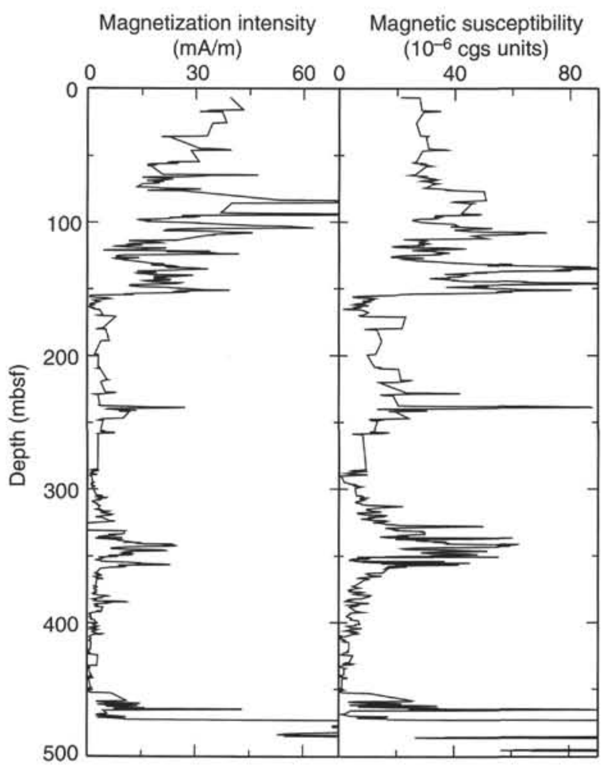

Figure 22. NRM intensity and magnetic susceptibility for Hole 1001A.

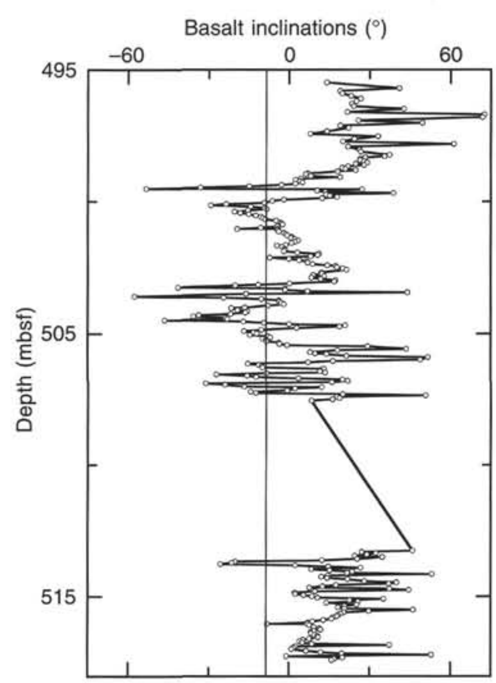

Figure 23. Basalt inclinations from Hole 1001A after 25-mT AF demagnetization.

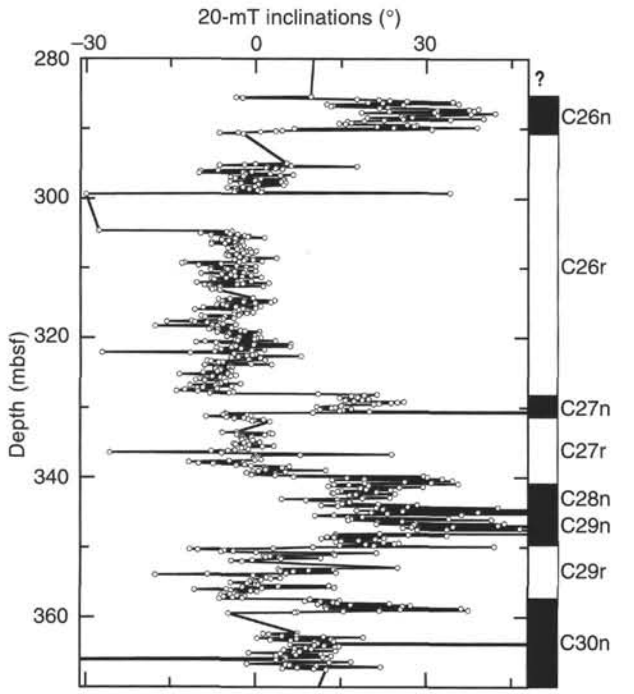

Figure 24. Inclinations and interpreted polarity chrons for the interval from 280 to 365 mbsf from Hole 1001A after 20-mT AF demagnetization.

tary succession. The results are only interpreted for Hole 1001A; correlation with Hole 1001B will be done post cruise, and will produce a more continuous record.

Paleomagnetic data for discrete samples are given in the Appendix tables on CD-ROM (back pocket, this volume).

SEDIMENTATION RATES AND MASS ACCUMULATION RATES

Sedimentation rates at Hole 1001A are illustrated in an age-depth plot (Fig. 25). These rates rely on the major planktonic foraminifer and calcareous nannofossil datums listed in Tables 3 and 4. Select nannofossil datums (the same as at Site 999) are used to estimate average sedimentation rates through time (Fig. 26). Differences in age-depth plots between nannofossils and foraminifers (Fig. 25) probably result in large part from the relatively coarse sampling densities used at this site for foraminifers (e.g., only core-catcher samples were studied).

To estimate the mean sedimentation rates and mass accumulation rates (MARs) more robustly (Table 6), we divided the record into five linear sections. Based on preliminary nannofossil data, mean sedimentation rates varied greatly from each of these intervals to the next. The mean rate decreased from 11 m/m.y. in the Late Cretaceous (76.0–65.0 Ma) to 4 m/m.y. in the early Paleocene (65.0–60.6 Ma) and then increased to 19 m/m.y. through the late Paleocene and early Eocene (60.6–52.0 Ma). The Paleogene and Neogene records are separated by a major unconformity that spans the interval from approximately 52.0 to 13.5 Ma. The mean sedimentation rate was only 7 m/m.y. from 13.5 to 9.6 Ma, an interval that spanned the time of the middle/late Miocene carbonate crash. Finally, in the latest Miocene to Holocene interval (9.6–0 Ma), the sedimentation rate averaged about 14 m/m.y. (Fig. 26). The general pattern of variation in sedimentation rates at Site 1001 matches that of Site 999 (Fig. 29, "Site 999" chapter, this volume). For example, both sites exhibit decreased rates in the early Paleocene and during the late Miocene carbonate crash.

Table 5. Depths of polarity chron boundaries in Hole 1001A.

Polarity chron	Age (Ma)	Depth (mbsf)
C24n (o)	53.347	200.0–208.4
C24r (o)	55.904	259.5
C25n (o)	56.391	267.0–273.7
C25r (o)	57.554	277.5–283.4
C26n (o)	57.911	290.4–293.4
C26r (o)	60.920	328.3–334.4
C27n (o)	61.276	331.3–335.9
C27r (o)	62.499	339.5–340.9
C29n (o)	64.745	350
C29r (o)	65.578	357.4

Note: (o) = onset.

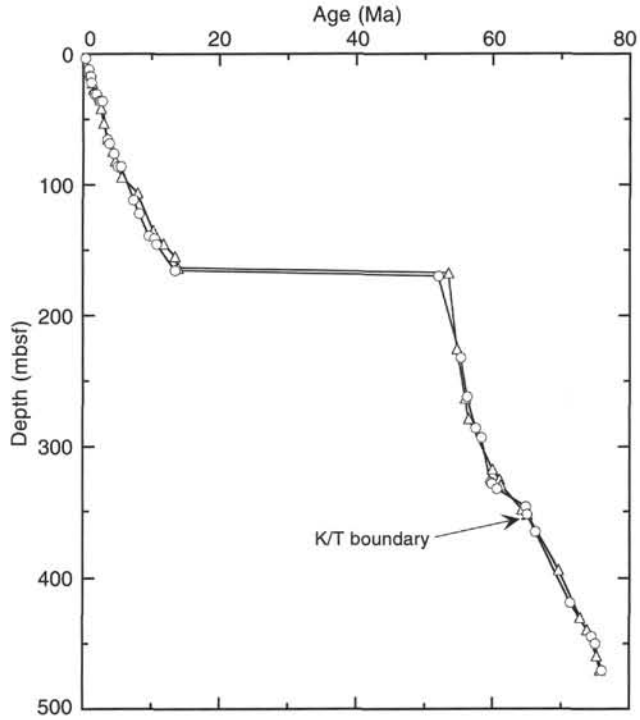

Figure 25. Age-depth plots for planktonic foraminifer (open triangles) and calcareous nannofossil (open circles) datums in Hole 1001A.

Bulk MARs for the Upper Cretaceous averaged 2.0–2.7 g/cm^2/k.y. (Table 6). Rates decreased markedly across the K/T boundary, averaging only 0.7–0.8 g/cm^2/k.y. in the early Paleocene; much of this is related to a marked decrease in carbonate MARs (Figs. 27–30). Bulk MARs rebounded in the late Paleocene and early Eocene, but were highly variable at 2.4–4.4 g/cm^2/k.y. The interval including the middle/late Miocene carbonate crash had low bulk MARs of 0.7–0.9 g/cm^2/k.y. A similar pattern of the noncarbonate MARs increasing at the expense of carbonate MARs has been observed at all the Leg 165 sites. Bulk MARs averaged 1.5–1.8 g/cm^2/k.y. for the upper Miocene and 1.3–1.5 g/cm^2/k.y. for the Pliocene–Pleistocene interval. The sparse data from the upper part of the section also suggest that the rates decreased in the Pleistocene, a pattern that has been observed at the earlier sites.

ORGANIC GEOCHEMISTRY

Introduction

Concentrations of inorganic carbon ($CaCO_3$) were measured coulometrically at a frequency of typically one sample per section (1.5

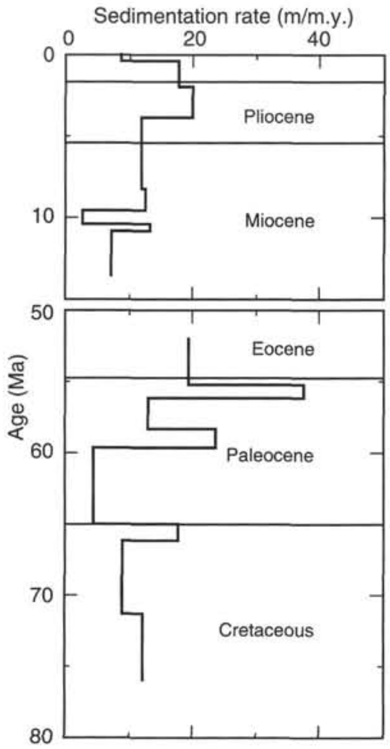

Figure 26. Sedimentation rates vs. age calculated from selected nannofossil datums in Hole 1001A.

m) for each core collected in Hole 1001A (Table 7). Because of poor core recovery over certain intervals and the presence of a number of critical intervals, the carbonate data for Hole 1001A are somewhat patchy. Carbonate determinations for Hole 1001B were not possible given the time constraints. Concentrations of total organic carbon (TOC) were determined for a representative suite of samples from Hole 1001A. In conjunction with the total carbon measurements, additional data were generated for concentrations of total nitrogen (N_T) and sulfur (S_T). Finally, headspace gases were monitored routinely in compliance with drilling safety requirements (one sample/core). Analytical details are provided in the "Organic Geochemistry" section of the "Explanatory Notes" chapter (this volume).

Concentrations of Inorganic and Organic Carbon, Total Nitrogen, and Total Sulfur

Concentration data for $CaCO_3$ carbon are discussed and graphically presented in the "Lithostratigraphy" section of this chapter. These data, along with results for TOC, N_T, and S_T, are provided in Table 7. Levels of TOC at Site 1001 are sufficiently low that the majority of the concentrations are near or below analytical resolution. The low concentrations of N_T are consistent with the extreme depletions in TOC. Because TOC was sparse, no effort was made to characterize the organic matter further using either Rock-Eval pyrolysis or C/N values.

The low levels of TOC dictate the diagenetic pathways that dominate the coupled organic-inorganic regime at Site 1001. Low rates of bacterial sulfate reduction are expected, given the comparative absence of TOC, and are indicated by the very gradual downcore decline in interstitial sulfate (see "Inorganic Geochemistry" section, this chapter). Low levels of bacterial production of hydrogen sulfide are indicated further by total sulfur concentrations of less than 0.2 wt% (Table 7). Given the expected scarcity of acid-volatile sulfide, intermediate sulfur species, organic-S, and solid-phase sulfates, total sulfur is assumed to be present entirely as FeS_2. Concentrations of pyrite-S show no systematic trend downcore and appear to be decoupled from the very low values for TOC. Although low, concentrations of S are slightly higher than expected given the extreme paucity of TOC; this may reflect externally derived hydrogen sulfide or perhaps sulfate reduction driven by the microbial oxidation of volatile hydrocarbons.

Volatile Hydrocarbons

As part of the shipboard safety and pollution monitoring program, hydrocarbon gases were measured continuously in the sediments of Hole 1001A (one analysis/core) using the headspace technique. Consistent with the very low levels of organic carbon, methane was found to occur at low concentrations in all the samples collected at Site 1001. Concentrations in the upper ~180 mbsf ranged from values below detection to 7 ppm. Additional hydrocarbon gases were not observed over this interval.

At approximately 220 mbsf, a subtle methane maximum was observed with a concentration of 43 ppm. In addition, C_2 through C_6 hydrocarbons were measured at trace levels. At greater depths, methane concentrations were low (~5–15 ppm) and C_{2+} hydrocarbons were generally absent. The slight methane enrichment at ~220 mbsf and the associated C_{2+} hydrocarbons occur immediately below a zone of low porosity (see "Physical Properties" section, this chapter). This porosity minimum, which is several tens of meters thick and has values as low as ~20%, corresponds with a major unconformity and a zone of chert enrichment (see "Lithostratigraphy" and "Biostratigraphy" sections, this chapter). As observed at Site 1000, the low-porosity zone may behave as a permeability seal capable of trapping small amounts of upwardly migrating thermogenic gases.

The gradual downcore decrease in sulfate concentration at Site 1001 indicates low rates of bacterial sulfate reduction as a consequence of the low availability of reactive organic phases. The low concentrations of headspace methane are expected given the likely persistence of sulfate over the entire lengths of both cores and the common observation that significant methanogenesis occurs only after sulfate is depleted (Martens and Berner, 1974).

INORGANIC GEOCHEMISTRY

Interstitial Water Chemistry

Introduction

A total of 13 interstitial water samples were collected at Site 1001 at depths from 1 to 370 mbsf (Table 8). Only eight samples were obtained from Hole 1001A at sporadic intervals because of the poor recovery caused by the rotary coring of unconsolidated sediments and the need to preserve critical stratigraphic intervals. Five samples were obtained from Hole 1001B to supplement the sporadic coverage of Hole 1001A. The smooth profiles exhibited by some elements using the combined sample sets attest to the good correspondence between the two holes. Analytical methods are detailed in the "Inorganic Geochemistry" section of the "Explanatory Notes" chapter (this volume). Samples were analyzed for pH, salinity, chlorinity, alkalinity, sulfate, phosphate, ammonium, silica, Na, Fe, Mn, Mg, Ca, K, Sr, Rb, and Li. Variable water yields prevented the full range of shipboard analyses being performed on all samples. Concentrations were not normalized to Cl concentration for reasons given in descriptions of the previous Leg 165 sites. Data for volcanic ash thickness, degree of alteration, mineralogy, and frequency (see "Igneous Petrology and Volcanology" section, this chapter) are used to evaluate the relationship between ash distributions and downcore geochemical trends in both pore waters and sediments. Reference seawater values are plotted as arrows on the axes of the various diagrams; these values are derived from mean ocean-bottom-water compositions (Millero and Sohn, 1992).

Table 6. Interpolated ages and mass accumulation rate data from Site 1001.

Core, section, interval (cm)	Depth (mbsf)	Age (Ma)	DBD (g/cm^3)	LSR (cm/k.y.)	Bulk MAR (g/cm^2/k.y.)	$CaCO_3$ (wt%)	$CaCO_3$ MAR (g/cm^2/k.y.)	Noncarbonate MAR (g/cm^2/k.y.)
165-1001A-								
3R-1, 29–31	16.39	1.14	0.98	1.44	1.41	58.06	0.82	0.59
4R-1, 29–31	25.99	1.80	0.96	1.44	1.38	61.73	0.85	0.53
5R-1, 29–31	35.59	2.47	1.00	1.44	1.44	63.22	0.91	0.53
6R-1, 29–31	45.19	3.14	0.98	1.44	1.41	55.89	0.79	0.62
7R-1, 29–31	54.89	3.81	0.97	1.44	1.40	63.31	0.89	0.51
7R-2, 29–31	56.39	3.92	0.97	1.44	1.39	66.72	0.93	0.46
7R-3, 29–31	57.89	4.02	0.97	1.44	1.39	57.14	0.79	0.60
8R-1, 29–31	64.49	4.48	1.01	1.44	1.46	62.72	0.92	0.54
8R-3, 29–31	67.49	4.69	0.94	1.44	1.35	59.48	0.81	0.55
8R-4, 29–31	68.99	4.79	0.96	1.44	1.39	60.31	0.84	0.55

Note: DBD = dry-bulk density, LSR = linear sedimentation rate, MAR = mass accumulation rate.

Only part of this table is produced here. The entire table appears on CD-ROM (back pocket).

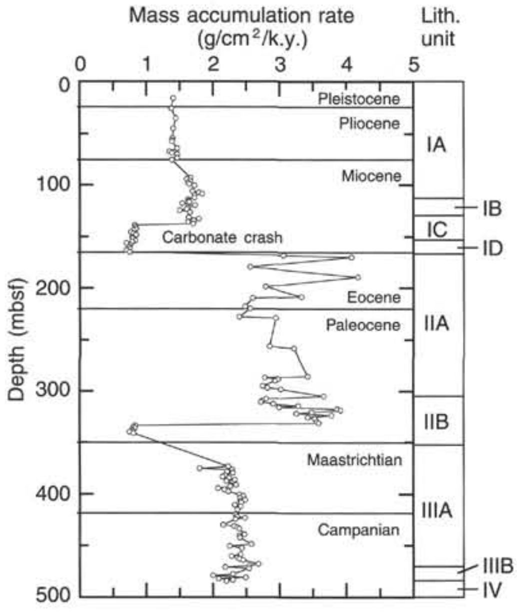

Figure 27. Bulk sediment mass accumulation rates vs. depth for Hole 1001A. Lithologic unit boundaries are shown on the right (see "Lithostratigraphy" section, this chapter).

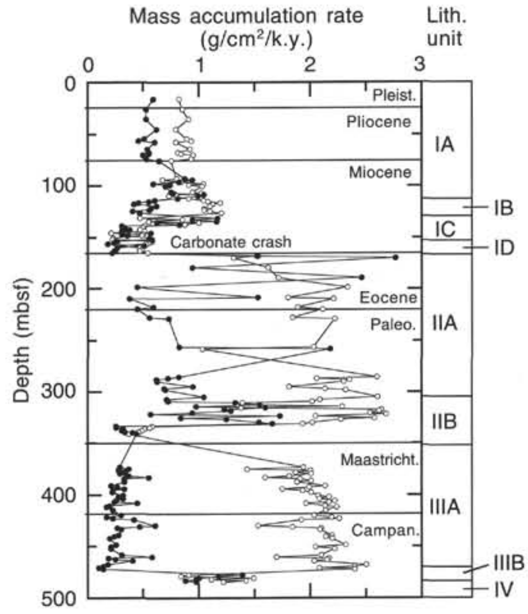

Figure 28. Mass accumulation rates for carbonate (open circles) and noncarbonate (solid circles) fractions vs. depth for Hole 1001A. Lithologic unit boundaries are shown on the right (see "Lithostratigraphy" section, this chapter).

pH, Salinity, Sodium, and Chlorinity

Values of pH range from 7.28 to 7.73. There is an overall trend of decreasing values down to the unconformity at 165 mbsf followed by a pronounced increase below this stratigraphic level and then a decline once more. Salinity levels are invariant from the shallowest sample gathered down to the unconformity (Fig. 31) and then increase dramatically from 35 to 39 g/kg over the next 200 m. This salinity increase cannot be accounted for by the sum of Na and Cl alone (Fig. 31) and is largely the result of greatly elevated levels of Ca below the unconformity (see below). The gradual 5% decline in Na concentrations may be a reflection of the progressive albitization of plagioclase as well as zeolite crystallization in the basaltic basement (see "Igneous Petrology and Volcanology" section).

Sulfate, Ammonium, Iron, and Manganese

Concentrations of dissolved sulfate at Site 1001 show a monotonic decrease downcore, with a 30%–40% decline in concentration relative to initial seawater values by ~350 mbsf (Fig. 32). This relationship reflects the very low rates of ambient dissimilatory sulfate reduction. Site 1001 is characterized by extreme deficiencies in organic carbon, with levels consistently below 0.1 wt% and often below the limits of analytical resolution (see "Organic Geochemistry" section, this chapter). In the absence of sufficient organic matter, which behaves as an electron donor, processes of dysaerobic to anaerobic respiration are minimal.

Consistent with the low rates of bacterial sulfate reduction, concentrations of ammonium are very low and show a high degree of downcore variability (Fig. 32). For example, in contrast to the strong organic signal at Site 1000 (e.g., recorded by ammonium concentrations approaching 3 mM), Site 1001 is characterized by a subsurface maximum of only 151 µM. The downcore scatter probably reflects the effects of silicate interaction; detrital clay minerals can form an ammonium sink through incorporation as either a trace cation or through exchange with K, and ammonium also is often released during the weathering of micas.

Despite the low levels of organic carbon, Mn concentrations in the upper ~150 mbsf are substantially higher than those that characterize

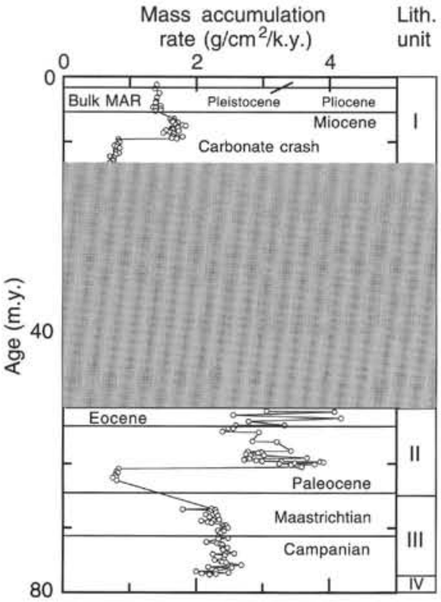

Figure 29. Bulk sediment mass accumulation rates (MARs) vs. age for Hole 1001A

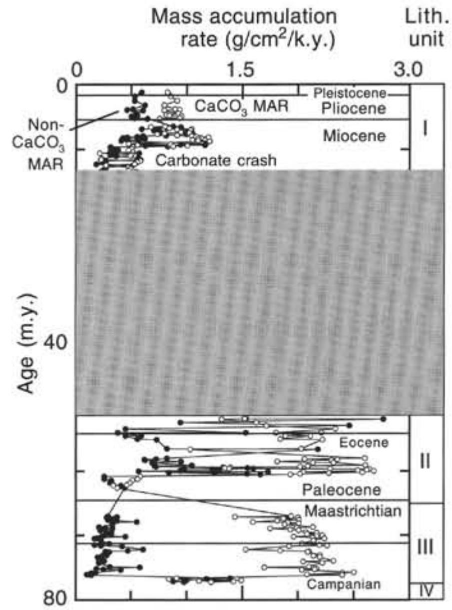

Figure 30. Mass accumulation rates (MARs) for carbonate (open circles) and noncarbonate (solid circles) fractions vs. age for Hole 1001A.

Table 7. Concentrations of inorganic carbon, calcium carbonate, total carbon, total organic carbon, total nitrogen, and total sulfur, Hole 1001A.

Core, section, interval (cm)	Depth (mbsf)	C_{inorg} (wt%)	$CaCO_3$ (wt%)	Total C (wt%)	TOC (wt%)	Total N (wt%)	Total S (wt%)
165-1001A-							
2R-1, 31–32	6.71	7.68	64.0				
3R-1, 31–32	16.41	6.97	58.1				
3R-2, 31–32	17.91	7.30	60.8				
4R-1, 31–32	26.01	7.41	61.7				
5R-1, 32–33	35.62	7.59	63.2				
6R-1, 27–28	45.17	6.71	55.9				
7R-1, 27–28	54.87	7.60	63.3				
7R-2, 27–28	56.37	8.01	66.7				
7R-3, 27–28	57.87	6.86	57.1	6.90	0.04	0.03	0.19
8R-1, 27–28	64.47	7.53	62.7				
8R-2, 28–29	65.98	8.12	67.6				
8R-3, 27–28	67.47	7.14	59.5				
8R-4, 28–29	68.98	7.24	60.3				
8R-5, 27–28	70.47	7.86	65.5				
9R-1, 27–28	74.07	7.66	63.8	7.58	0.00	0.02	0.15

Notes: Data are reported as weight percent (wt%). C_{inorg} = inorganic carbon, $CaCO_3$ = calcium carbonate, TOC = total organic carbon.

Only part of this table is produced here. The entire table appears on CD-ROM (back pocket).

Table 8. Interstitial water composition, Site 1001.

Core, section	Depth (mbsf)	pH	Alkalinity (mM)	Salinity (g/kg)	Cl^- (mM)	Na^+ (mM)	Mg^{2+} (mM)	Ca^{2+} (mM)	SO_4^{2-} (mM)	PO_4^{3-} (μM)	NH_4^+ (μM)	$Si(OH)_4$ (μM)	K (mM)	Fe (μM)	Mn (μM)	Sr (μM)	Rb (μM)
165-1001A-																	
6R-1	46.82	7.50	2.31	35	551	475	49.9	14.0	26.0	142	129	10.7	10.7	33.5	213	1.52	1.52
9R-1	75.30	7.28	2.44	35	548	467	49.1	15.7	24.6	90	133	11.4	11.4	37.0	243	1.47	1.47
12R-3	107.10	7.37	1.95	35	546	466	48.3	19.9	24.2	104	166	9.8	9.8	22.5	319	0.88	0.88
15R-3	136.00	7.44	1.95	35	546	458	47.4	24.0	23.9	151	278	8.8	8.8	54.5	357	1.00	1.00
18R-1	161.80	7.33	1.65	35	555	458	46.6	28.5	23.9	79	476	9.4	9.4	37.5	380	1.21	1.21
34R-3	309.10			38	577	419	26.4	91.7	20.6	96	445	6.5	6.5	6.5	593	0.16	0.16
36R-1	325.30			39	573	416	25.1	94.8	19.7	41	221	6.1	6.1	7.0	585	0.11	0.11
40R-3	365.35			39		399	22.3	107.3	18.9	35	140	4.9	4.9		608		
165-1001B-																	
1R-1	26.80	7.67	2.76	35	548	484	51.3	12.6	25.8	70	129	10.90	10.90	52.5	160	1.62	1.62
2R-3	154.80	7.41	1.55	35	548	478	46.2	26.2	23.0	80	302	8.56	8.56	43.0	365	0.88	0.88
3R-1	208.05	7.73	0.84	36	561	451	34.0	60.6	21.6	98	329	8.29	8.29	6.5	433	1.31	1.31
7R-5	252.40	7.40	0.93	37	559	437	30.4	75.4	20.4	73	307	7.11	7.11	4.0	509	0.67	0.67
12R-2	295.90	7.50	0.37	38	579	429	27.2	86.2	19.9	75	430	6.61	6.61	5.5	532	0.22	0.22

Notes: No data indicate where sample volumes were too small to provide for full analysis. This entire table also appears on CD-ROM (back pocket).

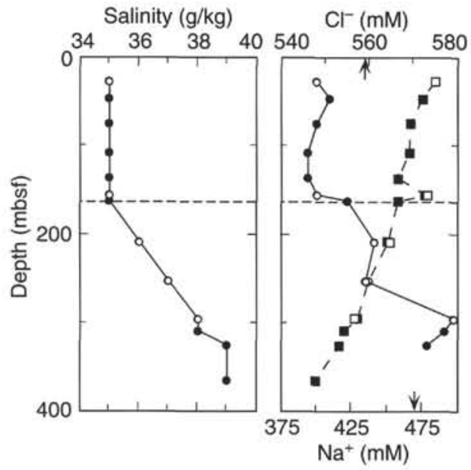

Figure 31. Depth profiles of salinity, Na^+, and Cl^- in Site 1001 interstitial waters. Solid symbols indicate data from Hole 1001A, open symbols from Hole 1001B. Arrows indicate mean ocean-bottom-water composition taken from Millero and Sohn (1992). Dashed line indicates the stratigraphic position of the erosional unconformity.

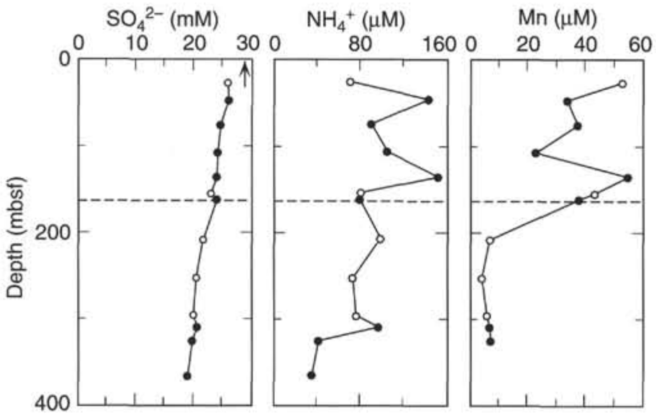

Figure 32. Sulfate, ammonium, and manganese concentrations in Site 1001 interstitial waters. Solid symbols indicate data from Hole 1001A, open symbols from Hole 1001B. Arrow indicates mean ocean-bottom-water sulfate composition taken from Millero and Sohn (1992). Dashed line indicates the stratigraphic position of the erosional unconformity.

the more organic-rich sediments of Site 1000. In part, this relationship reflects the lower overall $CaCO_3$ content and, consequently, the increased detrital source effect (see "Sediment Chemistry" section below). Furthermore, the sediments at Site 1001 are characterized by a lower availability of reactive $CaCO_3$ surfaces that are known to facilitate the adsorption of Mn, and there is no evidence for significant carbonate precipitation in the sediment column. In general, levels of dissolved Mn at Site 1001 are lowest where concentrations of $CaCO_3$ are consistently highest. The subsurface Mn maximum located at approximately 140 mbsf corresponds with the region of minimum $CaCO_3$ concentrations; again, this likely reflects an enhanced detrital source effect. In the absence of significant concentrations of organic carbon, the redox conditions of the pore water show a classic signal of deep-marine suboxic diagenetic reactions (Froelich et al., 1979).

Calcium, Magnesium, Alkalinity, and Strontium

Concentrations of Ca^{2+} and Mg^{2+} show an antithetic relationship, with a systematic decrease in Mg^{2+} that corresponds to a tenfold increase in dissolved Ca^{2+} (Fig. 33). The increase in Ca^{2+} is of sufficient magnitude to cause an ~10% increase in salinity. In fact, the increase

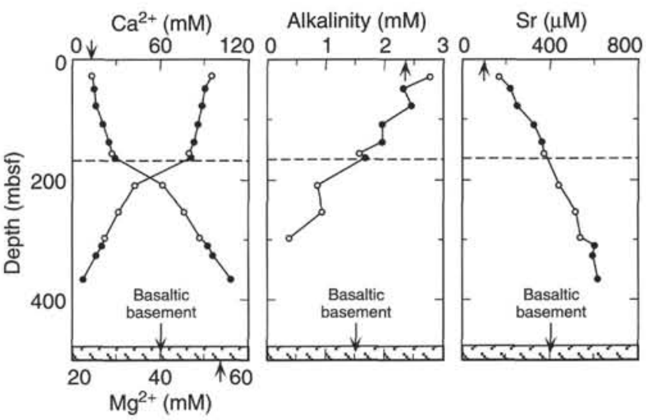

Figure 33. Depth profiles of Ca^{2+}, Mg^{2+}, alkalinity, and Sr in Site 1001 interstitial waters. Solid symbols indicate data from Hole 1001A, open symbols from Hole 1001B. Arrows indicate mean ocean-bottom-water composition taken from Millero and Sohn (1992). Horizontal dashed line indicates the stratigraphic position of the erosional unconformity.

in dissolved Ca^{2+} is up to a factor of 100 greater than those observed at Sites 998, 999, and 1000, where the Ca^{2+} profiles are dominated by alteration of intercalated and dispersed ash and detrital silicates in association with dissolution-reprecipitation reactions involving carbonate phases. Inflections in the profiles for Ca^{2+} and Mg^{2+} corresponding with the major unconformity observed at ~165 mbsf are noteworthy. Undoubtedly, these trends are a result of diffusion responding to the sharp porosity contrast observed across the erosional surface (see "Physical Properties" section, this chapter).

Unlike the previous three sites, which had subsurface concentrations of alkalinity in excess of seawater values, the results for Site 1001 show a systematic decrease and approach zero values by ~300 mbsf, despite the large associated increase in Ca^{2+} (Fig. 33). Because of the paucity of organic carbon, alkalinity does not show the surficial increase expected with oxidation of organic matter during anaerobic respiration. Concentrations of dissolved Sr display a roughly twofold increase over the interval that is characterized by increasing Ca^{2+}. The general relationships between alkalinity and Ca^{2+} argue for a Ca^{2+} source that is decoupled from the $CaCO_3$ and, when viewed in the context of all available data (e.g., K, Rb, and Na^+), suggest a strong signal from alteration of the proximal basaltic basement (see "Igneous Petrology and Volcanology" section, this chapter).

Fundamentally, the profiles for Ca^{2+}, Mg^{2+}, and alkalinity are controlled by a complex interplay of multiple competing and supporting reactions. For example, carbonate reactions and pathways of ash alteration are undoubtedly factors within the sediment column. Nevertheless, the large increase in Ca^{2+}, the concomitant decrease in alkalinity, and the broadly monotonic downcore gradients between overlying seawater and basement basalts with relative insensitivity to solid-phase variation within the sediment, are all consistent with a strong basement signal. The net reaction reflects (1) alteration of calcic plagioclase and mafic glass (Ca^{2+} release) within the basaltic basement and a corresponding precipitation of Mg-rich smectite (Mg^{2+} consumption), (2) formation of additional silicate phases (clays and zeolites as sinks for K, Rb, Na^+, etc.), and (3) precipitation of $CaCO_3$ (an alkalinity sink) recorded in the abundant calcite veins present throughout the altered basalt. Given the relative concentrations of Ca^{2+} and alkalinity, it is not surprising that the basement-associated precipitation of calcite is not apparent in the profile for Ca^{2+}. Ultimately, the relative role of basement alteration, as manifested in the pore-water profiles, will be constrained through additional, shore-based analyses. In particular, it is expected that downcore trends for the Sr-, S-, and O-isotopic composition of pore water will assist in deconvolving the relative contributions from seawater and less radiogenic basaltic sources.

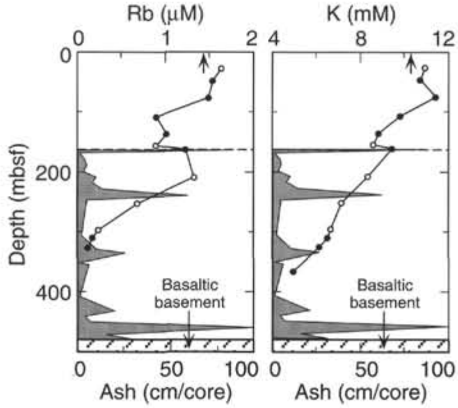

Figure 34. Depth profiles of Rb and K in Site 1001 interstitial waters. Solid circles indicate data from Hole 1001A, open circles from Hole 1001B. The thickness of megascopic ash layers in centimeters per core is also plotted. Arrows indicate mean ocean-bottom-water composition taken from Millero and Sohn (1992). Horizontal dashed line indicates the stratigraphic position of the erosional unconformity.

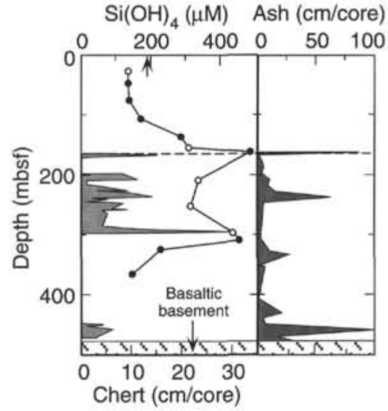

Figure 35. Depth profile of dissolved silica in Site 1001 interstitial waters. Solid symbols indicate data from Hole 1001A, open symbols from Hole 1001B. Thickness of chert layers per core indicated (gray area) in left-hand figure. The thickness of megascopic ash layers in centimeters per core is shown on the right (dark gray area). Horizontal dashed line indicates the stratigraphic position of the erosional unconformity.

Rubidium and Potassium

Both Rb and K concentrations in pore waters decline with increasing depth (Fig. 34). Potassium concentrations decrease from values close to seawater (11.5 mM) to <5 mM over 350 m, with a minor increase at the unconformity. Rubidium concentrations decline from 1.6 µM to negligible values (~0.1 µM) at 300 mbsf but show a secondary enrichment across the unconformity. The pronounced decrease in porosity across the unconformity undoubtedly contributes to the alkali metal (and other) inflections in pore-water chemical gradients at this level, but quantifying this effect is complicated by the presence of numerous possible sources and authigenic sinks for alkali metals at this interface (see "Lithostratigraphy" section, this chapter). Empirical observations are as follows: (1) excluding minor variations, the overall slopes of the trends are similar above and below the unconformity; (2) K and Rb concentrations increase at the unconformity, which coincides with the first appearance of silicic ash in the section, suggesting enhanced dissolution of alkalis related to ash weathering, and (3) Rb and K concentrations decrease smoothly below the unconformity, despite the presence of silicic ashes. This decrease in alkali concentrations in the lower part of the section, and the overall morphology of the profiles, could be attributed to the effects of a sink in the form of an alkali-metal-depleted basaltic basement that is weathering to form smectite and zeolite sinks. Minor variations related to ash alteration or mineral precipitation within the overlying sediment column may be superimposed upon these generally basement-dominated tends. For instance, the sharp decline of Rb concentrations (to essentially background concentrations) well above the basement implicates the possible effects of a mineralogical sink associated with reverse weathering reactions within the sediment column. The sharp decline in silica that is concordant with the Rb trend supports this hypothesis, but the nature of the sink is not readily apparent from XRD measurements.

Silica

The main feature of the dissolved silica pore-water profile at Site 1001 is a well-defined zone of elevated concentrations (>250 µM) between 130 and 320 mbsf that corresponds very closely to the distribution of chert in the sediment column (Fig. 35). Chert is not found above the unconformity. A possible source for the silica needed to form chert is from the abundant silicic ash layers observed in the lower part of the section. Discrete ash layers also terminate at the unconformity, suggesting erosion of a more extensive depositional sequence. At least two alternatives are available to explain these striking relationships. In both, a significant source of silica for the chert is likely to be altered silicic ash. Of critical importance, however, is the fact that the biogenic silica input cannot be well constrained by shipboard studies. One possibility is that chert formation was initiated well before the erosional event that created the unconformity and that chert distribution was more extensive than observed now. Although chert formation may be possible at the stratigraphic levels observed here (150 mbsf), pre-unconformity physical conditions (specifically, higher temperatures and greater burial depths) would have greatly favored diagenetic chert precipitation. The elevated dissolved silica levels associated with the chert-rich zone, in this scenario, would be a vestige of these earlier conditions. An alternative explanation is that chert precipitation occurred after erosion and burial of the unconformity and its distribution is controlled by physiochemical conditions imposed by the unconformity. In this situation, the abrupt cessation of chert precipitation above the unconformity would be attributed to the absence of a source, namely, silicic ashes (or, again, biogenic silica). Currently, we favor pre-unconformity chert formation. The monotonic decrease in K concentration across the unconformity suggests that despite greatly reduced porosity (65%–20%) it is not a particularly effective barrier to chemical exchange. Thus, in the post-unconformity chert alternative, we would expect to observe some chert above the unconformity, which is not the case.

Summary

Pore-water profiles for alkali metals, Sr, Ca^{2+}, and Mg^{2+} at Site 1001 appear to be strongly influenced by the effects of weathering reactions associated with a relatively shallow basaltic basement. Ca^{2+} and Sr are postulated to be released during the breakdown of labradoritic plagioclase. This results in very high (>100 mM) dissolved Ca^{2+} concentrations in the lower part of the drilled section. A concomitant decrease in pore-water Mg^{2+} largely reflects smectite formation during basalt alteration at depth. In contrast to previous sites on this leg, alkali metal profiles do not appear to be dominated by release during ash weathering. A zone of elevated dissolved silica between 150 and 320 mbsf is closely associated with the presence of chert, which terminates at the level of the erosional unconformity. We postulate that chert precipitation occurred before the erosional unconformity when burial depths and temperatures were greater. The dominant source of silica for the chert is probably the abundant silicic ashes encountered below the unconformity, although the biogenic silica input cannot be constrained presently.

Sediment Chemistry

Introduction

At Site 1001, the shipboard sediment chemistry program continued to sample sediment at a rate of one sample per every third core through the entire recovered sequence. We targeted analysis of the interstitial water squeeze-cakes, which served to speed up the acquisition time because we did not have to wait for the cores to reach the sampling table before starting the sample preparation procedure. In several instances, we took additional discrete 10-cm^3 samples from particular intervals that visually appeared representative and had no obvious marker beds (i.e., discrete ash layers, turbidites, or other unusual lithologies). The samples were analyzed as described in the "Explanatory Notes" chapter of this volume. A total of 20 samples were analyzed for major and trace elements. Sedimentary chemical data are presented in Tables 9 and 10.

Quantifying Sedimentary Components (Terrigenous Material and Dispersed Ash)

As at previous sites, the bulk sediment chemistry was used to quantify the absolute amounts of terrigenous material and other components distributed through the sediment column. Although it was relatively straightforward to quantify the amount of dispersed ash at the previous sites, we will show below that such determination at Site 1001 is more complicated.

We again quantified the terrigenous component by a normative calculation, based on the concentration of Cr in a given sample and comparing that to the concentration of Cr in average shale (Taylor and McLennan, 1985), according to:

$$(\%\text{Terrigenous})_{\text{sample}} = 100 \times (\text{Cr}_{\text{sample}}) / (\text{Cr})_{\text{avg shale}}.$$

We chose Cr as the reference element for many of the reasons outlined in the discussion of Site 999. As before, with the analytical detection limit of 3 ppm for Cr, the detection limit of the terrigenous calculation itself is slightly better than 3% (i.e., 3 ppm/110 ppm); this value also defines the amount of noise in the calculations. Given this calculation of the concentration of terrigenous material based on the Cr abundances, the remaining material—termed "residual"—was calculated by difference, according to:

$$(\%\text{Residual})_{\text{sample}} = 100 - \%\text{CaCO}_3 - \%\text{Terrigenous}.$$

Referring to the remaining material as "residual" is a nongenetic terminology.

Overall, the sedimentary sequence at Site 1001 can be divided into three contrasting chemical signatures, each with internal variation (Fig. 36). The first is located above the major Eocene/Miocene unconformity (see "Biostratigraphy" section, this chapter) and consists of bulk sediment containing ~60% $CaCO_3$ and 40% terrigenous matter, the latter of which appears similar in composition to average shale. The second is below the unconformity and consists of ~70%–80% $CaCO_3$, only ~5% terrigenous matter, and no more than 20% total of dispersed ash and other components (e.g., chert). The third is located from 400 mbsf to the bottom of the sequence and consists essentially entirely of $CaCO_3$ and dispersed ash.

In detail, throughout the uppermost 110 mbsf, the bulk sediment can be successfully modeled completely as a two-component system (carbonate and terrigenous matter). This depth range corresponds well with lithologic Subunit IA (see "Lithostratigraphy" section, this chapter). From 110 mbsf to the Eocene/Miocene unconformity at ~165 mbsf, the carbonate concentration increases, whereas that of the terrigenous matter decreases and a third component (strictly termed "residual" at this point of the discussion) begins to become quantitatively significant (Fig. 36). The shipboard sampling program was not of a sufficiently high resolution to discern the middle to late Miocene carbonate minimum (see "Lithostratigraphy" section, this chapter).

Table 9. Major element chemistry of bulk sediment, Hole 1001A.

Core, section, interval (cm)	Depth (mbsf)	Ca (ppm)	Fe (ppm)	Mn (ppm)	P (ppm)	Ti (ppm)
165-1001A-						
2R-1, 42–44	6.82	320634	27534	2872	469	2409
3R-1, 110–112	17.20	325811	25833	2561	435	2201
6R-1, 145–150	46.35	306972	28745	1775	358	2503
9R-1, 145–150	75.25	296436	28846	2064	351	2342
11R-4, 98–100	98.48	294093	27385	1435	335	2292
12R-3, 145–150	107.05	290177	36502	2085	552	2473
15R-3, 145–150	135.95	283461	37329	2368	694	2684
17R-4, 98–100	156.18	332531	14627	2528	273	1030
18R-1, 145–150	161.75	342406	13525	2516	225	992
18R-4, 98–100	165.78	375826	5181	1180	266	320
21R-1, 84–86	180.44	306741	9082	387	486	822
24R-1, 86–88	209.26	371701	5612	559	365	508
28R-1, 58–60	247.48	338175	6159	433	237	463
34R-3, 145–150	309.05	313558	8819	555	353	690
36R-1, 145–150	325.25	322836	10547	895	562	837
36R-4, 43–45	328.73	337739	6626	932	417	578
40R-3, 0–5	365.30	349719	9244	638	287	753
43R-4, 109–111	396.79	364312	3669	482	152	322
46R-2, 47–49	421.97	374047	1921	277	97	205
51R-3, 93–95	471.61	365950	2917	742	77	192

Notes: Data overspecified for calculation purposes. This entire table also appears on CD-ROM (back pocket).

Below the unconformity, the composition of the sediment changes dramatically. Calcium carbonate concentrations increase to ~70%–80% and, most importantly, the concentration of the terrigenous component decreases sharply to less than 10% (Fig. 36). In harmony with this decrease in terrigenous matter is an increase in the residual component, up to maximum values of ~20% of the bulk sediment. At previous sites, based on independent chemical partitioning and in part on strong correlations with the distribution of discrete ash layers (see previous chapters, this volume), we were able to attribute the majority of this residual component to dispersed ash in the bulk sediment. However, because the terrigenous component is so low in concentration from 165 to 390 mbsf, there is increased uncertainty in the concomitant assessment of the residual fraction. In addition, the stratigraphic distribution of the residual component at Site 1001 does not correlate obviously with the distribution of the discrete ash layers (Fig. 36; see "Igneous Petrology and Volcanology" section, this chapter). Therefore, the interpretation of the residual component is somewhat complicated, and this component may very well include fractions other than dispersed ash. For example, chert has been documented to be present from 150 to 300 mbsf (and a small quantity again from 450 to 500 mbsf; see "Lithostratigraphy" section, this chapter), and thus will contribute to the residual component. Note, however, that the stratigraphic sequence is completely barren of chert from 300 to 450 mbsf (see "Lithostratigraphy" section, this chapter), and this interval indeed still contains relatively high abundances of the residual fraction. The sedimentologic descriptions of the sequence throughout these intervals do not provide additional information on potential contributors to the residual fraction, and we therefore tentatively conclude that the dispersed ash component in fact comprises the majority of the residual component in the sediment deeper than 300 mbsf. From 150 to 300 mbsf, however, precise quantification of the amount of dispersed ash will await additional shore-based studies. Contrasts between the occurrence of the discrete layers and the dispersed ash component may yield important insights into the depositional history of Site 1001 as well as the nature of eolian vs. fluvial input of the ash.

Finally, the third bulk lithology at Site 1001 is located below 400 mbsf and it consists of ~90% calcium carbonate, 0% terrigenous matter, and ~10% dispersed ash. This is the portion of the sequence in which the discrete ash layers become more prevalent (see "Igneous

Table 10. Trace element chemistry of bulk sediment, Hole 1001A.

Core, section, interval (cm)	Depth (mbsf)	Nb (ppm)	Zr (ppm)	Y (ppm)	Sr (ppm)	Rb (ppm)	Zn (ppm)	Cu (ppm)	Ni (ppm)	Cr (ppm)	V (ppm)	Ba (ppm)
2R-1, 42–44	6.82	4.1	58	10	915	36	98	36	52	44	82	302
3R-1, 110–112	17.20	4.5	55	7	932	34	74	33	44	41	63	229
6R-1, 145–150	46.35	4.7	62	10	977	38	74	36	54	55	85	214
9R-1, 145–150	75.25	5.9	71	9	940	50	74	42	50	45	83	198
11R-4, 98–100	98.48	5.5	68	11	938	56	93	58	49	51	116	239
12R-3, 145–150	107.05	5.5	71	12	884	51	84	39	62	56	89	218
15R-3, 145–150	135.95	6.5	90	22	980	40	95	147	79	51	79	545
17R-4, 98–100	156.18	1.9	45	9	1198	27	53	26	32	19	29	222
18R-1, 145–150	161.75	BDL	45	7	1298	20	46	24	30	14	23	301
18R-4, 98–100	165.78	BDL	21	8	719	7	50	30	20	4	8	1221
21R-1, 84–86	180.44	BDL	33	7	478	11	21	28	15	8	16	1389
24R-1, 86–88	209.26	BDL	18	4	598	5	29	24	11	4	6	1118
28R-1, 58–60	247.48	BDL	22	4	628	7	23	22	13	6	10	1003
34R-3, 145–150	309.05	BDL	21	5	437	8	34	36	24	8	16	1813
36R-1, 145–150	325.25	BDL	25	9	445	10	45	46	26	12	22	2455
36R-4, 43–45	328.73	0.5	18	6	398	8	33	25	19	8	11	1658
40R-3, 0–5	365.30	BDL	25	20	604	9	36	42	24	9	15	3617
43R-4, 109–111	396.79	BDL	15	11	460	5	24	36	18	3	6	1776
46R-2, 47–49	421.97	BDL	11	9	383	5	26	30	9	<3	<4	953
51R-3, 93–95	471.61	1.1	21	6	335	3	24	18	9	<3	<4	249

Notes: BDL = below detection limits. Data overspecified for calculation purposes. This entire table also appears on CD-ROM (back pocket).

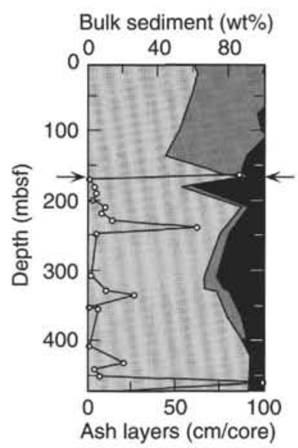

Figure 36. Depth profiles of carbonate concentration (light gray area), terrigenous matter (dark gray area), and the "residual" component (black), all in units of weight percent of the bulk sediment. Also plotted is the frequency of discrete ash layers (open circles, in units of centimeters per core). Horizontal dashed line at 165 mbsf indicates the Eocene/Miocene unconformity.

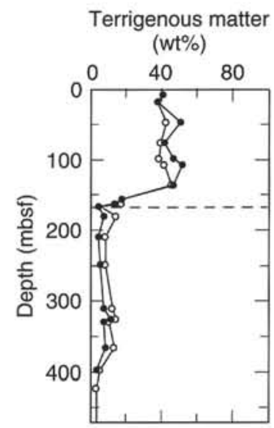

Figure 37. Depth profiles of the amount of terrigenous matter in the bulk sediment, as determined using both Cr- (solid circles) and Ti-based (open circles) normative calculations. The dashed horizontal line at 165 mbsf indicates the Eocene/Miocene unconformity.

Petrology and Volcanology" section, this chapter) and also where there is little or no chert, so our attribution of the residual fraction to dispersed ash is robust.

Terrigenous Provenance

The other main thrust of the shipboard sediment chemistry program at Site 1001 addressed determination of changes in detrital terrigenous provenance. Such changes were assessed by two separate methods.

First, substituting Ti in the above equation for calculation of the terrigenous component allows us also to test the suitability of using average shale compositions of Cr to quantify the terrigenous component. Such substitution (Fig. 37) indicates (1) that Cr- and Ti-based calculations yield closely similar estimates of the absolute terrigenous abundance and identical determinations of the pattern of terrigenous deposition through time; and (2) that there is nonetheless a slight fractionation of Ti and Cr within the sequence. In particular, note that through the upper 165 mbsf the Cr-based calculation yields slightly greater values than the Ti-based calculation, whereas below the unconformity the Cr-based values are slightly less than the Ti-based values (Fig. 37). Although some of this contrast above and below the unconformity may reflect the increased significance of dispersed ash (with its relatively high Ti concentration; see "Igneous Petrology and Volcanology" section, this chapter), it is also consistent with a subtle but quantifiable change in terrigenous provenance from the Paleocene–Eocene to the Miocene–Pleistocene.

The second method of assessing provenance changes involves determining chemical variability in the noncarbonate (100 – %$CaCO_3$) fraction. In addition to contributing toward an understanding of provenance changes, such study will constrain the amount of dispersed ash in the sediment. For example, comparing the concentration of Zr vs. the proportion of noncarbonate material in the sample set indicates that there are two distinct trends within the data set (Fig. 38). One group trends toward high values typical of average shale whereas the other trends toward lower values typical of ash (or perhaps a range of ash, "shales," or mixtures of both). Such patterns can also be seen for Ti, Zn, and Rb (Fig. 38). Additional post-cruise study of these data groupings, as well as of additional elements, will further constrain the chemical variability throughout the sequence, and further identify other potential sources, such as basaltic material near the basement. At this point, we have clearly identified that there are three (or more) contributing components, including one or more "shale" components, a dispersed ash component, and the biogenic calcium carbonate.

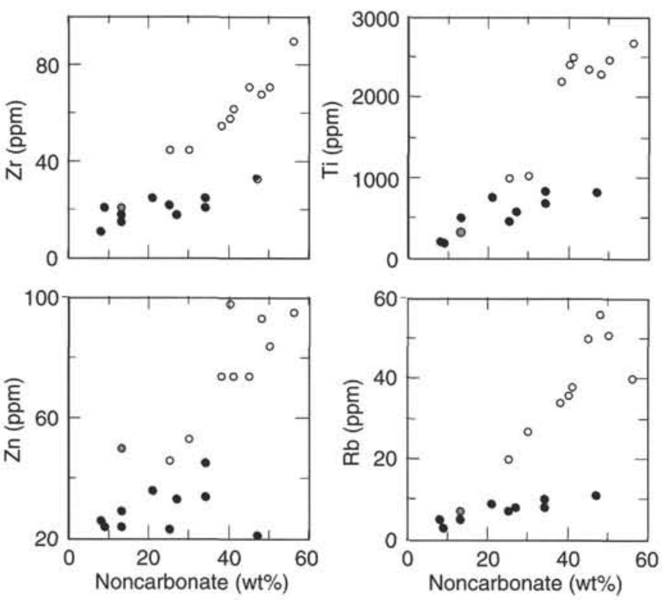

Figure 38. Plots of elemental variability with respect to the noncarbonate (100 – %$CaCO_3$) fraction. Shown here are data trends for Zr, Ti, Zn, and Rb. Open circles are for data from the uppermost cores (Samples 165-1001A-2R-1, 42–44 cm, through 18R-1, 145–150 cm), and black circles are for lowermost cores (Sample 165-1001A-21R-1, 84–86 cm, to the deepest sample). The light gray circle represents the single sample (165-1001A-18R-4, 98–100 cm) that is located in the small wedge of limestone between the two unconformities (see "Biostratigraphy" section, this chapter).

IGNEOUS PETROLOGY AND VOLCANOLOGY

Drilling at Site 1001 yielded several important results for igneous petrology and volcanology studies. The volcanic ash layers recovered at this site extended the record of explosive volcanism further back in age than at any other site cored on Leg 165, revealing a Campanian explosive volcanic episode with a unique geochemical signature. Furthermore, the recovery of over 20 m of basaltic basement rocks and the recovery of the lava/sediment contact in two holes is a major contribution to the study of the Caribbean Oceanic Plateau. These conformable contacts provide new biostratigraphic dating of the timing of basaltic volcanism in the late stages of the evolution of this large igneous province. A perplexing feature is the occurrence of basaltic volcaniclastic turbidites in the Campanian limestones a few meters above the basaltic basement. These, together with the relatively vesicular nature of the basalts, may indicate that relatively shallow-water volcanic edifices existed on the oceanic plateau in the Late Cretaceous.

Volcanic Ash Layers

Drilling at Site 1001 recovered numerous volcanic ash layers, ranging in age from 52 to 77 Ma. As the ash succession at this site was cored twice, a comparison between Hole 1001A and adjacent Hole 1001B gives a good indication of the variability in the observed volcanic ash record, which can be attributed to variable core recovery. The distribution of volcanic ash layers at Site 1001 is given in the Appendix tables on CD-ROM (back pocket, this volume). The total ash layer thickness in Holes 1001A and 1001B is 426 and 451 cm, respectively, and the average layer thickness is 4 and 4.6 cm, whereas the total number of layers is 109 for Hole 1001A and 98 for Hole 1001B. The difference between the two holes is dominantly in the Campanian, where several thick ash layers and ash turbidites were better recovered in Hole 1001B. The occurrence of ash layers indicates three principal explosive volcanic episodes (Fig. 39). There is a pronounced episode in the period from 53 to 55 Ma (late Paleocene to early Eocene), with accumulation rates of ash layers up to 100 cm/m.y. This episode may correspond to the early Eocene volcanism observed on the Cayman Rise at Site 998, where we recovered the final stages of the episode. These late Paleocene–early Eocene tephra layers are silicic and typically contain plagioclase phenocrysts, with rare biotite.

Another volcanic episode occurs in the earliest Paleocene sediments, immediately above the K/T boundary (62–65 Ma), with a peak accumulation rate of 20 cm/m.y. The same episode was observed at Site 999 on the Kogi Rise in the Colombian Basin, with accumulation rates up to 50 cm/m.y. The lower Paleocene ash consists of altered silicic glass shards, with abundant plagioclase phenocrysts and very common large hornblende crystals.

The volcanic record throughout the Maastrichtian is very subdued at Site 1001, with almost no ash layers recorded in the sediments. A third episode occurs, however, in the Campanian, beginning immediately above the basaltic lava basement succession at around 78 Ma, and terminating in the mid-Campanian at about 74 Ma. The accumulation rate of ash layers during this episode is up to 150 cm/m.y. The Campanian tephra layers are dominantly silicic in composition, but generally highly altered, with the replacement of glass shards by smectite and chlorite. Some of the turbidite-like layers may be mafic in composition. Plagioclase is the principal phenocryst phase that is present or has survived alteration, together with rare quartz, a trace of amphibole and biotite in some layers, and minor opaque minerals.

A distinctive facies of Campanian volcanic ash layers was recovered in cores from Hole 1001B. For example, in Section 165-1001B-31R-5 there are five medium-bedded volcanic ash layers that have sharp, slightly erosive bases with bioturbated tops. The thickest layer, between 65 and 95 cm, contains at least 15 distinct fining-upward intervals, each with a sharp base, defined by an abrupt change in grain size. The other layers in the section contain either minor cross-laminations or convolute laminations. These sedimentary features indicate deposition of tephra by sediment gravity flow and not by ash fallout. A thin section from the base of a flow deposit in Core 165-1001B-31R shows that the sediment is highly altered with no trace of fresh glass. However, several important components can still be identified based on remnant structures and color. A common component of the layer is poorly vesicular blocky shards with relatively large spherical vesicles and curvilinear boundaries. The morphology of these shards is typical of mafic hyaloclastites (Fisher and Schmincke, 1984). Dark ash layers of Campanian age were also reported at DSDP Site 152 in sediments closely overlying the volcanic basement (Edgar, Saunders, et al., 1973). Another conspicuous, but less common component in Hole 1001B is red oxidized vesicular clasts up to 1 mm in diameter. In addition, there are abundant subrounded clasts of microcrystalline basalt. Finally, the volcaniclastic material in this layer is mixed with rare to common tests of foraminifers. The lithology and grain size of these layers greatly resemble a thick sequence of volcaniclastic turbidites recently drilled at Site 953, approximately 70 km north of the island of Gran Canaria in the Atlantic Ocean (Shipboard Scientific Party, 1995). Near the base of Site 953, a sequence of thin- to medium-bedded volcaniclastic turbidites interbedded with deep-water carbonate was identified overlying thick-bedded, poorly vesicular, basaltic hyaloclastite debris-flow deposits. The thin-bedded turbidites were interpreted to represent material derived from the shallow-water stage of volcanism associated with the evolution of Gran Canaria, based on the presence of red oxidized lithics, the fine-grained and vesicular nature of the hyaloclastites, and the presence of partially rounded basalt fragments and foraminifers.

The source and tectonic setting of the volcanism that produced the Campanian ash layers recovered at Site 1001 is an interesting problem, as this volcanic episode reaches its climax only 2–3 m.y. after the emplacement of the youngest basalts of the Caribbean Oceanic Plateau. Volcanism was widespread in the Greater Antilles arc sys-

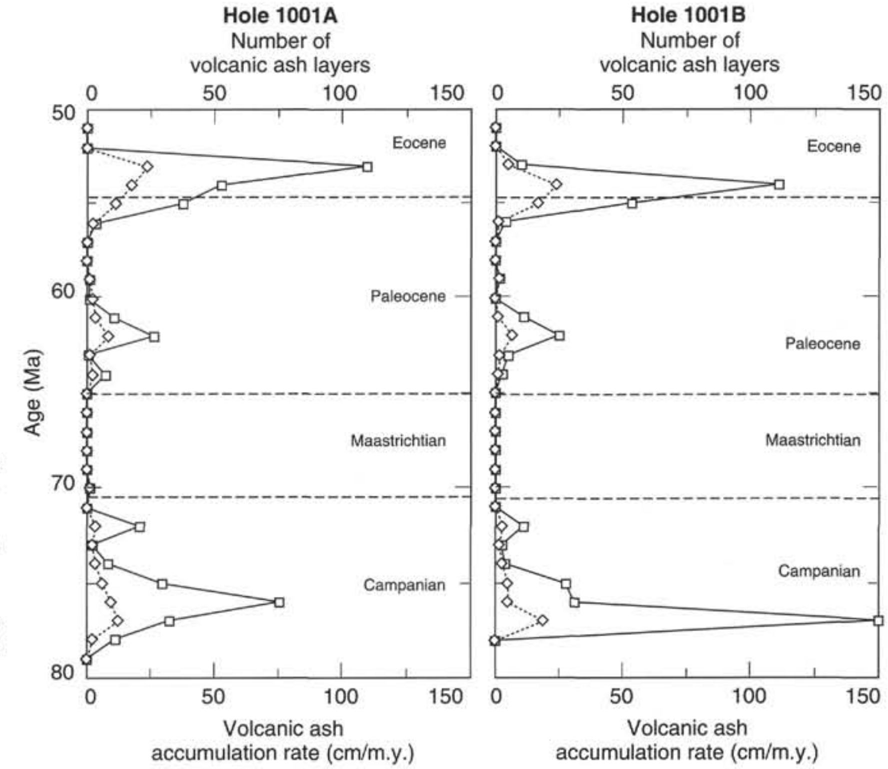

Figure 39. Distribution of volcanic ash layers observed in sediments from Holes 1001A and 1001B. Open diamonds show the number of ash layers per million years; open squares show the ash accumulation rate (cm/m.y.) The record in the two holes is very similar, except for the higher thickness of ash in the Campanian episode in Hole 1001B, because of the good recovery in this hole of relatively thick ash layers and ash turbidites. Three principal episodes are documented: a latest Paleocene to early Eocene silicic ash episode, which may correspond to the volcanic ash succession observed on the Cayman Rise (Site 998), a Paleocene episode also observed at Site 999 on the Kogi Rise, and a Campanian episode that is unique to this site.

Table 11. Major and trace element composition of volcanic ash layers from Site 1001.

Core, section, interval (cm)	Depth (mbsf)	Major oxide (wt%)											
		SiO_2	TiO_2	Al_2O_3	Fe_2O_3	MnO	MgO	CaO	Na_2O	K_2O	P_2O_5	Total	LOI
165-1001A-													
24R-1, 14–16	208.54	62.8	0.71	16.5	7.37	0.01	6.75	3.17	2.08	1.12	0.02	100.5	10.86
50R-3, 103–106	462.43	63.1	0.52	18.1	6.82	0.03	6.77	3.20	1.80	0.83	0.07	101.2	13.73
50R-5, 78–81	465.18	58.8	1.25	15.9	9.66	0.05	6.91	4.19	1.82	1.08	0.39	100.0	11.22
165-1001B-													
31R-3, 37–39	474.03	53.8	1.12	13.8	13.40	0.11	8.40	6.34	2.15	1.19	0.11	100.4	15.28

Core, section, interval (cm)	Depth (mbsf)	Trace element (ppm)									
		Nb	Zr	Y	Sr	Rb	Zn	Cu	Ni	Cr	V	Ba
165-1001A-												
50R-3, 103–106	462.53	34.1	498	46	315	7	75	20	26	5	29	65
50R-5, 78–81	465.18	25.6	366	66	332	12	105	31	62	3	90	67
165-1001B-												
31R-5, 37–39	474.03	4.0	83	15	293	13	142	132	74	52	266	91

Notes: Shipboard XRF data. LOI = loss on ignition. This entire table also appears on CD-ROM (back pocket).

tem in the Late Cretaceous (Lewis and Draper, 1990), and this region must be considered as a potential source, together with the Central American arc and the magmatism on the Nicaraguan Rise. On nearby Jamaica, a Late Cretaceous magmatic arc produced a variety of volcanic rocks, including ignimbrites (Draper, 1986). Products of silicic explosive volcanism of Campanian age have also been found in the Cordillera Central of Hispaniola and the Massif du Nord in Haiti.

Alternatively, the source of the Campanian volcanic ash layers could be the earliest stages of the Central American arc to the west. This would be more consistent with present-day atmospheric dispersal paths of tephra, although the site may still have been significantly to the south of such sources. On the other hand, the presence of distinctive hyaloclastite turbidites raises the possibility that the influx of volcaniclastic sediment shortly after the emplacement of the basement rocks was derived from relatively proximal sources on the basaltic plateau. The association of mafic hyaloclastite turbidites and silicic tephra falls is compatible with a volcaniclastic facies adjacent to hot-spot oceanic islands. For example, marine sedimentary basins adjacent to Iceland, the Canary Islands, and the Galápagos Islands currently receive influxes of silicic tephra by fallout from Plinian style eruptions and deposition of abundant mafic volcaniclastics by sediment gravity flows (e.g., Schmincke and von Rad, 1979; Sigurdsson and Loebner, 1981). Thus, the Campanian volcanic ash record may represent the waning stages of oceanic island volcanism, contributing volcaniclastic material to a subsiding oceanic plateau.

Geochemistry of Volcanic Ash Layers

The major oxide and trace element composition of four Campanian volcanic ash layers (taken from Sections 165-1001A-50R-3 and 50R-5) is shown in Table 11. Two of these 35- and 18-cm-thick layers, which occur about 10 m above the basement contact, contain bedded units and laminations, and thus may be ash turbidites (Fig. 40). They range in major oxide composition from basaltic andesite to

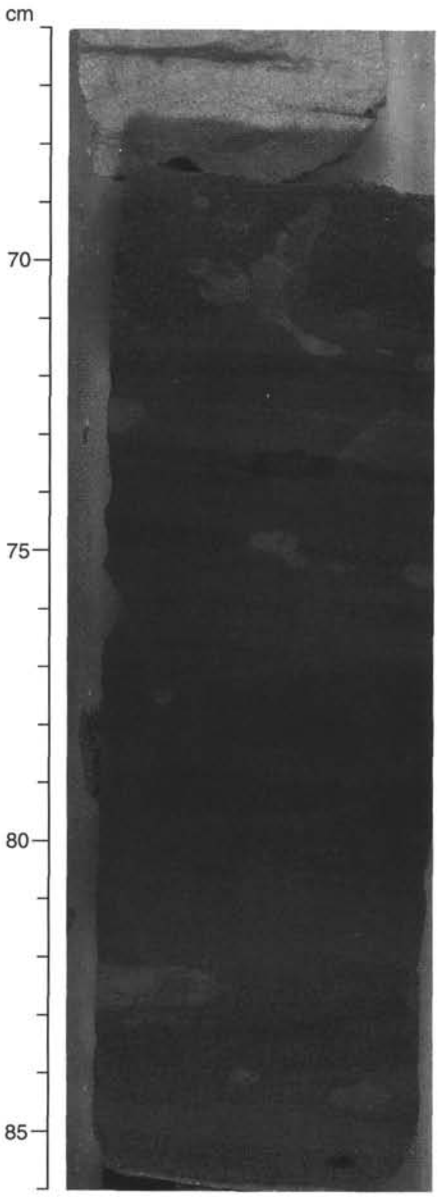

Figure 40. An 18-cm-thick volcanic ash layer of Campanian age (interval 165-1001A-50R-5, 66–86 cm) with well-defined laminations, indicative of a turbidite origin. The chemical composition of this and related ash layers is highly distinctive and dissimilar from silicic ashes recovered on Leg 165 (Table 11).

dacite. In terms of trace element composition, they are strikingly different from other ash layers recovered on Leg 165, with higher concentrations of Nb, Zr, Y, Zn, and Cu, but lower values of Sr, Rb, and Ba. The latter may be due in part to leaching of alkalis during alteration of the volcanic glass, but the differences are sufficiently large to be distinctive of this volcanic episode. Their trace element composition is also markedly different from that of the underlying basalts (Table 12).

Igneous Basement

Basaltic rocks of dominantly extrusive origin were encountered at a depth of 485.4 mbsf in Hole 1001A (Section 165-1001A-52R-6), and 486.2 mbsf in Hole 1001B (Section 165-1001B-32R-6). Of the 37.65 m of basement drilled in Hole 1001A, some 20.5 m of core were recovered, or 54.5%. This compares favorably with the total of about 25 m of igneous basement rocks recovered from five Caribbean sites during drilling during DSDP Leg 15.

The basalts are overlain by Campanian limestones and clayey limestones, with nannofossils of the CC21 biozone, indicating a minimum age of 77 Ma (see "Biostratigraphy" section, this chapter). Thin lenses of carbonate sediment between the basalt flow units also contain a Campanian microfossil assemblage. The sediment/basalt contact, which was recovered perfectly intact in both holes, consists of a dark greenish black, glassy basaltic breccia with a light greenish gray limestone matrix (Fig. 19). Angular 1- to 2-cm-thick clasts of dense basaltic glass (now altered to smectite) contain a variolitic to microcrystalline vesicle-free interior.

The basaltic sequence in Hole 1001A is divided into 12 formations, which likely represent individual lava flows and associated hyaloclastite breccias. In some cases, the contacts between units appear to be intrusive, with a chilled and glassy rind, but in view of the high vesicularity of these units and their petrographic similarity, we interpret such relations as indications of the injection of lava lobes into the interior of expanding and growing lava flows. The basaltic succession and the distribution of principal rock types are shown in Figure 41. The youngest is Formation A, which has a total thickness of 596 cm and consists of a massive basaltic lava flow, grading upward into a hyaloclastite breccia.

The upper bed (A1; lithologic Units 1, 2, and 3; Sections 165-1001A-52R-6 to 52R-8) is a 176-cm-thick, glassy, aphyric basaltic breccia and lapilli. In the upper part of this bed, the glassy and angular basaltic clasts appear to be supported in the limestone sediment, but they grade down into breccia and lapilli that is dominantly supported in a glassy basaltic lapilli matrix. Individual glassy clasts have a very dark greenish black rim, with a light gray interior, where the glass is altered to clay. Some larger clasts or basaltic veins have a dark brown microcrystalline basaltic interior, grading outward through a variolitic zone, to a dark greenish black glassy margin. Some of the basaltic veins from the underlying massive basalt have penetrated into the breccia, and their chilled margins have spalled off angular glassy lapilli clasts (Fig. 42). Thus, the breccia and lapilli clasts have been generated in situ by fragmentation of the quenched rinds of the basaltic lava (Fig. 43). Abundant angular voids between the concave and angular breccia and lapilli clasts, up to 1 cm in size, are lined or filled with white calcite (Fig. 44).

Bed A2 is 4.2 m thick and comprises the lower part of Formation A (lithologic Unit 4 in Sections 165-1001A-52R-8 to 53R-4). This massive and aphyric basalt is microcrystalline and vesicular in the upper part, but grades downward to a poorly vesicular and medium-grained lower part. Numerous subvertical joints in the basalt lava are filled with calcite.

Formation B is a sparsely plagioclase-phyric basalt that is 2.2 m thick (Units 5–11 in Sections 1001A-53R-4 to 54R-1). The upper contact is a well-preserved glassy rim, underlain by a vesicle-rich zone. The entire core recovery from this formation consists of alternating pieces of basalt with glassy chilled margins, glass-bearing breccia, and lapilli. Individual pieces are generally less than 40 cm in length and typically have glassy rinds on both upper and lower contacts. We interpret this formation as a pillow lava, with associated breccia zones and glassy lapilli generated by the spalling off of expanding and growing pillows.

Formation C is also a sparsely plagioclase-phyric pillow lava and basalt breccia (Units 12–17 in Sections 165-1001A-54R-1 to 54R-3). The central region of this formation has a relatively massive (80 cm), sparsely plagioclase-phyric unit (Section 165-1001A-54R-2), which is likely to represent the flow interior, overlain and underlain by pillow lava fragments and breccia with voids filled by white calcite. Subvertical calcite veins are also common infilling in subvertical joints in the massive basalt. Subhedral plagioclase phenocrysts up to

Table 12. Major oxide chemical composition of basalts from Site 1001.

Core, section, interval (cm)	Depth (mbsf)	SiO_2	TiO_2	Al_2O_3	Fe_2O_3	MnO	MgO	CaO	Na_2O	K_2O	P_2O_5	Total	LOI
165-1001A-													
53R-2, 75–80	489.3	49.7	1.37	16.1	10.6	0.19	8.51	11.22	2.33	0.02	0.09	100.1	ND
53R-3, 68–71	490.08	49.2	1.32	15.0	12.1	0.19	7.16	12.98	2.08	BDL	0.11	100.1	1.78
53R-4, 93–96	491.70	49.5	1.29	15.7	11.7	0.20	6.36	13.37	2.11	0.28	0.08	100.6	1.65
54R-1, 44–47	494.44	49.8	1.29	15.7	11.6	0.20	6.40	13.34	2.02	0.29	0.08	100.7	2.19
54R-3, 37–40	497.24	49.1	1.31	14.6	11.7	0.19	6.92	13.73	2.11	0.53	0.09	100.3	3.14
54R-4, 93–98	499.20	49.1	1.24	15.3	11.2	0.20	6.57	14.67	2.10	0.51	0.09	101.0	3.31
54R-5, 81–84	500.35	49.4	1.27	15.0	11.4	0.19	7.24	13.03	2.09	0.01	0.09	99.7	1.94
54R-6, 126–130	502.30	49.3	1.21	15.5	11.2	0.19	7.31	13.13	2.03	BDL	0.07	99.9	1.29
55R-1, 72–75	504.32	49.9	1.37	15.7	10.4	0.20	7.98	12.56	2.28	BDL	0.09	100.5	2.36
55R-2, 81–83	505.91	49.0	1.58	14.3	12.3	0.23	7.52	12.37	2.17	0.19	0.11	99.8	1.36
56R-1, 132–134	514.52	49.8	1.57	14.5	11.9	0.23	6.84	12.47	2.23	0.50	0.11	100.2	1.35
56R-2, 77–80	515.47	49.8	1.45	14.5	11.5	0.22	7.01	13.02	2.26	0.19	0.10	100.1	1.45
56R-3, 74–78	516.79	49.3	1.47	14.7	12.6	0.26	7.47	12.40	2.31	0.01	0.10	100.6	1.32
56R-3, 131–134	517.36	49.1	1.40	14.3	13.5	0.21	7.02	12.34	2.18	0.01	0.09	100.1	0.98

Notes: Shipboard XRF data; note that K_2O has been corrected by 0.25%. LOI = loss on ignition. ND = not determined. BDL = below limit of detection. This entire table also appears on CD-ROM (back pocket).

6 mm in diameter are present in the thicker basaltic units. The basal contact is a quenched glassy rind.

Formation D is an aphyric, 0.8-m-thick, pillow lava (Units 18 and 19 in Sections 165-1001A-54R-3 to 53R-4), with a chilled glassy top and base. The upper part is vesicular, and subvertical joints are filled by calcite.

Formation E is a 82-cm-thick massive basalt with a glassy top and a thin glassy lapilli basal layer (Units 20–22 in Sections 165-1001A-54R-4 and 5). At the base, there is a glassy contact with light gray to white carbonate sediment, about 2 cm in thickness. The sediment contains a large number of thick-walled benthic foraminifers typical of neritic environments in the Late Cretaceous (see "Biostratigraphy" section, this chapter).

Formation F is a thin basalt lava, also with a carbonate sediment lens at its base (Unit 23 in Section 165-1001A-54R-5).

Formation G is a 3.3-m-thick and sparsely plagioclase- and pyroxene-phyric basalt pillow lava (Units 24–26 in Sections 165-1001A-54R-6 and 54R-7). Chilled margins are common on some of the basaltic pieces, and there is a thin carbonate sediment layer at the base (Fig. 45).

Formation H is a 1.3-m-thick, sparsely plagioclase- and pyroxene-phyric basalt lava with a basaltic lapilli top (Units 28 and 29 in Section 165-1001A-55R-1). The basal contact is glassy.

Formation I is a plagioclase-phyric basaltic pillow lava (Units 30–38 in Sections 165-1001A-55R-1 to 55R-3), about 2.2 m thick. The bed contains several relatively thick units of massive basalt with chilled edges (70–100 cm thick), which likely represent individual pillows, associated with fragments of more glassy basalt above and below.

Formation J is a 1.4-m-thick, massive, fine-grained, sparsely plagioclase-phyric basalt lava (Units 39–48 in Section 165-1001A-55R-3). No glass contacts are observed, and the formation may represent a sill-like intrusion of magma into a growing lava flow.

Formation K is a 65-cm-thick, sparsely plagioclase-phyric basalt pillow lava (Units 49 and 50 in Section 165-1001A-56R-1). Individual basalt fragments have chilled glassy rinds and pipe vesicles near the margins. Thin intervals of microcrystalline to glassy basaltic breccia and lapilli are also present in the upper part, with white calcite cement infilling the angular vugs.

Formation L is an aphyric basalt lava, consisting of two beds (Units 51 and 52 in Sections 165-1001A-56R-1 to 56R-2). The upper bed is a 71-cm-thick basalt breccia and lapilli, with up to 6-cm basaltic clasts or veins with chilled glassy rinds that include relatively fresh or unaltered black to dark greenish black basaltic glass. The breccia and lapilli top is identical to that on Formation A at the top of the succession. The lower bed is a massive 206-cm-thick basalt that grades down from a microcrystalline upper part to a fine- to medium-grained lower part. Small vesicles are present in the upper part, but they decrease in abundance down to the end of the core.

The basement succession recovered in Hole 1001B consists of a single basalt lava formation, divided into an 60-cm-thick upper zone of sparsely plagioclase-phyric hyaloclastite breccia, grading down into a 3-m-thick massive plagioclase-phyric basalt, which persists to the base of the cored section. The structure and morphology of this flow is identical to the topmost flow recovered in Hole 1001A, but we consider the two to be different flows on the basis of phenocryst abundance, although they are only about 30 m apart.

Basalt Petrography

Basalts from Site 1001 display a wide variety of petrographic textures that primarily relate to the effects of quenching and the mode of eruption. A common lithology of the sequence is aphyric basalt, typified by the lower part of Formation A (Fig. 46). This basalt is fine to medium grained and equigranular, displaying a subophitic texture in the medium-grained interior flow, and an intersertal texture in the fine-grained outer part of the flow. Plagioclase occurs as euhedral laths up to 0.8 mm in length, with random orientation. These are partly poikilitically enclosed by subhedral crystals of clinopyroxene that range up to 0.9 mm in diameter. Oxides occur as subhedral to anhedral grains. Small amounts (~8%) of altered mesostasis, originally representing glass and some microlites, occur as irregular patches up to 0.4 mm and now highly altered to brownish smectite or "saponite." Vesicles are rare in this part of the unit, but they can range up to 1 mm in diameter. Most are spherical and filled with calcite and/or clay minerals. These aphyric basalts are texturally very similar to the "doleritic" basalts described from nearby DSDP Site 152 (Donnelly et al., 1973).

Another common lithology within the basement sequence of both Holes 1001A and 1001B is sparsely plagioclase-phyric basalt, such as in Formation G. This basalt is also fine to medium grained, with subophitic to intersertal texture (Fig. 47). The groundmass consists of euhedral plagioclase laths up to 0.8 mm long, intergrown with subhedral crystals of clinopyroxene and opaque minerals. Interstitial mesostasis forms irregular, altered patches of brownish smectitic clay, up to 0.4 mm in size. Phenocryst content is generally less than 2% and consists dominantly of euhedral to subhedral plagioclase crystals, sometimes occurring as glomeroporphyritic aggregates. The vesicle content is low, but it can range up to 5%, with most vesicles being spherical in shape and infilled with calcite or lined with clay minerals. Finer grained varieties of the sparsely phyric basalts are characterized by a more intersertal texture with smaller, more isolated euhedral laths of plagioclase. Many of the plagioclase microphenocrysts exhibit quench morphologies with distinctive belt-buckle

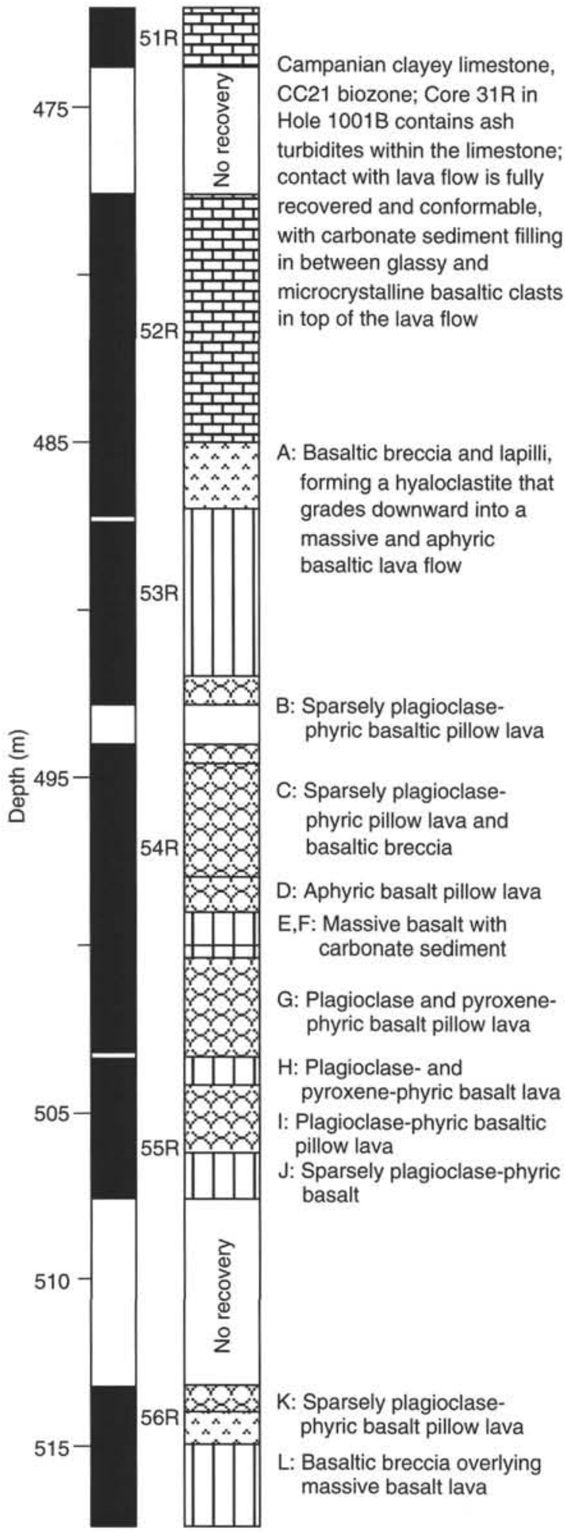

Figure 41. The Cretaceous basaltic basement succession in Hole 1001A includes 12 lava formations, which can be distinguished on the basis of petrography (especially phenocryst content) and glassy contact relationships. They consist dominantly of two flow types: pillow lavas and more massive sheet flows with hyaloclastite breccia tops. Column on left indicates core recovery (black).

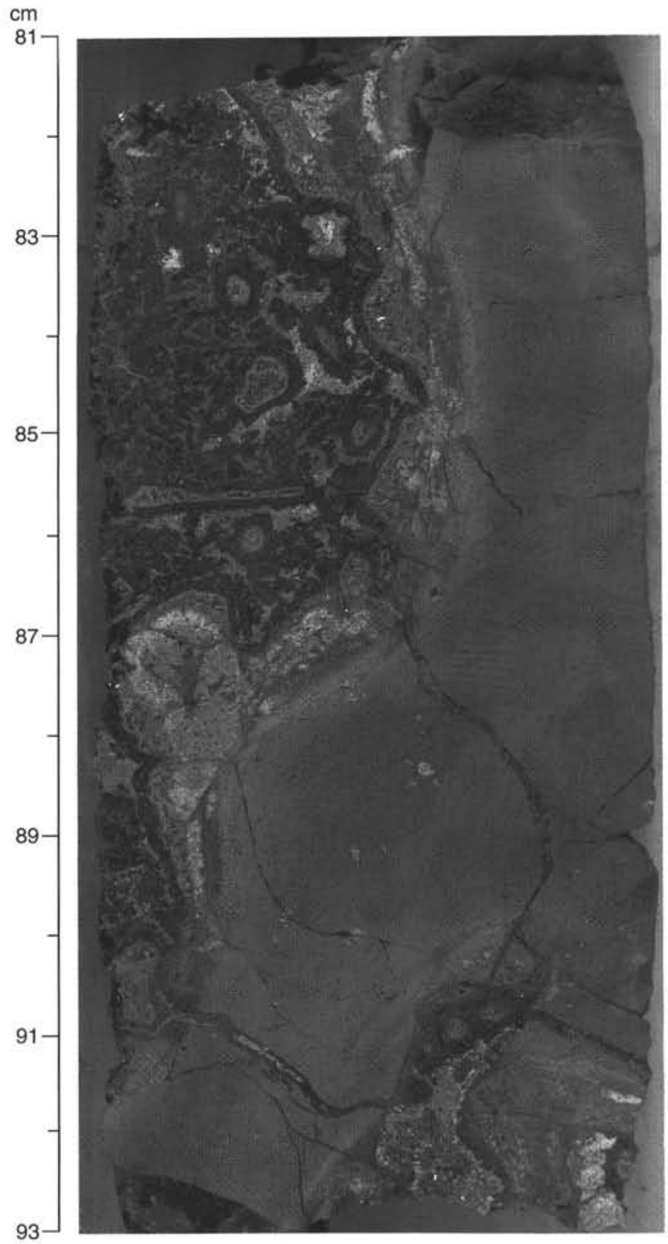

Figure 42. Veins or apophyses of basalt (right) intruding into the hyaloclastite breccia top of lava formation A. Spallation of the quenched margins of the basalt has contributed to the hyaloclastite matrix of the breccia (interval 165-1001A-52R-7, 81–93 cm).

outlines. The mesostasis of these basalts consists of a very fine-grained intergrowth of plagioclase, clinopyroxene, and opaque minerals. In addition there is up to 10% smectitic clay as an alteration product of interstitial glass.

Several flow units within the basaltic lava basement sequence are marked by quenched boundaries. The contact margins contain quenched microphenocrysts of plagioclase with a progressive inward development of spherulitic texture. Virtually all of the glassy margins appear to be palagonitized. Moving inward from the contact, the abundance of microphenocrysts of plagioclase and clinopyroxene increases in abundance and is accompanied by the formation of variolitic texture (Fig. 48). Phenocrysts of plagioclase up to 0.7 mm in length, sometimes as glomeroporphyritic aggregates, are also found

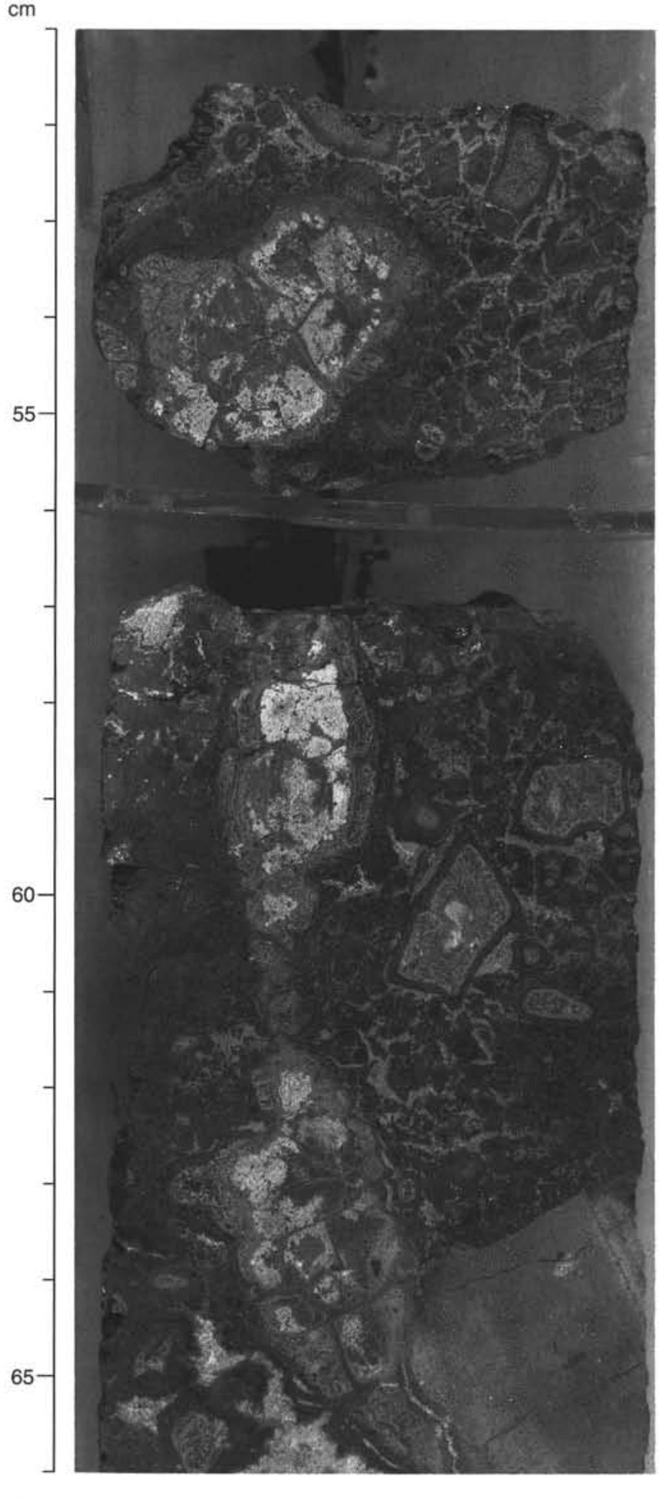

Figure 43. The upper part of basaltic veins in the hyaloclastite breccia has glassy margins, whereas the interior (light areas in photo) is extensively altered to smectite and chlorite (interval 165-1001A-52R-7, 51–66 cm).

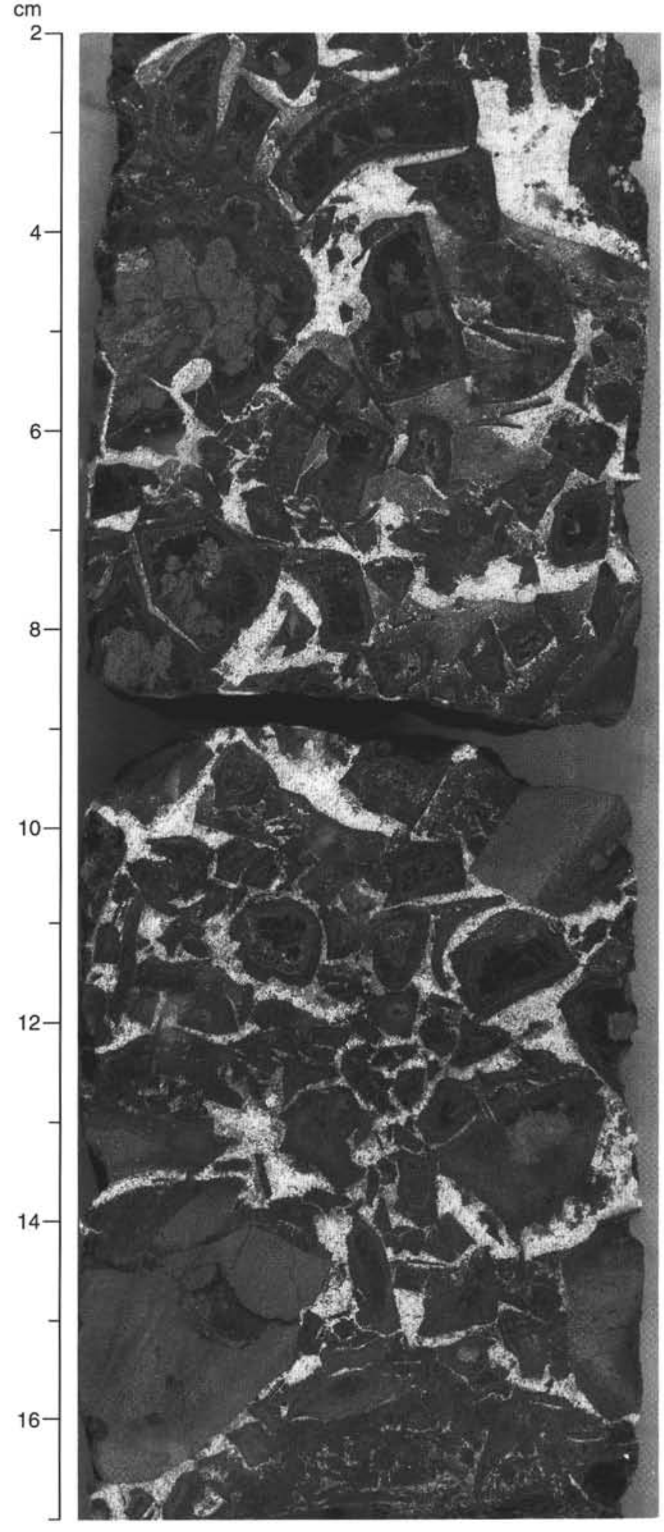

Figure 44. Clast-supported angular and cuspate glass shards and basalt fragments in a hyaloclastite breccia from formation A. In some places, the void spaces are filled in by secondary calcite (interval 165-1001A-52R-7, 2–17 cm).

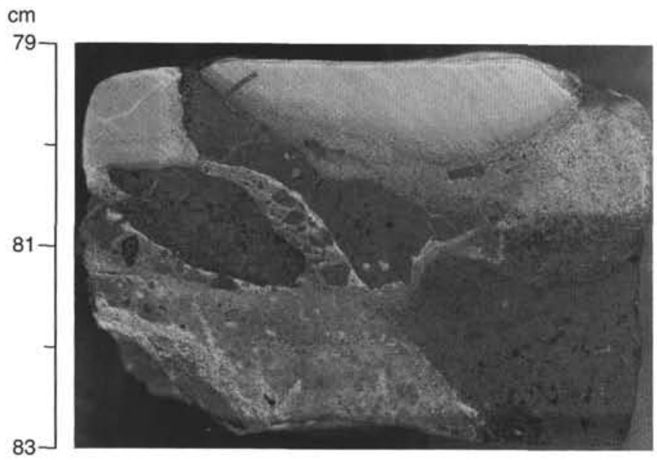

Figure 45. Lens of carbonate sediment at the contact between formations G and H (interval 165-1001A-54R-7, 79–83 cm). The fine-grained limestone contains thick-walled foraminifers, rounded clasts of both holocrystalline and glassy or variolitic basalt, and crystals of plagioclase and clinopyroxene. Veins of calcite and gypsum cut across the contact zone.

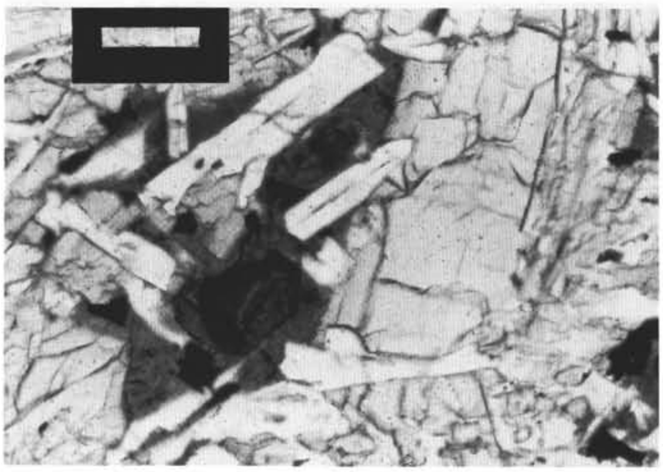

Figure 46. Aphyric basalt from interval 165-1001A-53R-3, 63–68 cm, showing subophitic texture with plagioclase laths partially enclosed by clinopyroxene. Altered glass occurs as irregular patches between crystals of plagioclase, clinopyroxene, and opaque minerals. Scale bar is 40 µm in length (transmitted light).

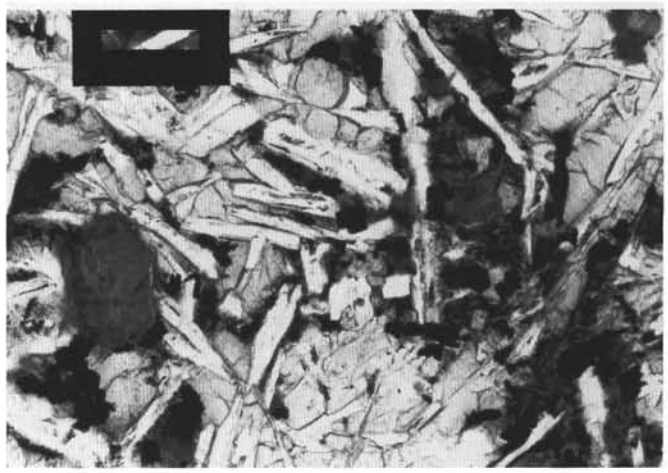

Figure 47. Sparsely plagioclase-phyric basalt from interval 165-1001A-54R-7, 15–16 cm, showing subophitic and intersertal texture. Elongate euhedral to subhedral plagioclase laths are partially enclosed by clinopyroxene. Interstitial mesostasis consists of altered glass and fine-grained intergrowths of plagioclase, clinopyroxene, and opaque minerals. Scale bar is 40 µm in length (transmitted light).

Figure 48. Sparsely plagioclase-phyric basalt from interval 165-1001A-55R-1, 112–114 cm, showing variolitic texture with radiating laths of plagioclase and clinopyroxene. Scale bar is 40 µm in length (transmitted light).

interior from the margin. Vesicles are common and spherical in shape, and range up to 1 mm in diameter. All are filled with either calcite or zeolites(?).

Within the basement sequence, there are also some thin (centimeter scale) intervals of carbonate sediment with foraminifers, interbedded between flow units. Basalts in contact with the sediment preserve quenched margins with remnant spherulitic structure. Glasses in the contact zone have been completely altered to smectitic clay and/or palagonite, and they contain possible pseudomorphs of olivine near the margins. Near the contact there are glomeroporphyritic aggregates of plagioclase and clinopyroxene up to 1 mm in length, together with quenched microphenocrysts of plagioclase. Vesicles are also common adjacent to the quenched margin and range up to 1.5 mm in diameter.

Geochemistry of Basalts

The major oxide composition of basalts from Site 1001 is given in Table 12, and the downcore variation in basalt chemistry in Figure 49. The basalts are tholeiitic, with notably high CaO contents, and they have MORB-like compositional affinities. There is a slight variation in both trace and major element composition downcore, and basalts below 505 mbsf in Hole 1001A define a separate group, with only slightly higher Fe, Ti, Zr, and Y (Table 13), but lower Al, Ca, Ni, and Cr than the basalts above (Fig. 50). However, the overall chemical variation is so slight that only very weak trends can be detected in major and trace element composition, such as might be caused by fractionation processes. We take this to indicate that the entire succession is from a single volcanic source. Their chemical characteristics are similar to the limited database of other basalts from the Caribbean Oceanic Plateau (Donnelly et al., 1973, 1990). The samples from basalts close to the sediment interface are significantly higher in MgO and lower in Fe_2O_3 and CaO. This trend is a result of the minor weathering or alteration of the topmost basalt, with an enrichment of Mg in the tri-octahedral smectites and a loss of Ca caused by the albitization of plagioclase.

Both Cr and Y are typically depleted in island-arc basalts relative to MORB and basalts from oceanic islands and plateaus (Pearce,

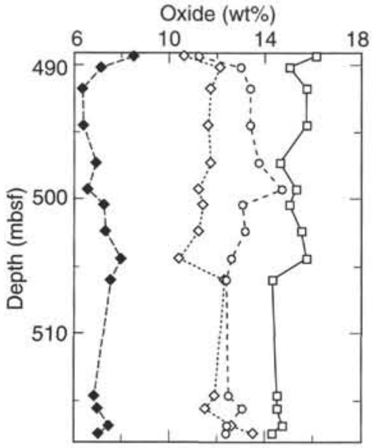

Figure 49. Major oxide composition of basalts in Hole 1001A exhibits minor variation downcore, with two principal basalt types identified (above and below 505 mbsf). The lower basalts are characterized by higher Al_2O_3 (open squares) and CaO (open circles) and by lower MgO (solid diamonds) and Fe_2O_3 (open diamonds). These variations are also observed in the trace element content, as shown in Figure 50. The trend to high MgO and low CaO and Fe_2O_3 in the topmost basalt is a result of weathering and the formation of tri-octahedral smectite in the flow and conversion of plagioclase to albite.

1982). As shown in Figure 51, the Site 1001 basalts do not have the characteristics of island-arc tholeiites, but rather show affinities with MORB. Similarly, the values of Y/Nb and Zr/Nb can be useful discriminants between plume-derived basaltic magmas and MORB. On such a plot, the Site 1001 basalts are transitional between depleted MORB and ocean-island basalts, indicating a mixed mantle source region for these Caribbean magmas (Fig. 52). The spread in Y/Nb and Zr/Nb is reasonably large and may be a function of source mixing or an indication of a heterogeneous source region.

Discussion

The basement recovered at Site 1001 is a basaltic submarine lava flow succession, consisting of 12 separate flow events with varying petrography and two principal lava flow types. They include aphyric basalts (Formations A, D, E, F, and L), which are typical of the most voluminous flows; sparsely plagioclase-phyric basalts (Formations B, C, I, J, and K), which are mainly pillow lavas; and sparsely plagioclase- and less common clinopyroxene-phyric basalts (Formations G and H). The contact relationships in both holes are the same, and indicate that the basalts were remarkably fresh and unweathered at the time of burial by carbonate sediment. Some of the basalts have thick, medium-grained and massive, vertically jointed interiors, overlain by a well-developed zone of hyaloclastite breccia. In the case of poor core recovery, such flows might be interpreted as sills, but the excellent recovery at this site shows clearly that they are of flow origin. We suggest that they represent sheet flows, associated with volcanic events of high mass eruption rate, where the flow rate is sufficiently high to overcome the tendency of a more slowly advancing lava to form pillows. The formation of hyaloclastite breccias on top of such flows will also aid in thermally insulating the fluid interior and hinder the formation of pillows. Furthermore, these thick hyaloclastite breccia components are likely to produce low-velocity layers within the volcanic succession, resulting in a strongly layered seismic velocity structure. All of the microcrystalline to fine-grained basalts are vesicular to a varying degree. This degree of vesiculation is taken as an indication of water depth at the time of eruption, and we note that these basalts are, for example, substantially more vesicular than the microcrystalline to glassy pillow lavas typically erupted on the mid-ocean ridge system. By analogy, with the degree of vesiculation on the Reykjanes Ridge, for example, we estimate water depths to be on the order of 1–2 km or less. Evidence from the microfossil assemblages in carbonate sediments supports this deduction (see "Biostratigraphy" section, this chapter).

Large igneous plateaus (LIPs) are huge volcanic provinces that may have been built up very rapidly as a result of localized volcanic events that are far in excess of the steady-state rates of normal accretion of basaltic magma at the ocean ridge. The apparently high rate of volcanism is analogous to that observed during the buildup of continental flood basalt provinces, and has led to the idea that LIPs are the result of focused magmatic activity from rising mantle plumes. Following the discovery of a prominent Caribbean-wide deep seismic reflector B″ that can be traced throughout the Venezuela Basin, on the Beata Ridge, and into the Colombian Basin (Ewing et al., 1968), basement drilling at five sites during DSDP Leg 15 (146, 150, 153, 151, and 152) demonstrated that the reflector corresponds to crust of basaltic composition that underlies much of the Caribbean Sea (Edgar, Saunders, et al., 1973). The Caribbean Oceanic Plateau has an area on the order of 600,000 km^2, and seismic refraction studies indicate that it has a thickness estimated up to 20 km, especially in the region of the Beata Ridge (Case et al., 1990).

At DSDP Site 146/149, drilling recovered a total of 11 m from two basaltic units. The sediment/basalt contact was not recovered, but, on the basis of a 2-cm chill zone at the base of the lower unit, the interpretation of the shipboard party was that dolerite sills had intruded into Coniacian limestone. Grain sizes range up to 0.3 mm in the upper unit and up to 0.1 mm in the lower unit. At Site 150, some 6.4 m of a fine-grained dolerite was recovered, but no contact was recovered. One meter of amygdaloidal basalt was recovered at Site 151, but no contact was seen. At Site 152, some 3.7 m of a weathered and vesicular basalt was recovered, with "marble" inclusions. Finally, at Site 153 some 3 m of amygdaloidal basalt was recovered, but no contact was seen.

The Late Cretaceous Caribbean basaltic crust is relatively enriched in large ion lithophile elements, and thus chemically unlike typical MORBs (Donnelly et al., 1973). Sen et al. (1988) and G. Waggoner (in Speed, 1987) have later shown that Leg 15 basalts and the correlative uplifted ocean floor basalts in the Dumisseau Formation in Haiti have $^{143}Nd/^{144}Nd$, $^{87}Sr/^{86}Sr$, and $^{206}Pb/^{204}Pb$ values unlike those of MORBs, and that their radiogenic isotope character is consistent with the derivation of the Caribbean Oceanic Plateau from the same mantle source as the Galápagos hot spot. Thus, the geochemical evidence is consistent with the model of the Caribbean Plate having drifted easterly from the Galápagos hot spot to its present position between the North and South American Plates (Duncan and Hargraves, 1984). The idea that the Caribbean Plate originated in the Pacific Ocean originates, however, with Wilson (1966). This idea will be tested further by detailed shore-based geochemical and radiogenic isotope studies of the recovered basalts.

PHYSICAL PROPERTIES

The physical properties program at Site 1001 included multisensor track (MST) and thermal conductivity measurements of whole-round cores, and *P*-wave velocity, index properties, electrical resistivity, and vane shear strength measurements of split cores. Methods for these measurements are described in the "Physical Properties" section of the "Explanatory Notes" chapter (this volume).

MST magnetic susceptibility and GRAPE data were recorded at 5-cm intervals at Site 1001, except for the interval around the K/T boundary (352–357 mbsf in Hole 1001A and 348–360 mbsf in Hole 1001B) and in the basalts (below 481 mbsf in Hole 1001A and below 479 mbsf in Hole 1001B), where magnetic susceptibility and GRAPE were recorded at 1-cm intervals. MST *P*-wave velocity data were re-

Table 13. Trace element composition of basalts from Site 1001.

Core, section, interval (cm)	Depth (mbsf)	Nb	Zr	Y	Sr	Rb	Zn	Cu	Ni	Cr	V
165-1001A-											
53R-2, 75–80	489.29	2.3	69	25	98	1.7	96	137	101	290	417
53R-3, 68–71	490.08	1.4	67	28	99	1.6	90	130	102	290	360
53R-4, 93–96	491.70	1.1	66	26	101	6.3	92	47	135	269	357
54R-1, 44–47	494.44	1.5	66	25	96	6.6	93	35	127	282	341
54R-3, 37–40	497.24	1.6	66	27	97	10.4	94	27	117	250	314
54R-4, 93–98	499.20	2.5	60	26	89	9.3	88	54	96	243	326
54R-5, 81–84	500.35	1.8	65	28	99	2.4	93	134	107	301	363
54R-6, 126–130	502.30	1.9	62	26	91	1.9	90	132	91	250	362
55R-1, 72–75	504.32	1.7	70	27	96	1.7	94	143	87	250	398
55R-2, 81–83	505.91	2.8	78	32	93	5.4	108	195	102	189	428
56R-1, 132–134	514.52	1.9	78	34	93	11.2	104	58	72	207	369
56R-2, 77–80	515.47	2.3	73	32	97	5.9	106	40	88	173	374
56R-3, 74–78	516.79	2.5	73	30	97	2.1	101	155	81	165	398
56R-3, 131–134	517.36	2.5	72	30	93	2.7	98	149	73	157	385

Note: This entire table also appears on CD-ROM (back pocket).

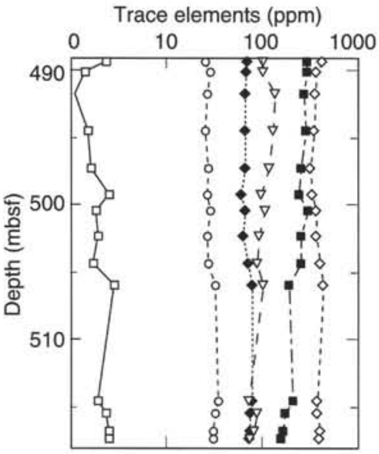

Figure 50. Downcore variation in trace element concentration (parts per million) of basalts in Hole 1001A. The basalt succession below 505 mbsf is, on the average, higher in Nb (open squares), Zr (solid diamonds), and Y (open circles), and lower in Ni (open inverted triangles) and Cr (solid squares).

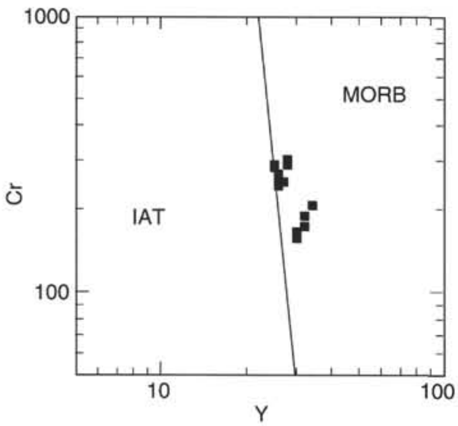

Figure 51. Cr vs. Y discrimination for Site 1001 tholeiitic basalts diagram. Note that the samples fall within the MORB field and display characteristics unlike island-arc tholeiites. (IAT; Pearce, 1982).

corded at 5-cm intervals in Hole 1001A to a depth of 165 mbsf; they were not recorded in Hole 1001B. MST natural gamma-ray measurements were made at 20-cm intervals, except for the interval around the K/T boundary and in the basalts, where NGR was measured every 10 cm. Only a few measurements of thermal conductivity were made at this site. Thermal conductivity was measured on Sections 1, 3, and

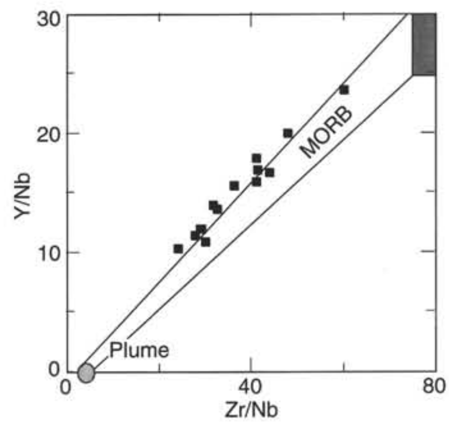

Figure 52. Y/Nb vs. Zr/Nb discrimination diagram indicates that Site 1001 tholeiitic basalts have affinities with a source that is intermediate or mixed between a MORB source and a plume source.

5 of Cores 165-1001A-12R to 18R from 103 to 167 mbsf, below which depth induration prevented insertion of the needles. Two measurements were also made in Core 165-1001B-1R at 26 and 29 mbsf.

P-wave velocity was measured on the split cores at a sampling interval of three per core, whereas samples for index properties were taken at an interval of six per core in Hole 1001A and three per core in Hole 1001B. Electrical resistivity was measured at a sample interval of three per core in Hole 1001A, to the depth at which induration prevented insertion of the needles for electrical resistivity (around 160 mbsf), and in the two spot cores of Hole 1001B at 26–29 mbsf and at 151–157 mbsf. Vane shear was measured in Hole 1001A to the depth at which induration prevented insertion of the vane for shear strength measurement (around 100 mbsf) and in Core 165-1001B-1R (26–29 mbsf); measurements were made at an interval of three per core.

Multisensor Track

Data from the MST measurements are presented in Figure 53 and in Tables 14 through 17. The GRAPE data follow the same trend as the bulk density determined from index properties (see below), but the GRAPE is offset to unrealistically low values below 165 mbsf, because the core does not fill the core liner below this depth. The magnetic susceptibility is 2 orders of magnitude higher in the basaltic basement than in the sediments. Within the sediments, relatively high values are found above the Eocene/Miocene unconformity near 165 mbsf (see below) and in the interval above the K/T boundary. The single peaks in magnetic susceptibility can be correlated from Hole 1001A to Hole 1001B, and the general pattern can be correlated between the MST data and the downhole magnetic susceptibility data

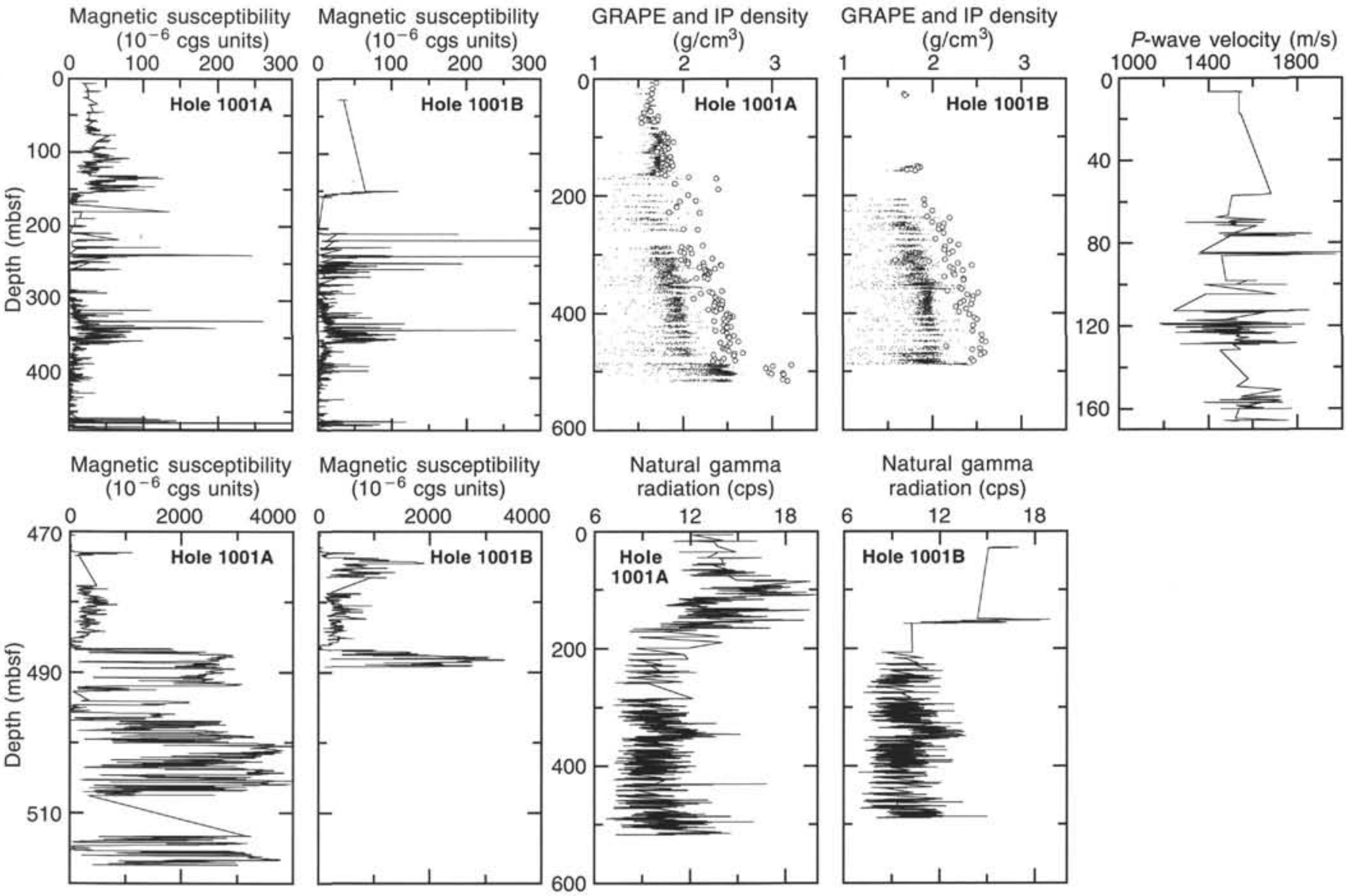

Figure 53. Multisensor track data showing magnetic susceptibility, GRAPE (with index properties density [open circles] for comparison), P-wave velocity, and natural gamma radiation vs. depth. For the basaltic basement interval, the magnetic susceptibility is shown on a separate scale.

Table 14. Magnetic susceptibility data for Site 1001.

Core, section, interval (cm)	Depth (mbsf)	Raw mean susc. (10^{-6} cgs)	SD susc.	Drift corr.	DAQ period (s)	Bkgd. corr.
165-1001A-						
2R-1, 5	6.45	17.4	5.973476	0	5	0.024
2R-1, 10	6.5	23.2	0.712541	0	5	0.038
2R-1, 15	6.55	25.2	0.804842	0.1	5	0.054
2R-1, 20	6.6	21.4	0.47155	0.1	5	0.069
2R-1, 25	6.65	27.4	1.011118	0.1	5	0.084
2R-1, 30	6.7	25.2	0.235775	0.1	5	0.1
2R-1, 35	6.75	28.8	1.470806	0.1	5	0.115
2R-1, 40	6.8	30.2	0.540569	0.1	5	0.13
2R-1, 45	6.85	33.8	0.712541	0.1	5	0.146
2R-1, 50	6.9	37	0.639679	0.2	5	0.172

Notes: Susc. = susceptibility, corr. = correction, SD = standard deviation, DAQ = data acquisition, and bkgd. corr. = background correction. The data in this table differ from the raw data in that (1) all columns do not appear, (2) depths have been added, (3) columns have been labeled, (4) unsuccessful measurements have been deleted, and (5) magnetic susceptibility values have been averaged.

Only part of this table is produced here. The entire table appears on CD-ROM (back pocket).

Table 15. Gamma-ray attenuation porosity evaluator (GRAPE) data for Site 1001.

Core, section, interval (cm)	Depth (mbsf)	Raw counts	DAQ period (s)	Density (g/cm^3)	Boyce corr. density (g/cm^3)
165-1001A-					
2R-1, 5	6.45	20449	3	1.741	1.67287
2R-1, 10	6.5	20728	3	1.715	1.64505
2R-1, 15	6.55	20729	3	1.714	1.64398
2R-1, 20	6.6	20316	3	1.753	1.68571
2R-1, 25	6.65	20636	3	1.723	1.65361
2R-1, 30	6.7	20173	3	1.767	1.70069
2R-1, 35	6.75	20833	3	1.705	1.63435
2R-1, 40	6.8	20530	3	1.733	1.66431
2R-1, 45	6.85	20444	3	1.741	1.67287
2R-1, 50	6.9	20475	3	1.738	1.66966

Notes: DAQ = data acquisition. Density = bulk density. Corr. = correction. The data in this table differ from the raw data in that (1) all columns do not appear, (2) depths have been added, (3) columns have been labeled, and (4) unsuccessful measurements have been deleted.

Only part of this table is produced here. The entire table appears on CD-ROM (back pocket).

from Hole 1001A (Fig. 54). Above the K/T boundary, the offset between the MST and log data of Hole 1001A is 110–115 cm, whereas below the boundary it is only 60 cm. Therefore, the gap between Cores 165-1001A-38R and 39R is actually only 15–20 cm and not 65 cm as estimated by the standard ODP method. Valid *P*-wave data were only obtained over shorter intervals. The natural gamma radiation is generally low over the entire depth interval (including the basalt), but a shift from relatively high to relatively low values is seen near 165 mbsf, corresponding to the shift in magnetic susceptibility, velocity, and index properties (see below).

Thermal Conductivity

Thermal conductivity data (Table 18; Fig. 55) occur within the interval between 1.1 and 1.4 W/(m·K).

Table 16. Multisensor track *P*-wave data for Site 1001.

Core, section, interval (cm)	Depth (mbsf)	*P*-wave velocity (m/s)	Raw mean time	Raw SD time	Raw mean displ.	Raw SD displ.	Mean signal level	DAQ period (s)	Linear thickness	Linear delay
165-1001A-										
2R-1, 10	6.5	1531.16	49.9	0.02	52	0	101005	5	5.1	2.5
2R-1, 15	6.55	1510.29	50.5	0	52	0	186005	5	5.1	2.5
2R-1, 20	6.6	1524.14	50.1	0.0316	52	0	151	5	5.1	2.5
2R-1, 25	6.65	1411.65	53.5	0.9452	51	0	880005	5	5.1	2.5
2R-1, 30	6.7	1550.12	49.3	0.04	51	0	10	5	5.1	2.5
2R-1, 35	6.75	1750.42	44.4	5.3498	51	0	61	5	5.1	2.5
2R-1, 40	6.8	1868.69	42	7.471	51	0	3	5	5.1	2.5
2R-1, 45	6.85	1539.33	49.6	0.04	51	0	11	5	5.1	2.5
2R-1, 50	6.9	1802.71	43.3	7.8756	51	0	44	5	5.1	2.5
3R-1, 95	17.05	1836.81	42.5	10.6452	49	0	23	5	5.1	2.5

Notes: SD = standard deviation, displ. = displacement, DAQ = data acquisition. The data in this table differ from the raw data in that (1) all columns do not appear, (2) depths have been added, (3) columns have been labeled, and (4) unsuccessful measurements have been deleted.

Only part of this table is produced here. The entire table appears on CD-ROM (back pocket).

Table 17. Natural gamma-ray (NGR) data for Site 1001.

Core, section, interval (cm)	Depth (mbsf)	GR (cps)	Win 1	Win 2	Win 3	Win 4	Win 5	DAQ period (s)
165-1001A-								
2R-1, 5	6.45	14.66	7.13	5.23	1.7	0.17	0.43	30
2R-1, 25	6.65	12.13	6.67	3.73	1	0.33	0.4	30
3R-1, 5	16.15	14.07	7.1	4.3	1.67	0.17	0.83	30
3R-1, 25	16.35	12.53	6.5	3.6	1.43	0.33	0.67	30
3R-1, 45	16.55	10.97	5.1	3.3	1.73	0.27	0.57	30
3R-1, 65	16.75	13.64	6.67	3.97	1.8	0.47	0.73	30
3R-1, 85	16.95	16.16	7.9	5.2	1.93	0.4	0.73	30
3R-1, 105	17.15	12.4	5.9	4.13	1.57	0.3	0.5	30
3R-2, 5	17.65	13.52	6.4	4.83	1.63	0.23	0.43	30
4R-1, 5	25.75	13.7	6.37	4.6	1.93	0.4	0.4	30

Notes: Win 1 through Win 5 = counts per second in each of five energy windows, corresponding to Schlumberger practice for spectral natural gamma-ray logs. DAQ = data acquisition. The data in the table differ from the raw data in that (1) all columns do not appear, (2) depths have been added, (3) columns have been labeled, and (4) unsuccessful measurements have been deleted.

Only part of this table is produced here. The entire table appears on CD-ROM (back pocket).

P-wave Velocity

Data from the velocity measurements on the split surface are presented in Table 19. The *P*-wave velocities were measured along the axis of the core as well as parallel to bedding by the Digital Sonic Velocimeter (DSV) down to a depth of around 100 mbsf. Below this depth, the sediments are more indurated and the *P*-wave velocities were measured in half cores parallel to bedding using the Hamilton Frame. In the basalt below 485 mbsf, the Hamilton Frame was used to measure *P*-wave velocities on discrete samples. As at Sites 998 and 1000 and in contrast to the more clay-rich sediments at Site 999, no significant difference between velocities along the core axis and parallel to bedding was seen at Site 1001. The change of measuring device at around 100 mbsf seems to have no influence on the continuity of the data.

The laboratory data for the sediments were corrected to in situ stress (Table 19; Fig. 56) by the empirical relation derived by Urmos et al. (1993) (see "Physical Properties" section, "Site 998" chapter, this volume), but comparison with log velocities (see "Downhole Measurements" section, this chapter) was difficult because of the poor quality of velocity log data below 170 mbsf.

The trend in velocity with depth for Site 1001 is similar to that found at Sites 998, 999, and 1000 down to a depth of about 165 mbsf, where a major discontinuity in velocity occurs at Site 1001 (Fig. 56). The discontinuity corresponds to unconformities between layers of Eocene and Miocene age (see "Biostratigraphy" section, this chapter). Below the unconformities, the interval down to 210 mbsf shows large variability in velocity (see "Index Properties," below), whereas a steady increase in *P*-wave velocities from around 2500 to 3500 m/s is seen in the lower section of sediments. The recovered basalt has *P*-wave velocities around 5000 m/s.

Index Properties

Index properties were measured for samples taken from split cores at those locations where the velocity measurements were made (Table 20; Fig. 57). For sediment samples, both wet and dry weights and wet and dry volumes were measured so that wet-bulk density, grain density, water content, porosity, and dry-bulk density could be calculated (see "Explanatory Notes" chapter, this volume). For basement samples only the bulk density was determined.

Although variations in index property data from Site 1001 are primarily governed by burial depth and the contrast between sediments and basalt, they are influenced also by the presence of the unconformity near a depth of 165 mbsf. Above this depth, porosities are between 70% and 58%, and wet-bulk densities between 1.6 and 1.8 g/cm^3. The unconformity is marked by a shift to higher values in wet-bulk density and corresponding shifts in porosity and water content. Below the unconformity, the interval down to 210 mbsf shows large variability. Porosities in this interval vary from 60% to values as low as 20%. These low porosities correspond to intervals with high-velocity peaks and to grain densities of 2.25 g/cm^3. The latter data indicate a high content of hydrated silica in these zones. The lower section of sediments, down to the basaltic basement, is characterized by grain densities around 2.72 g/cm^3, a steady porosity decrease from around 55% to near 20%, and a corresponding increase

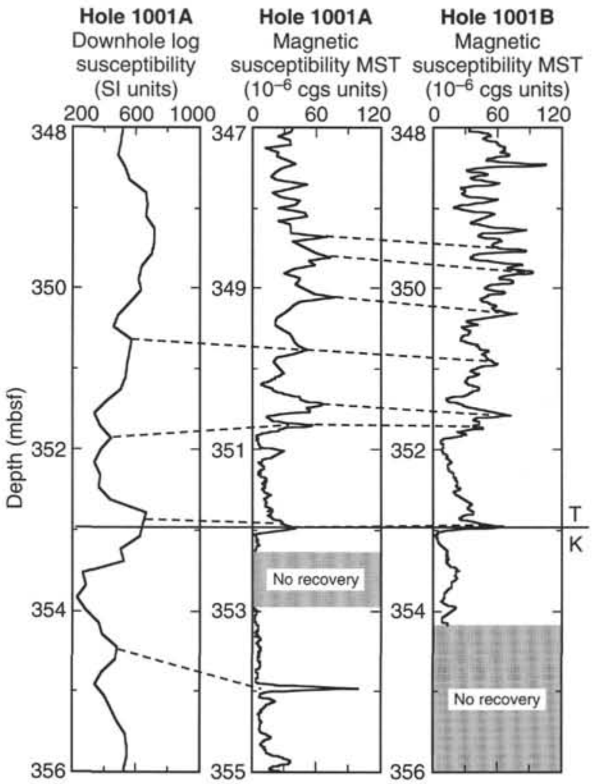

Figure 54. Correlation between magnetic susceptibility over the K/T boundary as measured by the downhole tool in Hole 1001A and as measured by the MST of Holes 1001A and 1001B. The offset between the downhole measurements and the MST data of Hole 1001A is caused by the difference between the wireline depth and the drilling depth.

Table 18. Thermal conductivity measured on whole-round core sections for Site 1001.

Core, section, interval (cm)	Depth (mbsf)	Thermal conductivity (W/[m·K])
165-1001A-		
12R-1, 30.0–30.1	102.90	1.247
12R-3, 30.0–30.1	105.90	1.309
12R-5, 30.0–30.1	108.90	1.284
13R-1, 30.0–30.1	112.50	1.238
13R-3, 30.0–30.1	115.50	1.236
13R-5, 30.0–30.1	118.50	1.247
14R-3, 30.0–30.1	125.10	1.240
14R-5, 30.0–30.1	128.10	1.277
15R-1, 30.0–30.1	131.80	1.132
15R-3, 30.0–30.1	134.80	1.201

Only part of this table is produced here. The entire table appears on CD-ROM (back pocket).

in wet-bulk densities from 2.0 to 2.6 g/cm^3. The recovered basalt has densities between 2.9 and 3.2 g/cm^3.

Electrical Resistivity

Electrical resistivity data were collected at the same locations where the velocity measurements were made. The electrical resistivity data are presented in Table 21 and Figure 58. The electrical resistivity decreases from around 0.6 Ωm near the seafloor to around 0.45 Ωm at 60 mbsf, below which depth the trend reverses and the resistivity increases to 0.9 Ωm at 160 mbsf, where the last data were collected. The electrical formation factor, F, was calculated from $F = R_o/R_w$, where R_o is the resistivity of the sediment and R_w is the resistivity of the pore water. The pore-water resistivity was assumed to be that of

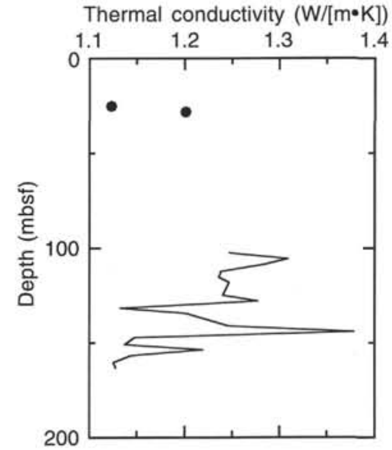

Figure 55. Thermal conductivity vs. depth measured on whole cores. Data from Hole 1001A are connected by a line, whereas the solid circles represent data from Hole 1001B.

Table 19. DSV (DSV1 and DSV2) and Hamilton Frame (DSV3) velocities measured at discrete intervals for Site 1001.

Core, section, interval (cm)	Depth (mbsf)	Instrument	Velocity (km/s)	Urmos correction (km/s)	Corrected velocity (m/s)
165-1001A-					
2R-1, 30–30.1	6.7	DSV1	1.579	0.009	1588
2R-1, 30–30.1	6.7	DSV2	1.581	0.009	1590
3R-1, 30–30.1	16.4	DSV1	1.574	0.023	1597
3R-1, 30–30.1	16.4	DSV2	1.620	0.023	1643
3R-2, 30–30.1	17.9	DSV1	1.591	0.025	1616
3R-2, 30.1–30.2	17.9	DSV2	1.590	0.025	1615
4R-1, 30–30.1	26	DSV1	1.595	0.035	1630
4R-1, 30–30.1	26	DSV2	1.604	0.035	1639
5R-1, 30–30.1	35.6	DSV2	1.616	0.048	1664
5R-1, 30.1–30.2	35.6	DSV1	1.609	0.048	1657

Note: DSV = Dalhousie University/Bedford Institute of Oceanography Digital Sonic Velocimeter.

Only part of this table is produced here. The entire table appears on CD-ROM (back pocket).

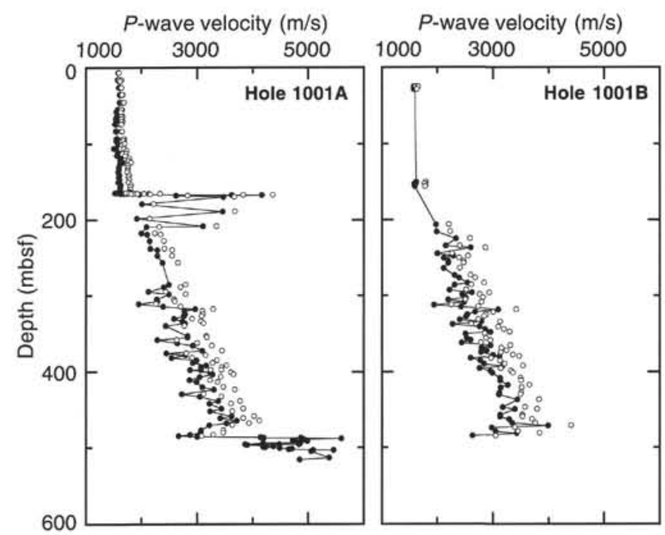

Figure 56. *P*-wave velocities for Holes 1001A and 1001B. Measured values are presented as solid circles connected by lines, whereas the open circles refer to depth-corrected values.

Table 20. Index properties measured at discrete intervals for Site 1001.

Core, section, interval (cm)	Depth (mbsf)	Water content (bulk wt%)	Bulk density (g/cm^3)	Grain density (g/cm^3)	Dry density (g/cm^3)	Porosity (%)
165-1001A-						
2R-1, 29–31	6.69		1.70			
3R-1, 29–31	16.39	41.23	1.66	2.75	0.98	66.83
4R-1, 29–31	25.99	42.03	1.66	2.72	0.96	68.02
5R-1, 29–31	35.59	38.84	1.64	2.76	1.00	62.15
6R-1, 29–31	45.19	39.30	1.61	2.77	0.98	61.77
6R-2, 29–31	46.69	41.35	1.60	2.81	0.94	64.49
7R-1, 29–31	54.89	40.41	1.63	2.72	0.97	64.44
7R-2, 29–31	56.39	41.20	1.64	2.80	0.97	66.01
7R-3, 29–31	57.89	38.40	1.57	2.75	0.97	58.75
8R-1, 29–31	64.49	41.21	1.73	2.82	1.01	69.43

Only part of this table is produced here. The entire table appears on CD-ROM (back pocket).

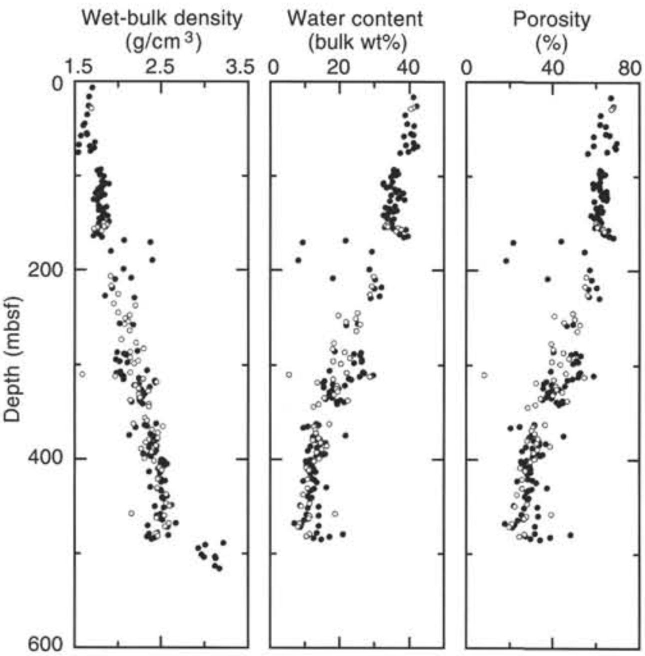

Figure 57. Bulk density, water content, and porosity vs. depth, Holes 1001A (solid circles) and 1001B (open circles).

seawater at 20°C (0.206 Ωm). The porosity, Ø, was calculated from the formation factor by Archie's equation:

$$F = a/(Ø)^m,$$

assuming (1) $a = 1$ and $m = 2$ and (2) $a = 1$ and $m = 3$. The resulting porosity data are plotted on Figure 58. Archie-porosities calculated with $m = 2$ are closest to the index properties data above 100 mbsf, whereas Archie-porosities calculated with $m = 3$ are closest to the index properties data below 120 mbsf. This change probably reflects the decrease in carbonate content of the sediments with depth (see "Lithostratigraphy" section, this chapter).

Vane Shear Strength

The ODP motorized minivane was used to measure undrained shear strength in split-core sections (Table 22; Fig. 59). These measurements were made at the depths also used for P-wave velocity determination. An overall increase in shear strength with depth is evident.

Table 21. Electrical resistivity measured at discrete intervals for Site 1001.

Core, section, interval (cm)	Depth (mbsf)	Resistivity (Ωm)
165-1001A-		
2R-1, 30.1–30.1	6.70	0.61
3R-1, 30.1–30.1	16.40	0.56
3R-2, 30.1–30.1	17.90	0.51
4R-1, 30.1–30.1	26.00	0.53
5R-1, 30.1–30.1	35.60	0.49
6R-1, 30.1–30.1	45.20	0.45
7R-1, 30.1–30.1	54.90	0.43
7R-3, 30.1–30.1	57.90	0.46
8R-1, 30.1–30.1	64.50	0.40
8R-3, 30.1–30.1	67.50	0.43

Only part of this table is produced here. The entire table appears on CD-ROM (back pocket).

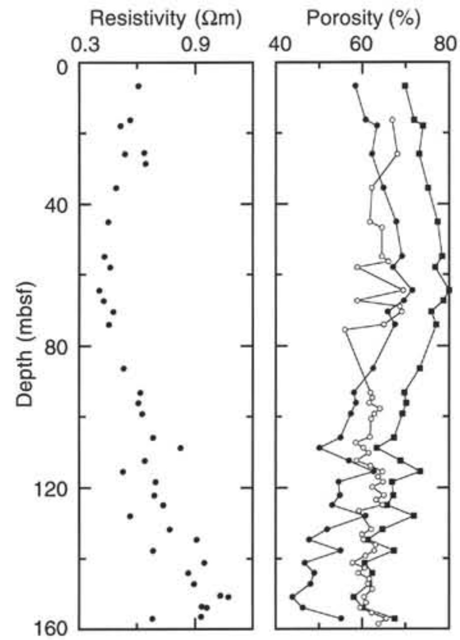

Figure 58. Electrical resistivity and Archie-porosity vs. depth. The Archie porosity is calculated under the assumption of $m = 2$ (solid circles) as well as $m = 3$ (solid squares). For comparison, index properties porosity is also plotted (open circles).

Table 22. Undrained and residual shear strength from miniature vane shear measurements for Site 1001.

Core, section, interval (cm)	Depth (mbsf)	Undrained shear strength (kPa)	Residual shear strength (kPa)
165-1001A-			
2R-1, 30.0–30.1	6.70	13.4	7.0
3R-1, 30.0–30.1	16.40	16.4	9.5
3R-2, 30.0–30.1	17.90	11.9	6.1
4R-1, 30.0–30.1	26.00	20.2	13.9
5R-1, 30.0–30.1	35.60	14.1	11.8
6R-1, 30.0–30.1	45.20	30.1	25.1
7R-3, 30.0–30.1	57.90	40.7	21.1
8R-1, 30.0–30.1	64.50	27.3	14.3
8R-5, 30.0–30.1	70.50	6.9	4.8
9R-1, 30.0–30.1	74.10	25.5	9.5

Only part of this table is produced here. The entire table appears on CD-ROM (back pocket).

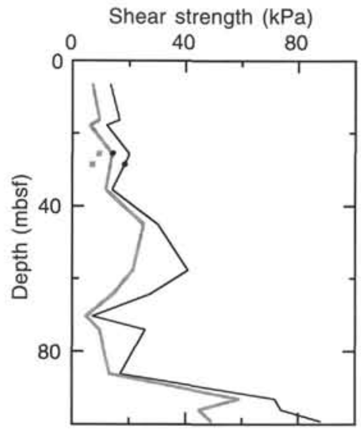

Figure 59. Undrained shear strength (Hole 1001A = solid line, Hole 1001B = solid circles) and residual shear strength (Hole 1001A = shaded line, Hole 1001B = shaded squares) vs. depth.

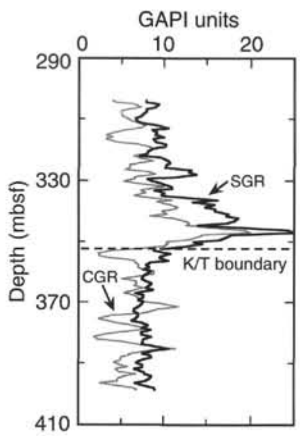

Figure 60. The total natural gamma-ray (SGR) and the K plus Th signal (CGR) over the depth interval containing the K/T boundary in Hole 1001A. The K/T boundary is near a marked decrease in natural gamma-ray intensity when crossing from Paleogene into Cretaceous sediments.

Gammaspectrometry of the Cretaceous/Tertiary Boundary Section[3]

For the depth interval containing the K/T boundary of Hole 1001A, the total gamma radiation (SGR) and the computed K plus Th gamma radiation (CGR) from the downhole logs (see "Downhole Measurements" section, this chapter) are plotted in Figure 60, where the level of the K/T boundary is tentatively indicated as reported in the "Lithostratigraphy" and "Biostratigraphy" sections, this chapter. The overall intensity in natural gamma radiation is lower in Hole 1001A than in Hole 999B (see Fig. 60), and the difference is accompanied by a general lower contribution from K plus Th relative to U. This pattern probably reflects the overall higher clay content in the Hole 999B sediments relative to Hole 1001A. The lowermost 20 m of the Paleogene has a relatively high natural gamma-ray intensity so that when crossing from Paleogene into Cretaceous sediments a decrease in the gamma-ray intensity is seen. This is obvious in Hole 1001A, and might well be the case in Hole 999B, where only a few meters of Cretaceous sediments were penetrated.

Figure 61 shows K, Th, and U data for a short interval crossing the K/T boundary in Hole 1001A, a K/(Th+U) plot of the same data, and, for comparison, K/(Th+U) for the equivalent section of Hole 999B. Similar to what was found in Hole 999B, low K/(Th+U) is seen near the K/T boundary in Hole 1001A, although the K, Th, and U data are widely different in the two holes. Spectral natural gamma-ray measurements of the K/T boundary clay at Stevns, Denmark, also record anomalously low K relative to Th and U (Engell-Jensen et al., 1984).

DOWNHOLE MEASUREMENTS

Operations

After drilling to a total depth of 522.8 mbrf in Hole 1001A, a complete wiper trip was made to condition the borehole for logging. Cuttings not removed by circulated seawater were swept out of the hole with bentonite gel mud introduced into the hole during conditioning operations. With the pipe set near the bottom of the hole, the bit was released and the pipe was then raised for logging. While raising the drill pipe, a slug of barite mud was pumped down the drill pipe to prevent seawater from flowing out of the pipe and onto the rig floor.

Wireline logging operations began in Hole 1001A at 21:00 UTC on 6 February 1996. All logging operations were completed by 01:00 UTC on 8 February, corresponding to a total logging time of 28.0 hr (Table 23). Each tool string was run to the bottom of the hole and then pulled upward at a rate between 300 and 600 m/hr, to acquire high-resolution log data. During the Quad combo (QC) and Formation MicroScanner (FMS) upward logging runs, the pipe was raised 28 m (to a depth of 83.8 mbsf) to allow more of the hole to be logged. A repeat section was also run with each tool string to provide data quality control.

The QC tool string included, from top to bottom, the telemetry cartridge, natural gamma spectroscopy, long-spaced sonic, compensated neutron, lithodensity, dual induction resistivity, and Lamont temperature tools. The QC tools were run down to the bottom of the hole to a depth of 485 mbsf, as determined by wireline measurements. A brief 2-min stop was made at the seafloor to allow the temperature tool to equilibrate to bottom temperatures. The total depth reached by the tool string in the hole was approximately 37.8 m above the total hole depth, as measured by the drillers. The tool string most likely encountered a ledge near the basement/sediment interface, rather than cuttings and debris filling the lower 37.8 m of the hole. During the first upward logging run, data were acquired as the tool string was raised at a rate of 300 m/hr, from 485 mbsf to seafloor depth (Table 23). The final upward QC run was completed by acquiring data in a 90.1 m repeat section between 228.4 and 138.3 mbsf.

The FMS included telemetry, natural gamma spectroscopy, and FMS sections. To assist the tool in descending to total depth more quickly, downward pressure was applied to the tool by pumping seawater down the drill pipe. High-resolution data were collected with the FMS between 420 and 100.5 mbsf, as the tool was raised at a rate of 300 m/hr (Table 23). A second run from 412.2 to 165.8 mbsf was run for quality control.

The geological high sensitivity magnetic tool (GHMT) string, including telemetry, natural gamma spectroscopy, and GHMT sections, was the final tool string used in the hole. At a depth of 152 mbsf, an obstruction was encountered that prevented further penetration of the borehole. Several unsuccessful attempts were made to maneuver past the restriction. The GHMT tool string was removed from the borehole and a second wiper trip began. The drill pipe was run down unimpeded to a depth of approximately 420 mbsf and the drill pipe was then pulled up to a depth of 188.8 mbsf for logging again. The GHMT tool string was run in the hole a second time and a total depth of 405.2 mbsf was reached. Logging data were recorded from 405.2 to 204 mbsf as the tool string moved uphole at 600 m/hr (Table 23). A second upward run was made with the GHMT between 403.8 and 190.9 mbsf.

[3]D.E. Paulsen, Department of Automaton, Technical University of Denmark b. 322, DK-2800 Lyngby, Denmark, and I.L. Lind, Department of Geology and Geotechnical Engineering, Technical University of Denmark, b. 204, DK-2800 Lyngby, Denmark.

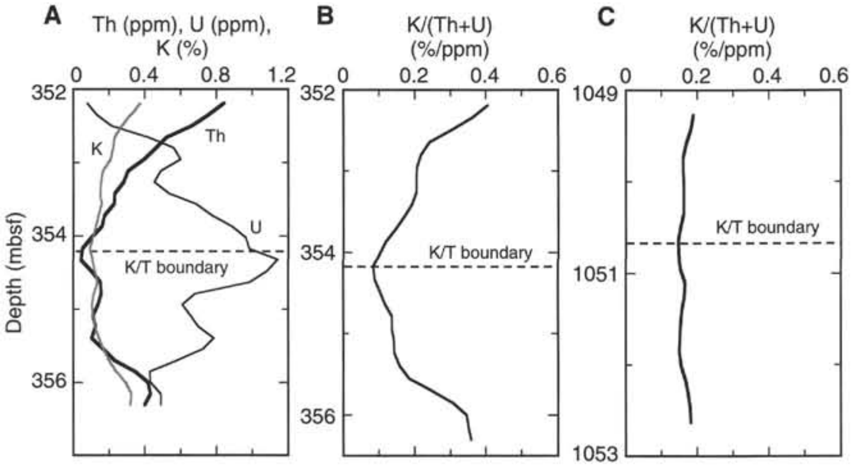

Figure 61. Th, U, and K (**A**) and the K/(Th+U) ratio (**B**) for downhole logging data of Hole 1001A. For comparison, K/(Th+U) of the equivalent interval in Hole 999B is shown plotted on a scale similar to that for Hole 1001A (**C**). The Hole 999B data are the same as presented in Figure 70 in the "Site 999" chapter, this volume.

Table 23. Time schedule (UTC) for logging operations at Hole 1001A, including a listing of the tools used during each logging run.

Time (UTC)	Activity
6–8 February 1996	
Drillers' TD = 3793.8 mbrf (522.8 mbsf), WD = 3271 mbrf	
2100	Prepare cable. Quad combo assembled and prepared for logging.
0020	Run in hole with Quad combo (TLT/DIT/HLDT/CNT/SDT/NGT/TCC/LEH-QT).
0230	Begin logging first upward pass (485–0 mbsf). Pull pipe up 28 m to 83.8 mbsf. Log 90.1-m repeat section (228.4–138.3 mbsf).
0500	Quad combo pulled out of drill string.
0600	Quad combo disassembled and removed from rig floor.
0630	FMS assembled and prepared for logging.
0650	RIH with FMS.
0830	Touch bottom and begin logging first logging upward run (420–100.5 mbsf). Pull pipe up 28 m to 83.8 mbsf. Complete second logging run (412.2–165.8 mbsf).
1015	FMS pulled out of drill string.
1145	FMS disassembled and removed from rig floor.
1155	GHMT assembled and prepared for logging.
1215	GHMT lowered into drill string.
1500	Encountered bottom at 161 mbsf, pull tool out of hole.
1630	GHMT removed from drill pipe and begin wiper trip.
1815	Complete wiper trip and set drill pipe at 189 mbsf. Begin second attempt to log hole with GHMT.
2100	Touch bottom at 405.2 mbsf and begin first upward logging pass (405.2–204 mbsf). Complete second logging run (403.8–190.9 mbsf).
2230	GHMT pulled out of drill string.
0015	GHMT disassembled and removed from rig floor.
0100	End logging operations.

Note: TD = total depth, WD = water depth.

Log Quality

In general, the data from all three tool strings appear to be of high quality; however, the sonic log and GHMT were particularly noisy. The sonic log is characterized by almost continuous cycle skipping below 170 mbsf, most likely caused by the severe rugosity of the borehole in alternating chalk, limestone, and chert-rich layers. It will be necessary to pick traveltimes from the sonic waveforms during post-cruise processing to produce a useful sonic log. The noise observed on the GHMT is very localized and occurred randomly during both runs. This noise is related to an electronics problem of a tool, which was isolated after logging operations were completed. The bulk density and the photoelectric (PEF) values are not valid above 100 mbsf, where the caliper arms were closed.

Additional processing (including depth shifting) of logging data was conducted onshore by the Borehole Research Group. The results are presented in Figures 62 and 63 at the end of this chapter, and on a CD-ROM disk in the back pocket of this volume. Detailed information regarding shore-based log processing is given in the "Downhole Measurements" section of the "Explanatory Notes" chapter (this volume).

Logging Units

Four logging units were identified in Hole 1001A (Figs. 62, 63), based on log response and analyses of recovered cores, but these should not be confused with the lithologic units defined earlier ("Lithostratigraphy" section, this chapter). The boundaries between adjacent logging units were placed at significant inflection points resulting from simultaneous variations on several of the logs (Figs. 62, 63). These units display consistent log responses or distinct overall trends.

The lithologies for unrecovered intervals can be inferred from the logs, based on the broad assumption that the logging tools respond to varying proportions of the primary constituents in samples actually recovered (e.g., carbonate, clay, volcanic ash, and biogenic silica) and to their relative porosity.

Logging Unit 1 (83 to 167 mbsf)

Logging Unit 1 is distinguished by uniformly low resistivity (<1 Ωm), velocity (<1.7 km/s), and slightly increasing and more variable density (1.3–1.75 g/cm^3) and PEF values. This unit is characterized by the lowest values of velocity, density, and resistivity observed in the entire logged section. Total gamma-ray counts reach absolute maximum values (>20 API) above ~112 mbsf, but are variable and decrease steadily downhole, primarily following the change in Th concentration. Density and PEF values increase rapidly from 110 to 120 mbsf, where they remain elevated and more variable. This trend is matched by uniformly decreasing concentrations of K, U, and Th over the same interval. In addition, nearly constant velocity and resis-

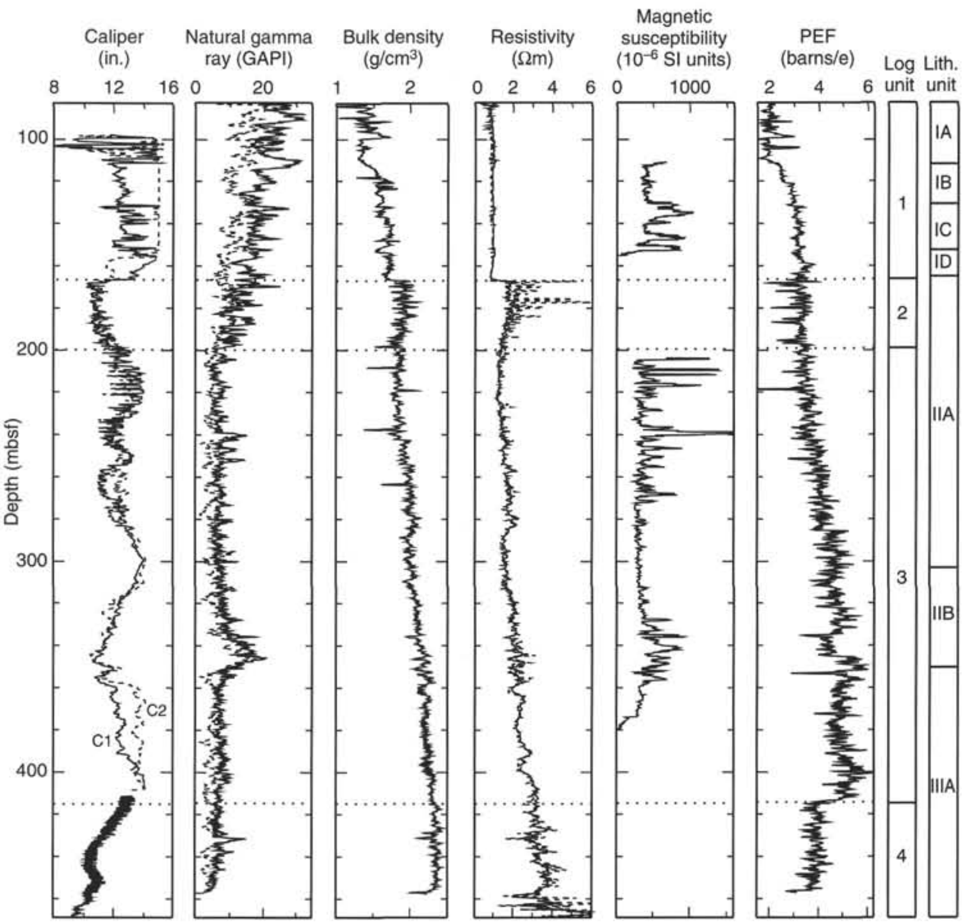

Figure 62. Selected downhole logs for the interval from 85 to 470 mbsf in Hole 1001A: (1) caliper measurements from the FMS tool are shown for the interval from 100 to 412 mbsf and from the Quad combo tool string below 412 mbsf; (2) total natural gamma ray, bulk density, resistivity, and photoelectric effect (PEF) measurements are from the Quad combo tool string; and (3) magnetic susceptibility measurements are from the GHMT tool string. Depth intervals of logging units are marked by dotted lines. The lithologic units are defined in the "Lithostratigraphy" section (this chapter). Resistivity and density reflect the porosity of the formation and therefore the degree of lithification or cementation. The PEF and gamma ray can be used as lithologic indicators.

tivity values are observed from 112 to 132 mbsf, followed by a marked increase in variability.

Logging Unit 1 corresponds to the lower portion of lithologic Subunit IA, and all of Subunits IB (112–132 mbsf), IC (132–153 mbsf), and ID (153–166 mbsf). The maximum gamma-ray counts and relatively low velocity, density, and PEF values above 110 m are consistent with the relatively low carbonate content (~52%; i.e., high clay content) of the clayey nannofossil ooze of lithologic Subunit IA ("Geochemistry" and "Lithostratigraphy" sections, this chapter). The rapid rise in density and PEF and declining gamma-ray counts is consistent with the sharp increase in carbonate concentration (>70%) at 112 mbsf, which defines the lithologic Subunit IA/IB boundary. The degree of lithification increases from Core 165-1001A-13R (112–122 mbsf) to Core 16R (141–151 mbsf), where the lithology is characterized by layers of soft chalk interbedded with nannofossil ooze ("Lithostratigraphy" section, this chapter). The increased density values, decreased gamma-ray counts, and increased variability of velocity and resistivity may be a response to the onset of interbedded chalky layers and nannofossil ooze with decreasing clay content. The gamma-ray response indicates that clay content decreases downhole from maximum values above 112 mbsf, reaching constant low values below 200 mbsf. Thorium vs. potassium concentrations in the interval from 85 to 110 mbsf fall largely within the montmorillonite (smectite) clay field and within both the illite and montmorillonite clay fields for the entire logging Unit 1 interval (Fig. 64). The dominance of montmorillonite (with minor chlorite) in Unit 1, indicating an igneous parental material, is consistent with an elevated terrestrial component within the sediment above 167 mbsf inferred from geochemical studies ("Geochemistry" section, this chapter). Three thick ash layers (18–25 cm thick) are reported in Core 165-1001A-18R at approximately 163 mbsf; however, only minor peaks in Th occur. Interestingly, this interval is associated with the absolute maximum in U concentration (1–1.5 ppm; Fig. 63; "Igneous Petrology and Volcanology" section, this chapter). The carbonate crash reported for lithologic Subunit IC may be reflected in an isolated minimum in density (~1.6 g/cm³) and maxima in Th and K at ~153 mbsf.

The lower boundary of logging Unit 1, at 167 mbsf, is marked by an abrupt increase in velocity, density, and resistivity values and a continued steady decrease in total gamma-ray counts. This abrupt change in physical properties creates the large impedance contrasts, which corresponds to the high-amplitude reflection known as seismic horizon A″ (see "Seismic Stratigraphy" section, this chapter).

Logging Unit 2 (167–200 mbsf)

Logging Unit 2 is characterized by a distinct increase in the amplitude and frequency of variation in resistivity, density, and PEF. Average resistivity and density values remain uniformly high from 167 to 180 mbsf and steadily decrease, along with total gamma-ray counts, until 200 mbsf.

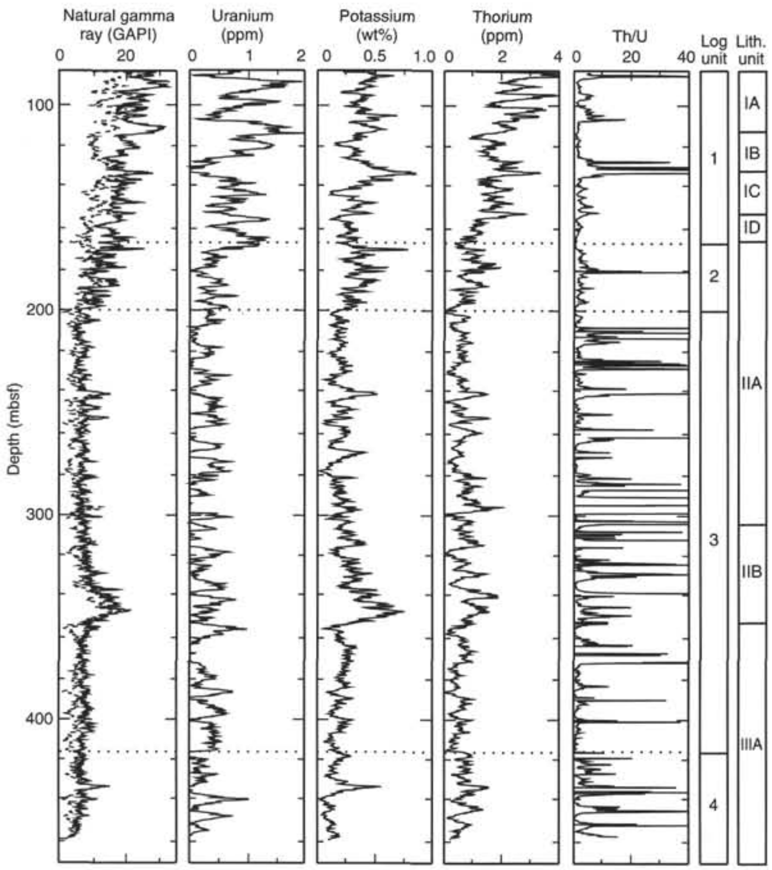

Figure 63. Downhole logs from the natural gamma-ray spectrometry tool on the Quad combo tool string for the interval from 85 to 460 mbsf in Hole 1001A, which give the total natural gamma ray, uranium, potassium, thorium, and Th/U. Depth intervals of logging units are marked by dotted lines. At Site 1001, maxima in the above elements and elemental ratios correlate with discrete ash fall layers and/or clay-rich intervals.

Logging Unit 2 corresponds to an extended interval with the lowest core recovery recorded during Leg 165. This interval correlates to the top 33 m of lithologic Unit II, which consists of calcareous chalk with interbedded chert layers ("Lithostratigraphy" section, this chapter). The logging response (elevated values and high variability) is consistent with large contrasts in induration of the interbedded chalk, clayey chalk, and chert. Numerous distinct minima in PEF values (~2 barns/e) are also observed, and these values approach those measured for cristobalite and opal (1.81 barns/e). The FMS reveals an image of extreme variations in resistivity, characterized by numerous discrete, thin, high-resistivity bands within wider zones of low resistivity. These bands of high resistivity are interpreted as individual chert lenses, which become thinner and less numerous with depth. The logging data indicate that this interval contains the greatest number of individual chert layers (or silicified zones) and will be especially important for reconstructing the lithostratigraphy of this low recovery zone (Fig. 14, "Lithostratigraphy" section, this chapter).

Logging Unit 3 (200–416 mbsf)

Logging Unit 3 is characterized by uniformly low gamma-ray counts (<10 API), and resistivity and density values become much less variable and are relatively low (<1.5 Ωm and <1.85 g/cm^3, respectively) at the top of this unit. Resistivity, density, and PEF increase steadily downhole, beginning at slightly different depths (225, 240, and 200 mbsf respectively), whereas total gamma-ray counts remain consistently below 10 API. The frequency and thickness of high-resistivity bands on FMS images decreases markedly below 200 mbsf, and these extreme resistivity contrasts are rare below 290 mbsf. The logging response across the Unit 2/3 boundary is consistent with a reported change from interbedded chert lenses and nodules within chalk above 200 mbsf (Core 165-1001A-23R) to increased disseminated chert within chalk below 200 mbsf. Furthermore, the FMS images indicate that discrete chert lenses are rare below 290 mbsf and that there is increasing resistivity (i.e., increased overall induration) of the sediment with few large contrasts. This FMS response generally corresponds to the lithologic Subunit IIA/IIB boundary at 304 mbsf, which was based, in part, on the lowest occurrence of chert. There is, however, no other significant logging response that corresponds to the lithologic Subunit IIA/IIB boundary.

Two notable anomalies punctuate the overall logging trends of logging Unit 3. An anomaly at approximately 240 mbsf is defined by an absolute maximum in magnetic susceptibility at 239 mbsf, a downhole increase in density that begins at 243 mbsf, and a peak in total gamma-ray counts (15 API) at 241 mbsf. The logging response defining this anomaly is consistent with the recovery of a claystone layer within Core 165-1001A-27R (237–247 mbsf), which marks a decrease in carbonate deposition in the latest Paleocene ("Lithostratigraphy" section, this chapter). Thorium vs. potassium concentrations in the interval from 239 to 254 mbsf fall largely within the illite clay field and indicate a provenance for this clay-rich interval that is distinct from the interval above 167 mbsf (Fig. 64), or possibly a depth-related diagenetic transformation of montmorillonite into illite.

A broad anomaly centered on approximately 345 mbsf is defined by elevated gamma-ray counts (10–20 API) from 336 to 353 mbsf, a distinct increase in the amplitude of variations in resistivity and density data from 336 to 365 mbsf, and an abrupt change in magnetic susceptibility defined by numerous maxima from 328 to 357 mbsf. A broad sinusoidal variation in PEF values, from a wide minimum at 340 mbsf to a maximum at approximately 352 mbsf, is also observed. These overlapping anomalies from different logs span the K/T boundary at approximately 353 mbsf. The gamma-ray anomaly directly above the K/T boundary is primarily due to increased K and Th concentrations (Fig. 63), and reaches a maximum at 347 mbsf, which corresponds to a claystone interval with mixed sedimentary rock in

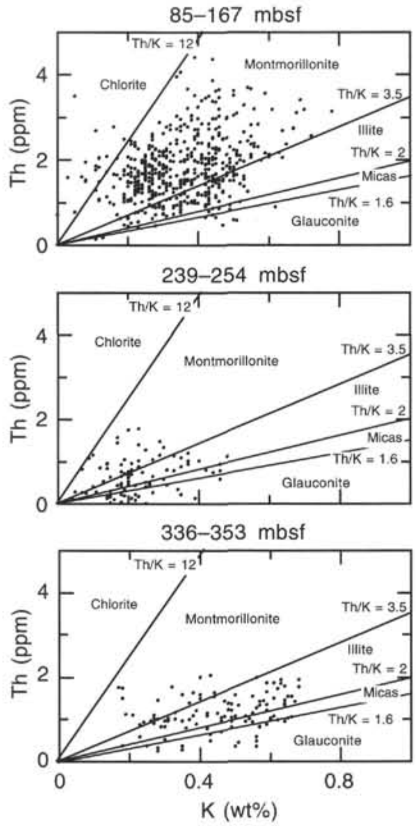

Figure 64. Identification of clay minerals as a function of thorium and potassium concentrations within three different depth intervals in Hole 1001A.

Core 165-1001A-38R (343–353 mbsf) ("Lithostratigraphy" section, this chapter). Thorium vs. potassium concentrations in the interval from 336 to 353 mbsf fall largely within the illite clay field and indicate a greater K content for this claystone than is observed for the uppermost Paleocene clay-rich interval (Fig. 64). Anomalies also extend to Cores 165-1001A-36R and 37R, which contain a peak in number of volcanic ash layers within chalk and are consistent with the increase in amplitude of variation observed on the density, resistivity, and magnetic susceptibility records ("Igneous Petrology and Volcanology" and "Lithostratigraphy" sections, this chapter).

The lithologic Subunit IIB/IIIA boundary is placed just above the K/T boundary and marks the change from calcareous chalk with clay/claystone to calcareous limestone with clay/claystone. The logging response across this lithologic unit boundary indicates that the increase in lithification is gradual; however, there is a change in the frequency and amplitude of variation in the logging data that differentiates the general logging character above and below the K/T boundary (i.e., this change is not just local to the K/T). The FMS record clearly reveals a dramatic decrease in frequency of variation downhole across the K/T boundary, while variations in density and resistivity appear significantly reduced (Fig. 62). The sequence observed on the FMS data was critical for evaluating the completeness of K/T recovery and is discussed in the "Summary and Conclusions" section in this chapter and the "Synthesis" chapter, this volume (Fig. 19, "Synthesis" chapter, this volume). PEF values are relatively elevated (4.5–6 barns/e) from 353 to 416 mbsf and are punctuated by a large isolated minimum in PEF (~2.5 barns/e) at 355 mbsf. This logging response may correspond to the reported increase in carbonate concentration to over 85% and decreased clay content within lithologic Subunit IIIA (i.e., PEF for calcite = 5.08, illite = 3.45, and montmorillonite = 2.04; "Lithostratigraphy" and "Inorganic Geochemistry" sections, this chapter).

Logging Unit 4 (416–470 mbsf)

Logging Unit 4 is characterized by the highest average density (>2.25 g/cm^3) and resistivity (>3 Ωm) values, along with an increase in the frequency and amplitude of variations in these data. There is an unusually large and abrupt decrease in PEF values (4.0 barns/e; Fig. 62) and an increase in frequency and amplitude of isolated maxima in Th concentrations (Fig. 63).

Ash layers, which were essentially absent over a 60-m interval above logging Unit 4, are again present beginning in Core 165-1001A-46R (420–429 mbsf) and increase in frequency and thickness downhole ("Igneous Petrology and Volcanology" section, this chapter). The isolated gamma-ray maximum at 433 mbsf is created by the contribution from an increase in K concentration with one of the numerous Th peaks and corresponds to an 18-cm-thick ash recovered in Core 165-1001A-47R ("Igneous Petrology and Volcanology" section, this chapter). The distinct minimum in resistivity at 458–461 mbsf, along with two closely spaced minima in density and PEF values at 458 and 462 mbsf, appear to correspond to two thick ash layers (18 and 35 cm thick) recovered in Core 165-1001A-50R ("Igneous Petrology and Volcanology" section, this chapter).

Logging Unit 4 lies within lithologic Subunit IIIA, and the logging response marking the Unit 3/4 boundary indicates that there is some change in the composition and physical properties of the sediment. Isolated anomalies are associated with thick ash layers, and the higher variability in the logging data may also be due to an increase in clay and/or foraminifer-rich layers. The abrupt shift to uniformly lower PEF values, along with a generally low gamma-ray count, is more difficult to explain but is consistent with lower carbonate and higher silica content.

Acoustic Velocities

The sonic log from Hole 1001A provided usable velocity data from 85 to 167 mbsf; however, post-cruise processing of the sonic log will be necessary before useful velocity data can be obtained for the remaining section.

Geological High-Sensitivity Magnetic Tool

Total induction and magnetic susceptibility, respectively, were recorded by the scaler magnetometer (NMRS) and the susceptometer (SUMS). A detailed review of these sensors and principles of magnetic logging are provided in the "Explanatory Notes" chapter (this volume). During the time interval that the geological high-sensitivity magnetic tool (GHMT-A) recorded data, the measured total field and susceptibility logs can be affected by time-dependent factors such as transient variations in the Earth's field and temperature drift. A repeat pass of the GHMT-A tool permits analysis of the time-dependent components of the borehole magnetic environment that affect the measurement of magnetization of the surrounding formation. The time-invariant components of the measured field (magnetic mineral concentration and remanent magnetization) can then be examined. Post-cruise data processing will further isolate and quantify both time-dependent and time-invariant factors, and may provide results on the orientation of the paleomagnetic field. We discuss the quality of magnetometer and susceptometer data in the following sections.

Total Induction Log

We removed the contribution of the Earth's magnetic field (Br), using the IGRF value of 39562 nT, from the total field (B) measured by the magnetometer. The remaining "local" field (Fig. 65) for the first run (B1) contains only local effects, that is, $B1(z) = Bf(z) + Ba(z) + Bt1(z,t)$. The second run is very noisy due to problems with the internal electronics of the GHMT tool.

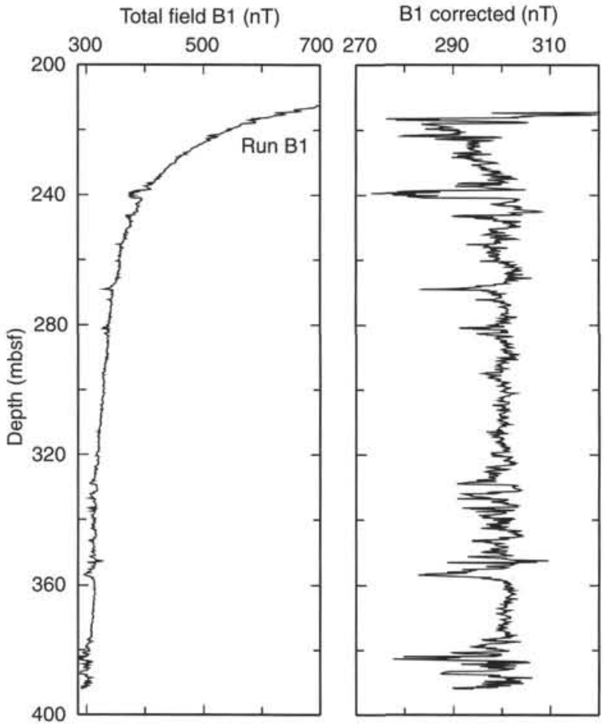

Figure 65. "Local" total magnetic induction for the first run (B1) and the resulting induction after correction for pipe effect (B1 corrected). Part of the total induction has been obtained by correcting the total induction for the main dipolar field.

There is a shift toward high values between 270 and 200 mbsf caused by the highly magnetic bottom-hole assembly (BHA). Apart from sharp positive peaks, the data show little magnetic variation, and the average value of the "local" field B1 is slightly higher than zero. The true value of Bf, the magnetization component of the formation, can be obtained by evaluating the anomaly field Ba and the transient field Bt1.

Analysis of the Components of the Magnetic Induction

Data from the two runs B1 and B2 are quite similar, except for the noisy spikes due to tool problems, and indicate there were no significant temporal changes in the external Earth's field. The remaining "local" B field for the first run, after correction for pipe effect (B1 corrected), is shown in Figure 65. This drill-pipe perturbation can usually be removed, assuming a dipolar effect, and allows for data recovery up to about 10 m beneath the BHA. An overall positive value of the remaining "local" field (B1 corrected) is observed, centered around 300 nT.

Analysis of Susceptibility Records

The magnetic susceptibility data in Hole 1001A appear to be of good quality (Fig. 66). There is a good correlation between the records of the two runs, except for the noisy spikes, indicating there were few measurement errors and little thermal drift of the measurement coils. The susceptibility log, when compared with the magnetic susceptibility measured on cores (see "Physical Properties" section, this chapter) shows a close correlation (Fig. 66). The core measurements are higher frequency because the MST has a higher vertical resolution than the GHMT. The GHMT acquires continuous data on the magnetic susceptibility of the borehole and is particularly important between 200 and 300 mbsf, where core recovery is very low.

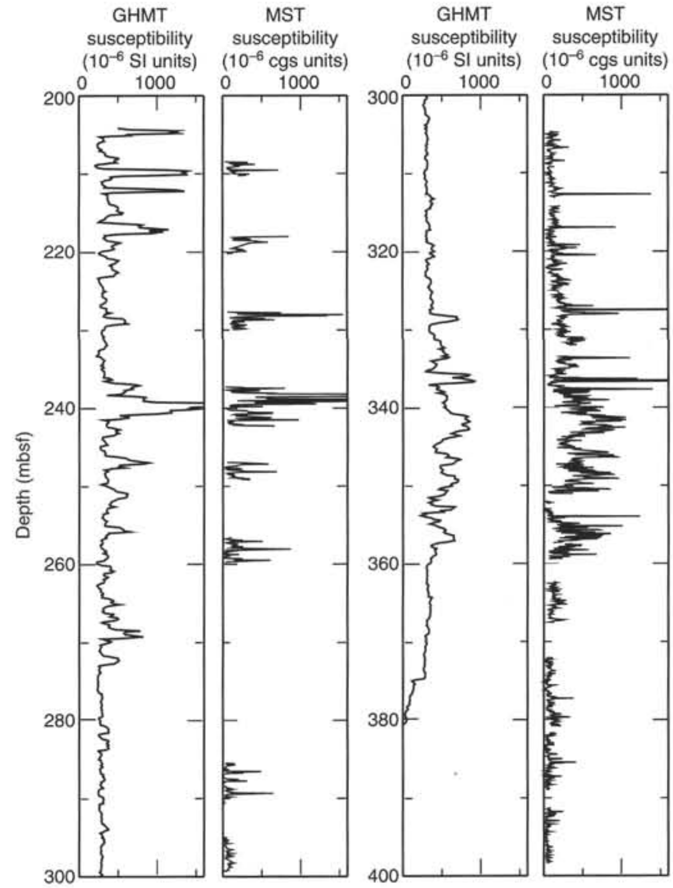

Figure 66. Downhole magnetic susceptibility for the first run for the interval logged by the GHMT (continuous line), and susceptibility measured on cores (discontinuous line) by the MST (see "Physical Properties" section, this chapter).

Comparison of Total Field and Susceptibility Logs

Figure 67 shows the comparison between the "local" B field, obtained from the first magnetometer run (B1 corrected), with the induced magnetization field (Bfi), calculated from the susceptibility recorded during the first run, using the relation:

$$\mathrm{Bfi} = \mathrm{Br} \cdot \mathrm{k} \cdot (1-3 \cdot \sin^2(\mathrm{I}))/2,$$

where k is the susceptibility, and Br and I are the intensity and inclination of the actual Earth's field, respectively. Bfi corresponds to the susceptibility effect on the total field. These two logs show correlations and anticorrelations, which indicate that they may be used to determine polarity reversals with further post-cruise processing.

SUMMARY AND CONCLUSIONS

Drilling at Site 1001 has provided a great variety of new information related to Caribbean paleoceanography, tectonics, and the origin of the Caribbean Oceanic Plateau. A thin Neogene cover made it possible to double-core the Paleogene and Upper Cretaceous sedimentary sequence, thus meeting our high-priority K/T boundary and ancient ocean objectives, and to recover the underlying igneous basement (Fig. 68). Priority was given to the older part of the record at this site. Due to time constraints, we spudded in with the RCB with the aim of successfully coring through an interval of lower Eocene cherts

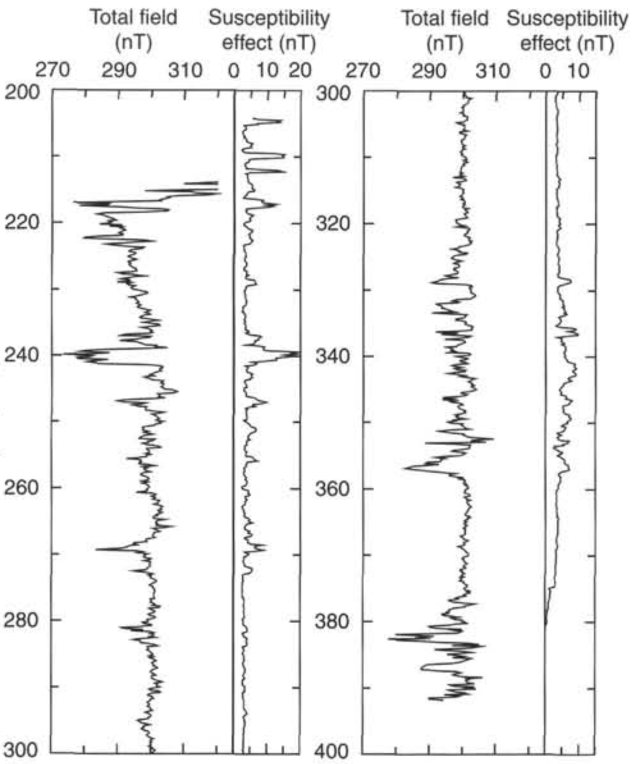

Figure 67. "Local" total induction after correction for pipe effect (B1 corrected) and downhole induction caused by the susceptibility (susceptibility effect; Bfi). Correlations and anti-correlations of these logs indicate that magnetostratigraphy may be determined with further post-cruise processing.

(seismic reflector A″), known to be present at about 160–170 mbsf, from previous coring at DSDP Site 152 some 40 km to the east-northeast.

Stratigraphy

The Neogene section in Hole 1001A is 165.7 m thick and contains a 13.5-m.y. record of sedimentation. Poor recovery prevents us from determining the completeness of this section. The upper Miocene–Pleistocene section consists of clayey nannofossil ooze and nannofossil ooze deposited at an average sedimentation rate of 14.4 m/m.y. (bulk mass accumulation rate of 1.3–1.5 g/cm^2/k.y. through the Pliocene–Pleistocene and 1.5–1.8 g/cm^2/k.y. through the upper Miocene). The middle Miocene/upper Miocene boundary interval accumulated at about 6.8 m/m.y. (0.7–0.9 g/cm^2/k.y.) and consists primarily of nannofossil ooze with clay and nannofossil clay. This latter interval can be correlated with the carbonate crash observed at Sites 998, 999, and 1000. A marked decrease in carbonate and sharp increase in magnetic susceptibility and noncarbonate MAR characterizes the carbonate crash interval (approximately 130–154 mbsf). The duration of decreased carbonate accumulation appears to be longer at Site 1001 than at the sites cored earlier during Leg 165. In detail, the carbonate crash is actually a series of sharp declines in carbonate content (and peaks in susceptibility) with intervening intervals having more typical background carbonate contents. What makes the record at Site 1001 so different is the occurrence of the last of these "mini-carbonate crashes" about 1 m.y. after they had stopped at the other Leg 165 sites.

An unconformity marks the boundary between the Neogene and the Paleogene at Site 1001. Middle Miocene greenish gray nannofossil ooze with clay (nannofossil Zone CN5, planktonic foraminifer Zone N11) rests unconformably on middle Eocene bluish white chalk (nannofossil Subzone CP13c) in Sample 165-1001A-18R-4, 88 cm (165.68 mbsf). The duration of the hiatus is approximately 30 m.y. The middle Eocene chalk is only 28 cm thick. A chert layer marks a lower unconformity (duration 8 m.y.), which is the contact between the middle Eocene section and lower Eocene light greenish gray chalk (nannofossil Zone CP10, planktonic foraminifer Zone P6).

The Paleocene–lower Eocene interval is represented by 186.4 m of section, much of which was double cored (Fig. 68). The dominant lithology is calcareous chalk, but the lower Eocene and upper Paleocene chalk is interbedded with many chert and volcanic ash layers. Sedimentation rates averaged nearly 19 m/m.y., and bulk MARs were highly variable (2.4–4.4 g/cm^2/k.y.). Core recovery through this interval was generally low, probably due to chert. Despite problems with core recovery, a 56- to 75-cm-thick interval of uppermost Paleocene mixed sedimentary rock with clay and claystone was successfully recovered twice (Samples 165-1001A-27R-2, 0–56 cm, and 165-1001B-6R-3, 0–75 cm). This interval was also recovered at Site 999 and is characterized by reduced carbonate content, high magnetic susceptibility, poorly developed lamination, and multiple volcanic ash layers. Preliminary biostratigraphy suggests that this interval correlates with the widespread oceanographic changes associated with the LPTM (Zachos et al., 1993).

The lower Paleocene and lower upper Paleocene is calcareous chalk with clay to claystone and is interbedded with foraminifer-rich sand layers and some volcanic ash layers. These sandy foraminifer-rich layers are interpreted to be the result of winnowing by active bottom traction currents. Core recovery increased significantly in this chert-free and more clay-rich interval. However, this part of the Paleocene accumulated at much lower rates (4.4 m/m.y. or about 0.7–0.8 g/cm^2/k.y. A very similar pattern of low sedimentation and bulk MARs was also observed in the lower Paleocene of Site 999 and elsewhere in the world ocean (e.g., Zachos and Arthur, 1986; D'Hondt et al., in press).

Upper Cretaceous calcareous limestones are 133.3 m thick and accumulated at an average rate of nearly 11 m/m.y. (2.0–2.7 g/cm^2/k.y.). The Maastrichtian and upper Campanian limestones are interbedded with thin claystones and foraminifer-rich sand layers. These features are particularly common throughout the Maastrichtian. The distribution of claystone beds, clearly expressed in downhole logging measurements, may represent an orbitally modulated signal in the sediments (e.g., Herbert and D'Hondt, 1990). Mid-Campanian limestone with clay to clayey mixed sedimentary rock overlies basaltic basement at 485.4 mbsf. This latter interval is characterized by interbedded volcanic ash layers and thick ash turbidites.

Cretaceous/Tertiary Boundary

The K/T boundary was cored in Holes 1001A and 1001B. The boundary was first recovered in the core catcher of Core 165-1001A-38R, at a depth of 352.7 mbsf, but due to extrusion from the core catcher the recovered section is somewhat disturbed. Four loose pieces of the boundary deposit were also recovered in the top of Section 165-1001A-39R-1. Based on the knowledge of the exact depth of the K/T boundary from the coring of Hole 1001A and the downhole FMS log, the boundary deposit was recovered again during drilling of Hole 1001B, entirely within Section 165-1001B-18R-5, at a depth of 352.9 mbsf. This section was not split on board ship to avoid geochemical contamination and protect the integrity of the material. It was split at the Gulf Coast Repository post-cruise, using a non-ferrous ceramic saw blade. The results of shipboard paleomagnetic studies show that the K/T boundary occurs in the upper part of Chron 29R (see "Paleomagnetism" section, this chapter).

The succession of lithologic layers at the K/T boundary in Section 165-1001B-18R-5 is shown in Figure 69 (and Fig. 12, "Synthesis" chapter, this volume). The lithostratigraphy of the boundary in Sec-

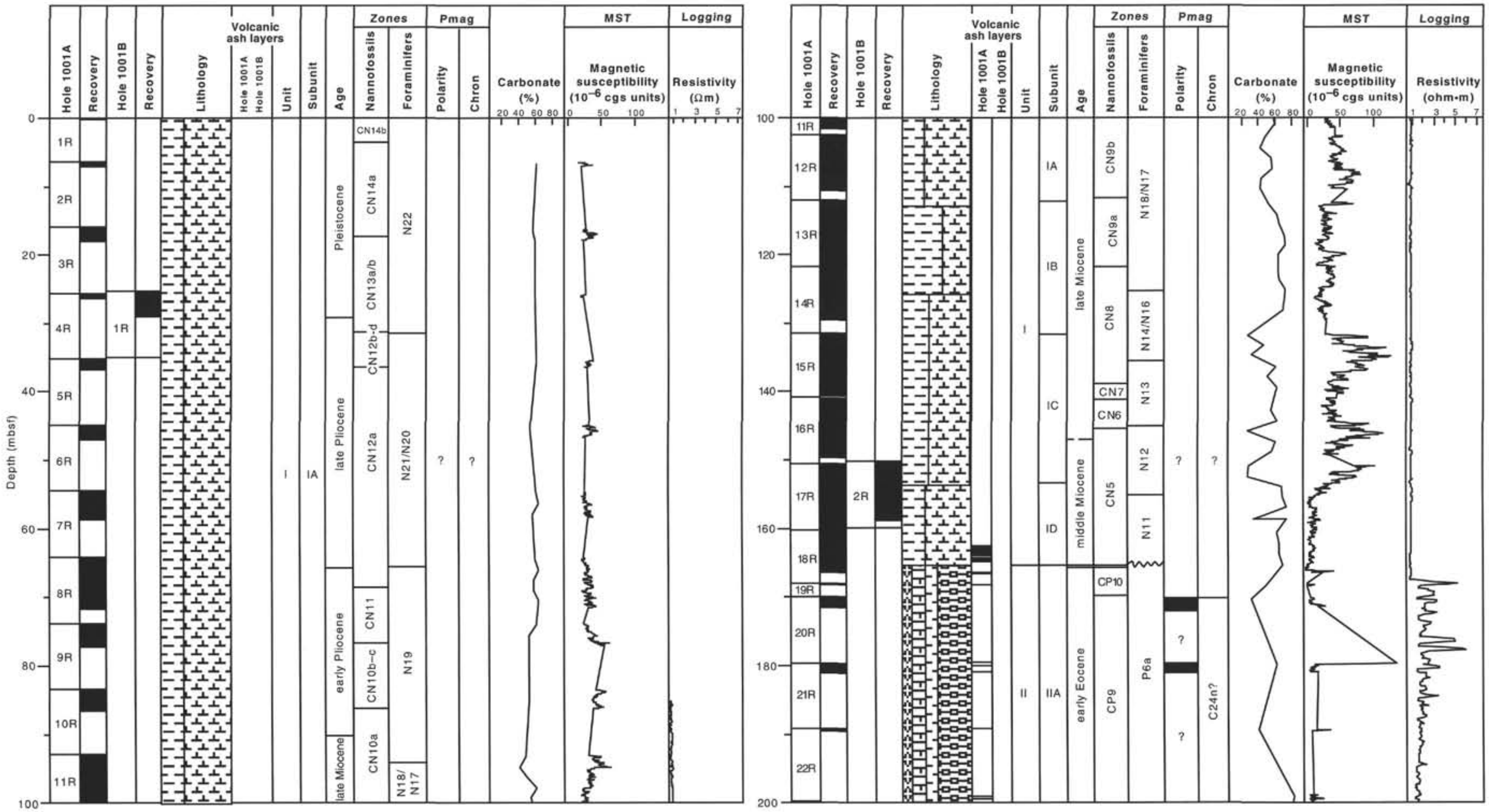

Figure 68. Site 1001 summary column for core recovery, lithology, volcanic ash layer occurrence, lithologic unit and subunit boundaries, ages, nannofossil and foraminiferal datum boundaries, magnetic reversal boundaries, carbonate percentages, MST magnetic susceptibilities, and, for Hole 1001A, *P*-wave velocities from downhole measurements. Horizontal lines in the foraminiferal zonal column show depths of boundaries in Holes 1001A (left) and 1001B (right).

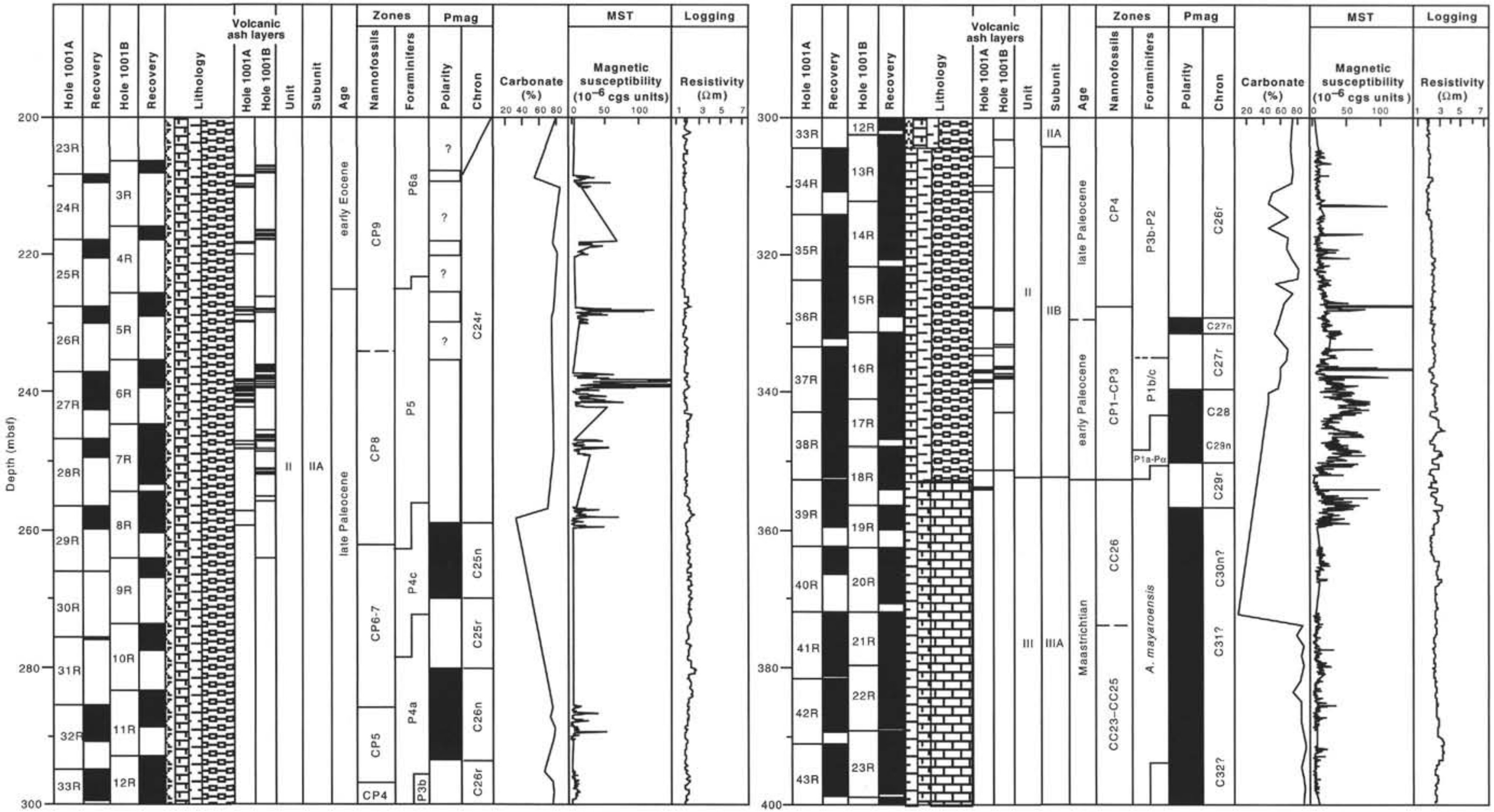

Figure 68 (continued).

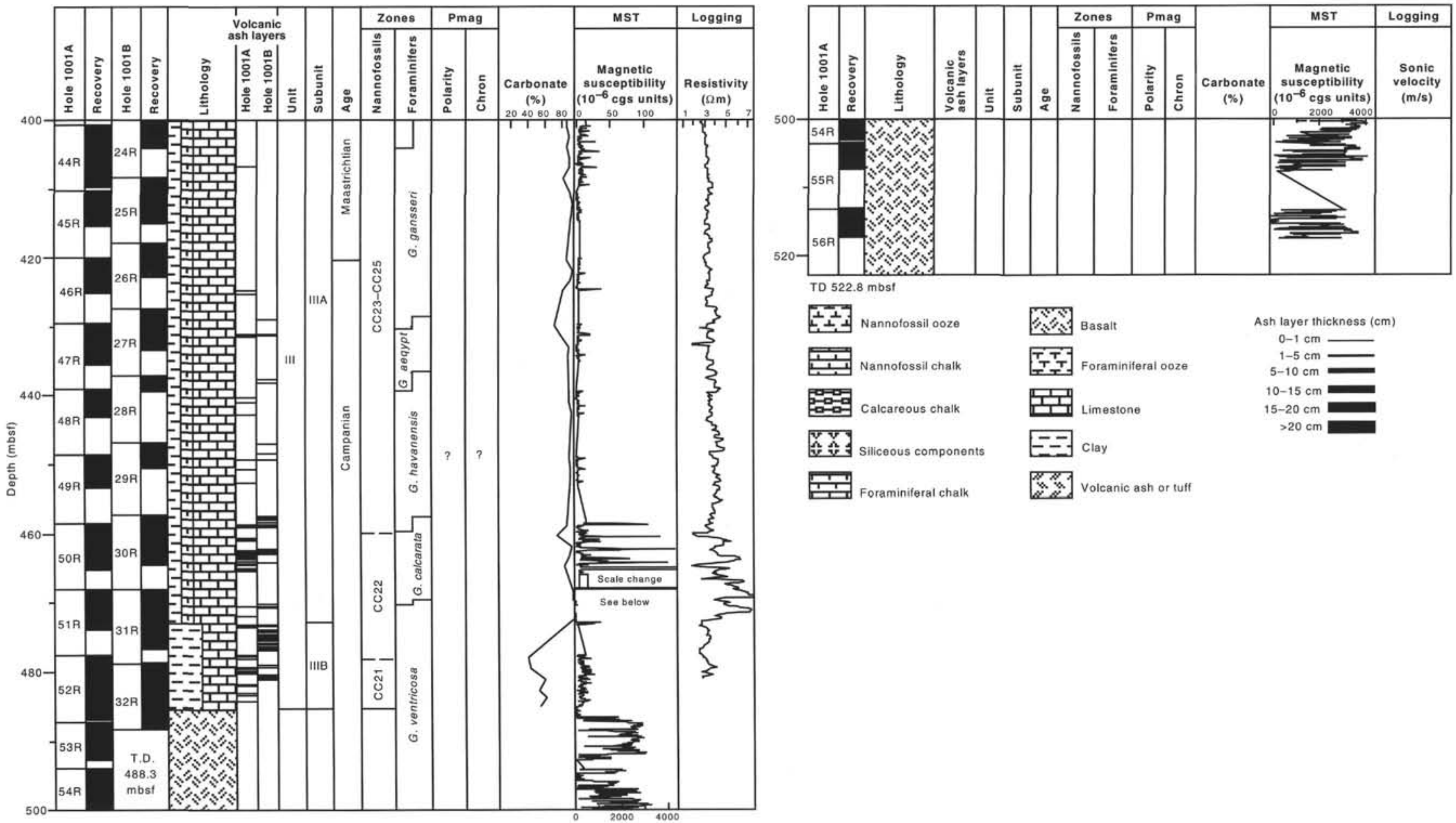

Figure 68 (continued).

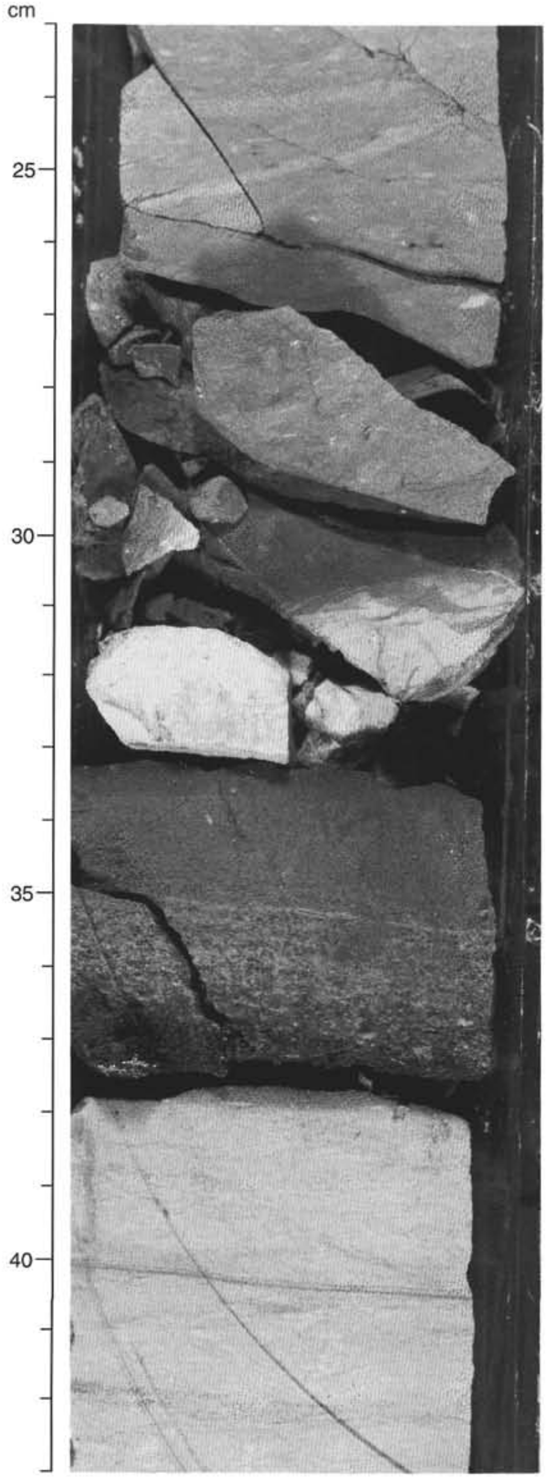

Figure 69. Photograph of the K/T boundary deposit in interval 165-1001B-18R-5, 23–43 cm. The apparent mottling on the surface of the Maastrichtian limestone, and to a lesser extent on the Paleocene clayey limestone, is caused by small loose clasts of tri-octahedral smectite particles that have been eroded from smectite-rich boundary Layers C and D during drilling. See Figure 12 in "Synthesis" chapter (this volume) for details.

tion 165-1001A-38R-CC is shown in Figure 21 (see "Lithostratigraphy" section, this chapter).

In Hole 1001A, the lowermost Paleocene sediments above the K/T boundary are alternating beds of moderately bioturbated and light gray calcareous chalk with thin claystone and mixed sedimentary rock (see "Lithostratigraphy" section, this chapter). The succession in the core catcher of Core 165-1001A-38R includes four lithologic layers that define the boundary interval.

Layer A

At the top is a 4-cm-thick, white to very light gray (5Y 8/1) and highly indurated limestone with a conchoidal fracture, which is closely comparable to the thin and indurated limestone bed on top of the K/T boundary at Site 999. A thin section of this limestone (Sample 165-1001A-38R-CC, 1 cm) shows that it contains planktonic foraminifers of the undifferentiated early Paleocene Zones P0/Pα (see "Biostratigraphy" section, this chapter). This limestone layer was also recovered in Hole 1001B, where it is 1.7 cm thick, with a gradational top and a very sharp base with the claystone below.

Layer B

The Layer A limestone is underlain by a 3.5-cm-thick unit of medium gray to greenish gray (5Y 5/1) claystone, massive and poorly indurated, with a shaly cleavage. The claystone is a mixture of very fine grained carbonate and clay. A smear slide of this layer (Sample 165-1001A-38R-CC, 8 cm) shows that it contains common quartz grains, including several grains of shocked quartz, up to 150 µm in diameter, with multiple sets of planar features (Fig. 70). Microscopic planar deformation features in quartz are micron-thin zones that have a distinctly different refractive index than the host mineral; they are most likely filled with quartz glass or they may contain the high-pressure polymorph stishovite (Stöffler, 1971). Hypervelocity bolide impacts are the only known natural process that can produce these diagnostic shock features, generating pressures on the order of 5–10 GPa. Shocked quartz is also present in the K/T boundary deposit in nearby Haiti, where it also occurs in the uppermost layer, above a thick smectite layer with glass spherules (Hildebrand and Boynton, 1990;

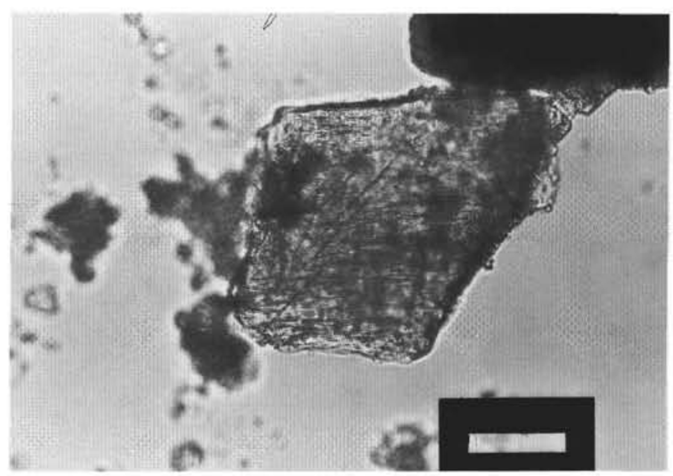

Figure 70. Photomicrograph of a shocked quartz grain from Layer B of the K/T boundary deposit in Hole 1001A (Section 165-1001A-38R-CC). The shocked quartz grain contains the characteristic twin sets of lamellae. Scale bar is 40 µm in length.

Sigurdsson et al., 1991). Layer B contains Cretaceous nannofossils, including rare taxa of Hauterivian to Aptian age (see "Biostratigraphy" section, this chapter).

Layer C

This layer is a greenish gray to bluish green-gray (5G 5/1), massive but mottled claystone to siltstone, 3.5 cm thick, with a greenish matrix and normally graded, small dark green, 1- to 2-mm-diameter smooth spherules. These spherical objects are most likely tektites or impact glasses, which are now largely altered to tri-octahedral smectite. This smectite component composes virtually the entire layer.

Layer D

Layer D is a dark greenish gray (5GY 5/1) shaly claystone, 1 cm thick, with 1- to 2-mm diameter lighter speckles. This unit is texturally similar to, and possibly gradational with Layer C, but it is deformed by drilling. In Hole 1001B this layer is 2 cm thick (Fig. 69; see Fig. 12, "Synthesis" chapter, this volume). In this hole, it is underlain by Layer E, a millimeter-thick layer of brownish gray claystone with shaly parting.

In the top of the core section that directly underlies the K/T boundary (Section 165-1001A-39R-1), there were four loose pieces of smectite-rich sediment recovered that are clearly related to the boundary deposit (Section 165-1001A-39R-1). They are of two types: two pieces consist of a dark greenish gray smectite with dark to black smectite spherules 1 to 2 mm in diameter. This material resembles and probably corresponds to Layer C above. The other two pieces consist of a tan to brown polymict breccia with angular clasts of claystone or limestone up to 6 mm in size, in a highly unconsolidated clayey smectite matrix with dark gray 1–2 mm spherules.

Several lines of evidence indicate that not all of the K/T boundary deposit was recovered during drilling at Site 1001. The recovery of the boundary deposit proper (Layers B to E in Fig. 12, "Synthesis" chapter, this volume) is 8.0 cm in Hole 1001A and 5.2 cm in Hole 1001B. A detailed correlation was made of the magnetic susceptibility between cores from both holes at Site 1001 and with the downcore magnetic susceptibility data of Hole 1001A, as shown in Figure 54 (see "Physical Properties" section, this chapter). This analysis indicates that the gap in recovery between Cores 38R and 39R in Hole 1001A is on the order of 15–20 cm, corresponding to the missing section of K/T boundary ejecta. It is most likely that this missing material is in the lower part of the deposit, as the upper clay-rich part appears to be well preserved and strongly correlated between the two holes (Fig. 69; Fig. 12, "Synthesis" chapter, this volume). Thus, a total inferred thickness of about 25 cm of the K/T boundary deposit at Site 1001 is significantly thinner than the 0.5- to 1-m deposit exposed on Haiti, 350 km to the north-northeast. This is in part due to the greater proximity of Haiti to the Chicxulub crater at the time of impact.

In summary, the K/T boundary deposit recovered at Site 1001 consists of two principal layers. The lower layer (Layers C and D), which may be up to 20 cm thick if the inferred missing section is included, consists of a nearly pure smectite, made up of 1- to 2-mm spherules that most likely represent altered impact glasses (tektites). This is likely ballistic fallout from the Chicxulub impact, and is thus analogous to the basal impact bed observed at the K/T boundary at Beloc in Haiti (Sigurdsson et al., 1991). The upper K/T boundary layer (Layer B) is a 1.7- to 3.5-cm claystone or mixed sediment, composed of fine carbonate and clay. It contains relatively common quartz grains, including quartz with planar deformation features characteristic of hypervelocity impacts. Thus, this layer includes late-stage fallout from the impact, but shore-based studies will reveal whether it also includes the iridium geochemical anomaly.

Igneous Basement

More than 37 m of submarine basaltic lava flows were cored in Hole 1001A, and similarly, the basalt lava/sediment contact and 2 m of a basaltic lava flow were recovered in Hole 1001B. The recovered basement cores reveal a succession of 12 lava flows, which include both pillow lavas and sheet flows, composed of thick hyaloclastite breccia tops and massive columnar basalt interiors. These 2 lava morphologic types may reflect different mass eruption rates, resulting in very different cooling rate history of the advancing lavas on the seafloor. Pillow lavas are most likely the result of eruptions with a lower mass eruption rate and subject to a higher cooling rate, whereas the sheet flows are probably generated by high mass eruption rate events, where the cooling rate is relatively less important. The lavas are interbedded with thin lenses of carbonate sediment with planktonic and benthic foraminifers. Several of the benthic foraminifers may be indicative of neritic environments. The Campanian limestones immediately above the basalts contain a foraminifer assemblage characteristic of an upper bathyal paleoenvironment.

The basalts are remarkably uniform in chemical composition, both in terms of major and trace elements, and show similarities to basalts recovered on DSDP Leg 15 from the Caribbean Oceanic Plateau. The petrographic variations in the basalt succession are very slight, with both aphyric and sparsely plagioclase- and clinopyroxene-phyric types present. Slight downcore variations in both major oxides and trace elements suggest two principal lava types, with an earlier erupted and more Fe- and Mg-enriched basalt, and later activity with basalts higher in alumina and CaO (Fig. 46). Preliminary results on trace element characteristics indicate that these basalts have chemical affinities with a source that may represent a mixture of MORB and plume-derived components (Fig. 49), but shore-based radiogenic isotope studies will be required to fully characterize the nature of their mantle source region.

Volcanic Ash Layers

The sedimentary record from Site 1001 provides evidence for three episodes of explosive volcanism in the Caribbean region. The latest Paleocene–early Eocene episode of silicic tephra fall layers is contemporaneous with explosive volcanic activity observed at Site 998, and attributed to the Cayman Ridge arc (see "Igneous Petrology" section, "Site 998" chapter, this volume). The record of this episode at Site 1001 suggests that it was quite vigorous. A weaker volcanic episode documented at Site 1001 occurred in the early Paleocene, and it may correspond to contemporaneous volcanic ash layers recovered at Site 999 on the Kogi Rise, which we have attributed to early Central American arc eruptions. The third episode recovered at Site 1001 occurred in the mid-Campanian. It includes both andesitic to silicic ash fall layers, as well as a few thick but altered ash turbidites of more basic composition. These turbidites have a limited distribution in the mid-Campanian limestones within 12.5 m of the basaltic basement, and their occurrence may have important implications regarding late-stage volcanic activity on the Caribbean Plateau proximal to Site 1001. The turbidites contain benthic foraminifers of possible mixed neritic and upper bathyal types (see "Biostratigraphy" section, this chapter), which may be derived from relatively shallow-water volcanic edifices on the Caribbean Oceanic Plateau. This evidence suggests rapid subsidence of the plateau following the Campanian emplacement of the underlying basalt lava succession. The short-lived nature of the ash turbidites immediately above the basalt also supports an interpretation of rapid subsidence of the volcanic edifice.

Geochemistry of Pore Waters and Sediments

Although the interior of massive basalt flows is relatively fresh, most of the basalts display moderate alteration. Thus, much of the plagioclase has suffered albitization, and chlorite and zeolites are common, both as infillings in vugs and as replacement in the groundmass. This basalt alteration process and the weathering reactions have had important effects on the chemical composition of pore waters in the overlying sediments, producing a basement signal in the interstitial waters ("Inorganic Geochemistry" section, this chapter). For example, the alteration of calcic plagioclase and highly reactive glass in the basalts and glassy lapilli and breccia units has produced a dramatic gradient in Ca (and Sr) in interstitial waters in the overlying sediments. This is accompanied by decreased alkalinity, due to precipitation of $CaCO_3$ in the basement rocks. The formation of Mg-rich smectite in the altered basalt glass and crystalline rocks has provided a sink for dissolved Mg, reflected in a strong downward trend in Mg in the pore waters. Thus, unlike most of the other sites drilled during Leg 165, the dominant factor on pore-water chemistry at Site 1001 cannot be attributed to the volcanic ashes, but rather to weathering reactions in the basement rocks. However, it is likely that the dissolved silica profile in the interstitial waters, which corresponds closely to the distribution of chert in the sediment, can be attributed to a source from the silicic volcanic ash layers. The source of the Eocene cherts and the prominent seismic reflector A″ that they generate, has long remained an important question in the study of Caribbean geology. The documentation of very widespread and abundant volcanic ash layers throughout the western and central Caribbean, as shown by Leg 165 drilling, lends support to the hypothesis that they play an important role in the distribution of cherts in Caribbean sediments (Mattson and Pessagno, 1971). For example, the presence of the ash may serve to inhibit shallow dissolution of the labile biogenic silica, which subsequently serves as a silica source for the diagenetic chert.

The early work in the region of the Hess Escarpment at DSDP Leg 15, Site 152, showed that the section is dominated by very carbonate-rich sediments (Edgar, Saunders et al., 1973). The sediment geochemistry program carried out at Site 1001 has greatly refined the picture and indicates that at least three sediment sources must be considered. The results show that the terrigenous component decreases dramatically below the Eocene/Miocene unconformity, below which the terrigenous matter becomes significantly less than 10% of the total and is virtually absent in sediments pre-dating the K/T boundary ("Inorganic Geochemistry" section, this chapter). This is consistent with the Caribbean Plate in the eastern Pacific region being relatively remote from continental sources and elevated above the adjacent abyssal plains in the Late Cretaceous and early Paleogene (Duncan and Hargraves, 1984; Pindell and Barrett, 1990). The geochemistry also shows that provenance of the terrigenous component may vary within the post-Eocene sediments, indicating the influence of at least two terrigenous sources on sedimentation at Site 1001. In addition to the carbonate and terrigenous components, the chemical composition of the Site 1001 sediments reveals a third residual component, which represents up to 25%–30% of the sediment in the Paleogene and Upper Cretaceous (Fig. 36). Most of this component is likely related to dispersed volcanic ash, although its downcore distribution does not show a close correlation with the occurrence of megascopic ash layers in the sediments (as also observed to an extent at Site 1000).

Seismic Stratigraphic Correlations

The coring and logging results provide additional constraints for mapping regional seismic reflection packages as illustrated by the correlations between seismic stratigraphy, depths, logging units, lithologic units, and ages at Site 1001 (Fig. 71). The 522.8-m-thick drilled section at Site 1001 corresponds to three main seismic Units A, B, and C; the lower Unit C corresponds to a basaltic basement marked by a prominent reflector (B″), and the upper Units A and B represent a pelagic sedimentary sequence, delimited by another prominent reflector (A″). Velocities above basement are interval velocities derived from two-way traveltimes (TWT) to the two prominent reflectors A″ and B″ and from drilling depths to each of these seismic horizons. Average interval velocity is 1.541 km/s for Unit A and 2.780 for Unit B. In the volcanic basement, the average velocity (4.672 km/s) is based upon laboratory measurements and is used to calculate the total depth at 4.736 s TWT.

The top basement reflector (B″) is characterized by a set of one to two very high amplitude, laterally continuous reflectors. The acoustic basement reflection (B″) at 4.720 s TWT corresponds to the transition from mid-Campanian clayey mixed sedimentary rocks (lithologic Subunit IIIB) to a succession of Campanian (?) submarine basaltic lava flows (lithologic Unit IV) drilled at 485.4 mbsf. Reflector A″, within the sedimentary sequence separating seismic Unit B from the overlying Unit A, is characterized by a clear set of continuous high amplitude reflections. Reflector A″ at 4.490 s TWT corresponds to a pair of unconformities at 165.7 mbsf that marks the lithologic Subunit ID/IIA boundary.

REFERENCES

Aubry, M.-P., 1984. *Handbook of Cenozoic Calcareous Nannoplankton* (Book 1): *Ortholithae (Discoasters):* New York (Micropaleontology Press).

———, 1988. *Handbook of Calcareous Nannoplankton* (Book 2): *Ortholithae (Catinasters, Ceratoliths, Rhabdoliths):* New York (Micropaleontology Press).

———, 1989. *Handbook of Cenozoic Calcareous Nannoplankton* (Book 3): *Ortholithae (Pentaliths and Others). Heliolithae (Fasciculiths, Sphenoliths, and Others):* New York (Micropaleontology Press).

Aubry, M.-P., Berggren, W.A., Kent, D.V., Flynn, J.J., Klitgord, K.D., Obradovich, J.D., and Prothero, D.R., 1988. Paleogene geochronology: an integrated approach. *Paleoceanography,* 3:707–742.

Aubry, M.-P., Berggren, W.A., Stott, L., and Sinha, A., 1996. The upper Paleocene–lower Eocene stratigraphic record and the Paleocene/Eocene boundary carbon isotope excursion: implications for geochronology. *In* Knox, R., Corfield, R., and Dunay, R.E. (Eds.), *Correlation of the Early Paleogene in Northwestern Europe,* Spec. Publ.—Geo. Soc. Am., 101: 353–380.

Backman, J., 1984. Late Paleocene to middle Eocene calcareous nannofossil biochronoly from the Shatsky Rise, Walvis Ridge and Italy. *Palaeogeogr., Palaeoclimatol., Palaeoecol.,* 57:43–59.

Backman, J., and Hermelin, J.O.R., 1986. Morphometry of the Eocene nannofossil *Reticulofenestra umbilicus* lineage and its biochronological consequences. *Palaeogeogr., Palaeoclimatol., Palaeoecol.,* 57:103–116.

Bralower, T.J., and Mutterlose, J., 1995. Calcareous nannofossil biostratigraphy of Site 865, Allison Guyot, Central Pacific Ocean: a tropical Paleogene reference section. *In* Winterer, E.L., Sager, W.W., Firth, J.V., and Sinton, J.M. (Eds.), *Proc. ODP, Sci. Results,* 143: College Station, TX (Ocean Drilling Program), 31–74.

Bralower, T.J., and Siesser, W.G., 1992. Cretaceous calcareous nannofossil biostratigraphy of Sites 761, 762, and 763, Exmouth and Wombat Plateaus, northwest Australia. *In* von Rad, U., Haq, B.U., et al., *Proc. ODP, Sci. Results,* 122: College Station, TX (Ocean Drilling Program), 529–556.

Burke, K., 1988. Tectonic evolution of the Caribbean. *Annu. Rev. Earth Planet. Sci.,* 16:201–230.

Burke, K., Cooper, C., Dewey, J.F., Mann, P., and Pindell, J.L., 1984. Caribbean tectonics and relative plate motions. *In* Bonini, W.E., Hargraves, R.B., and Shagram, R. (Eds.), *The Caribbean-South American Plate Boundary and Regional Tectonics,* Mem.—Geol. Soc. Am., 162:31–63.

Case, J.E., Shagam, R., and Giegengack, R.F., 1990. The geology of the northern Andes: an overview. *In* Dengo, G., and Case, J.E. (Eds.), *The Caribbean Region.* Geol. Soc. Am., Geol. of North Am. Ser., H:177–200.

Case, J.E. and Holcombe, T.L., 1977. Generalized tectonic map of the Caribbean. *Eng. Mining J.,* 178:49–51.

D'Hondt, S., Herbert, T., King, J., and Gibson, C., in press. Planktic foraminifera, asteroids, and marine production: death and recovery at the Cretaceous/Tertiary boundary. *In* Ryder, G.T., Fastovsky, D.E., and Gartner, S. (Eds.), *New Developments Regarding the K/T Event and Other Catastrophes in Earth History.* Spec. Pap.—Geol. Soc. Am., 307.

Diebold, J.B., Driscoll, N., Abrams, L., Buhl, P., Donnelly, T., Laine, E., and Leroy, S., 1995. A regional geophysical survey of the Venezuelan Basin and Beata Ridge: implications for the interpretations of stratigraphy and tectonics. *Eos,* 76:614.

Donnelly, T.W., Melson, W., Kay, R., Rogers, J.J.W., 1973. Basalts and dolerites of Late Cretaceous age from the central Caribbean. *In* Edgar, N.T., Saunders, J.B., et al., *Init. Repts. DSDP,* 15: Washington (U.S. Govt. Printing Office), 989–1011.

Donnelly, T.W., Beets, D., Carr, M.J., Jackson, T., Klaver, G., Lewis, J., Maury, R., Schellenkens, H., Smith, A.L., Wadge, G., and Westercamp, D., 1990. History and tectonic setting of Caribbean magmatism. *In* Dengo, G., and Case, J.E. (Eds.), *The Caribbean Region.* Geol. Soc. Am., Geol. of North Am. Ser., H:339–374.

Draper, G., 1986. Blueschists and associated rocks in eastern Jamaica and their significance for Cretaceous plate margin development in the northern Caribbean. *Geol. Soc. Am. Bull,* 97:48–60.

Droxler, A.W., 1995. *Caribbean Drilling Program; R/V Maurice Ewing Site Survey Preliminary Report,* ODP Data Bank (Lamont-Doherty Earth Observatory, Columbia University).

Droxler, A.W., Cunningham, A., Hine, A.C., Hallock, P., Duncan, D., Rosencrantz, E., Buffler, R., and Robinson, E., 1992. Late middle(?) Miocene segmentation of an Eocene–early Miocene carbonate megabank on the northern Nicaragua Rise tied to the tectonic activity at the North America/Caribbean plate boundary zone. *Eos,* (Suppl. 43), 73:299. (Abstract)

Droxler, A.W., Cunningham, A.D., Mucciarone, D., and Rosencrantz, E., 1995. Imaging the Hess Escarpment by Hydrosweep, high-resolution seismic, and magnetism, northeast Columbian Basin, Caribbean Sea. *Geol. Soc. Am. Abstr. Prog.,* New Orleans. (Abstract)

Duncan, R.A., and Hargraves, R.B., 1984. Plate tectonic evolution of the Caribbean region in the mantle reference frame. *In* Bonini, W.E., Hargraves, R.B., and Shagam, R. (Eds.), *The Caribbean-South American Plate Boundary and Regional Tectonics.* Mem.—Geol. Soc. Am., 162:81–94.

Edgar, N.T., Ewing, J.I., and Hennion, J., 1971. Seismic refraction and reflection in the Caribbean Sea. *Am. Assoc. Petrol. Geol. Bull.,* 55:833–870.

Edgar, N.T., Saunders, J.B., et al., 1973. *Init. Repts. DSDP,* 15: Washington (U.S. Govt. Printing Office).

Engell-Jensen, M., Korsbech, U., and Madsen, F.E., 1984. U, Th and K in Upper Cretaceous and Tertiary sediments in Denmark. *Bull. Geol. Soc. Den.,* 32:107–120.

Erba, E., Premoli Silva, I., and Watkins, D.K., 1995. Cretaceous calcareous plankton biostratigraphy of Sites 872 to 879. *In* Haggerty, J.A., Premoli Silva, I., Rack, F., and McNutt, M.K. (Eds.), *Proc. ODP, Sci. Results,* 144: College Station, TX (Ocean Drilling Program), 157–169.

Ewing, J., Antoine, J., and Ewing, M., 1960. Geophysical measurements in the western Caribbean Sea and in the Gulf of Mexico. *J. Geophys. Res.,* 65:4087–4126.

Ewing, J., Talwani, M., and Ewing, M., 1968. Sediments of the Caribbean. *Proc. Int. Conf. Trop. Oceanogr.,* Univ. of Miami, 5:88–102.

Fisher, R.V., and Schmincke, H.-U., 1984. *Pyroclastic Rocks:* New York (Springer-Verlag).

Froelich, P.N., Klinkhammer, G.P., Bender, M.L., Luedtke, N.A., Heath, G.R., Cullen, D., Dauphin, P., Hammond, D., Hartman, B., and Maynard, V., 1979. Early oxidation of organic matter in pelagic sediments of the eastern equatorial Atlantic: suboxic diagenesis. *Geochim. Cosmochim. Acta,* 43:1075–1090.

Herbert, T.D., and D'Hondt, S.L., 1990. Precessional climate cyclicity in Late Cretaceous-early Tertiary marine sediments: a high resolution chronometer of Cretaceous-Tertiary boundary events. *Earth Planet. Sci. Lett.,* 99:263–275.

Hildebrand, A.R., and Boynton, W.V., 1990. Proximal Cretaceous–Tertiary boundary impact deposits in the Caribbean. *Science,* 248:843–847.

Holcombe, T.L., Ladd, J.W., Westbrook, G., Edgar, N.T., and Bowland, C.L., 1990. Caribbean marine geology: ridges and basins of the plate interior. *In* Dengo, G., and Case, J.E. (Eds.), *The Caribbean Region.* Geol. Soc. Am., Geol. of North Am. Ser., H:231–260.

Lewis, J.F., and Draper, G., 1990. Geology and tectonic evolution of the northern Caribbean margin. *In* Dengo, G., and Case, J.E. (Eds.), *The Caribbean Region.* Geol. Soc. Am., Geol. of North Am. Ser., H:77–140.

Lyle, M., Dadey, K.A., and Farrell, J.W., 1995. The late Miocene (11–8 Ma) eastern Pacific carbonate crash: evidence for reorganization of deep-water circulation by the closure of the Panama Gateway. *In* Pisias, N.G., Mayer, L.A., Janecek, T.R., Palmer-Julson, A., and van Andel, T.H. (Eds.), *Proc. ODP, Sci. Results,* 138: College Station, TX (Ocean Drilling Program), 821–838.

Martens, C.S., and Berner, R.A., 1974. Methane production in the interstitial waters of sulfate-depleted marine sediments. *Science,* 185:1167–1169.

Mattson, P.H., and E.A. Pessagno, 1971: Caribbean Eocene volcanism and the extent of horizon A. *Science,* 174:138–139.

Millero, F.J., and Sohn, M.L., 1992. *Chemical Oceanography:* Boca Raton (CRC Press).

Okada, H., and Bukry, D., 1980. Supplementary modification and introduction of code numbers to the low-latitude coccolith biostratigraphic zonation (Bukry, 1973; 1975). *Mar. Micropaleontol.,* 5:321–325.

Pearce, J.A., 1982. Trace element characteristics of lavas from destructive plate boundaries. *In* Thorpe, R.S. (Ed.), *Andesites: Orogenic Andesites and Related Rocks:* New York (Wiley), 525–548.

Perch-Nielsen, K., 1985. Cenozoic calcareous nannofossils. *In* Bolli, H.M., Saunders, J.B., and Perch-Nielsen, K. (Eds.), *Plankton Stratigraphy:* Cambridge (Cambridge Univ. Press), 427–554.

Pindell, J.L., and Barrett, S.F., 1990. Geologic evolution of the Caribbean region: a plate-tectonic perspective. *In* Dengo, G., and Case, J.E. (Eds.), *The Caribbean Region.* Geol. Soc. Am., Geol. North. Am. Ser., H:405–432.

Premoli Silva, I., and Bolli, H.M., 1973. Late Cretaceous to Eocene foraminifera and stratigraphy of the Leg 15 sites in the Caribbean Sea. *In* Edgar, N.T., Saunders, J.B., et al., *Init. Repts. DSDP,* 15: Washington (U.S. Govt. Printing Office), 499–547.

Riedel, W.R., and Sanfilippo, A., 1973. Cenozoic Radiolaria from the Caribbean, Deep Sea Drilling Project, Leg 15. *In* Edgar, N.T., Saunders, J.B., et al., *Init. Repts. DSDP,* 15: Washington (U.S. Govt. Printing Office), 705–751.

Robaszynski, F., Caron, M., Gonzales-Donoso, J.-M., Wonders, A.A.H., and the European Working Group on Planktonic Foraminifera, 1984. Atlas of Late Cretaceous globotruncanids. *Rev. Micropaleontol.,* 26:145–305.

Sandwell, D.T., Yale, M.M., and Smith, W.H.F., 1994. ERS-1: Geodetic mission reveals detailed tectonic structures. *Transactions,* Am. Geophys. Union (Fall Meeting Abst. Suppl.), 75:155. (Abstract)

Sato, T., Kameo, K., and Takayama, T., 1991. Coccolith biostratigraphy of the Arabian Sea. *In* Prell, W.L., Niitsuma, N., et al., *Proc. ODP, Sci. Results,* 117: College Station, TX (Ocean Drilling Program), 37–54.

Schmincke, H.-U., and von Rad, U., 1979. Neogene evolution of Canary Island volcanism inferred from ash layers and volcaniclastic sandstones of DSDP Site 397 (Leg 47A). *In* von Rad, U., Ryan, W.B.F., et al., *Init. Repts. DSDP,* 47 (Pt. 1): Washington (U.S. Govt. Printing Office), 703–725.

Sen, G.R., Hickey-Vargas, R., Waggoner G., and Maurasse F., 1988. Geochemistry of basalts from the Dumisseau Formation, southern Haiti: implications for the origin of the Caribbean Sea crust. *Earth Planet. Sci. Lett.,* 87:423–437.

Shipboard Scientific Party, 1995. Site 953. *In* Schmincke, H.-U., Weaver, P., Firth, J.V., et al., *Proc. ODP, Init. Repts.,* 157: College Station, TX (Ocean Drilling Program), 317–394.

Sigurdsson, H., D'Hondt, S., Arthur, M.A., Bralower, T.J., Zachos, J.C., Fossen, M., and Channell, J.E.T., 1991. Glass from the Cretaceous–Tertiary boundary in Haiti. *Nature,* 349:482–487.

Sigurdsson, H. and Loebner, B., 1981. Deep-sea record of Cenozoic explosive volcanism in the North Atlantic. *In* Self, S. and Sparks, R.S.J. (Eds.), *Tephra Studies:* London (Reidel), 289–316.

Sissingh, W., 1977. Biostratigraphy of Cretaceous calcareous nannoplankton. *Geol. Mijnbouw,* 56:37–65.

Speed, R.C., 1987. *Caribbean Geological Evolution.* JOI-USSAC Report. Workshop on Caribbean Drilling, Jamaica.

Stöffler, D., 1971. Coesite and stishovite in shocked crystalline rocks. *J. Geophys. Res.,* 76:5474–5488.

Takayama, T., and Sato, T., 1987. Coccolith biostratigraphy of the North Atlantic Ocean, Deep Sea Drilling Project Leg 94. *In* Ruddiman, W.F., Kidd, R.B., Thomas, E., et al., *Init. Repts. DSDP,* 94 (Pt. 2): Washington (U.S. Govt. Printing Office), 651–702.

Taylor, S.R., and McLennan, S.M., 1985. *The Continental Crust: Its Composition and Evolution:* Oxford (Blackwell Scientific).

Urmos, J., Wilkens, R.H., Bassinot, F., Lyle, M., Marsters, J.C., Mayer, L.A., and Mosher, D.C., 1993. Laboratory and well-log velocity and density measurements from the Ontong Java Plateau: new in-situ corrections to laboratory data for pelagic carbonates. *In* Berger, W.H., Kroenke, L.W., Mayer, L.A., et al., *Proc. ODP, Sci. Results,* 130: College Station, TX (Ocean Drilling Program), 607–622.

Wilson, J.T., 1966. Are the structures of the Carribean and Scotia arc regions analogous to ice rafting? *Earth and Planet. Sci. Lett.,* 1:335–338.

Zachos, J.C., and Arthur, M.A., 1986. Paleoceanography of the Cretaceous/Tertiary boundary event: inferences from stable isotopic and other data. *Paleoceanography,* 1:5–26.

Zachos, J.C., Lohmann, K.C., Walker, J.C.G., and Wise, S.W., Jr., 1993. Abrupt climate change and transient climates during the Paleogene: a marine perspective. *J. Geol.,* 101:191–213.

Ms 165IR-106

NOTE: Core-description forms ("barrel sheets") and core photographs can be found in Section 4, beginning on page 403. Forms containing smear-slide data can be found in Section 5, beginning on page 821. Thin-section descriptions are given in Sections 6 and 7, beginning on page 851. See Table of Contents for material contained on CD-ROM.

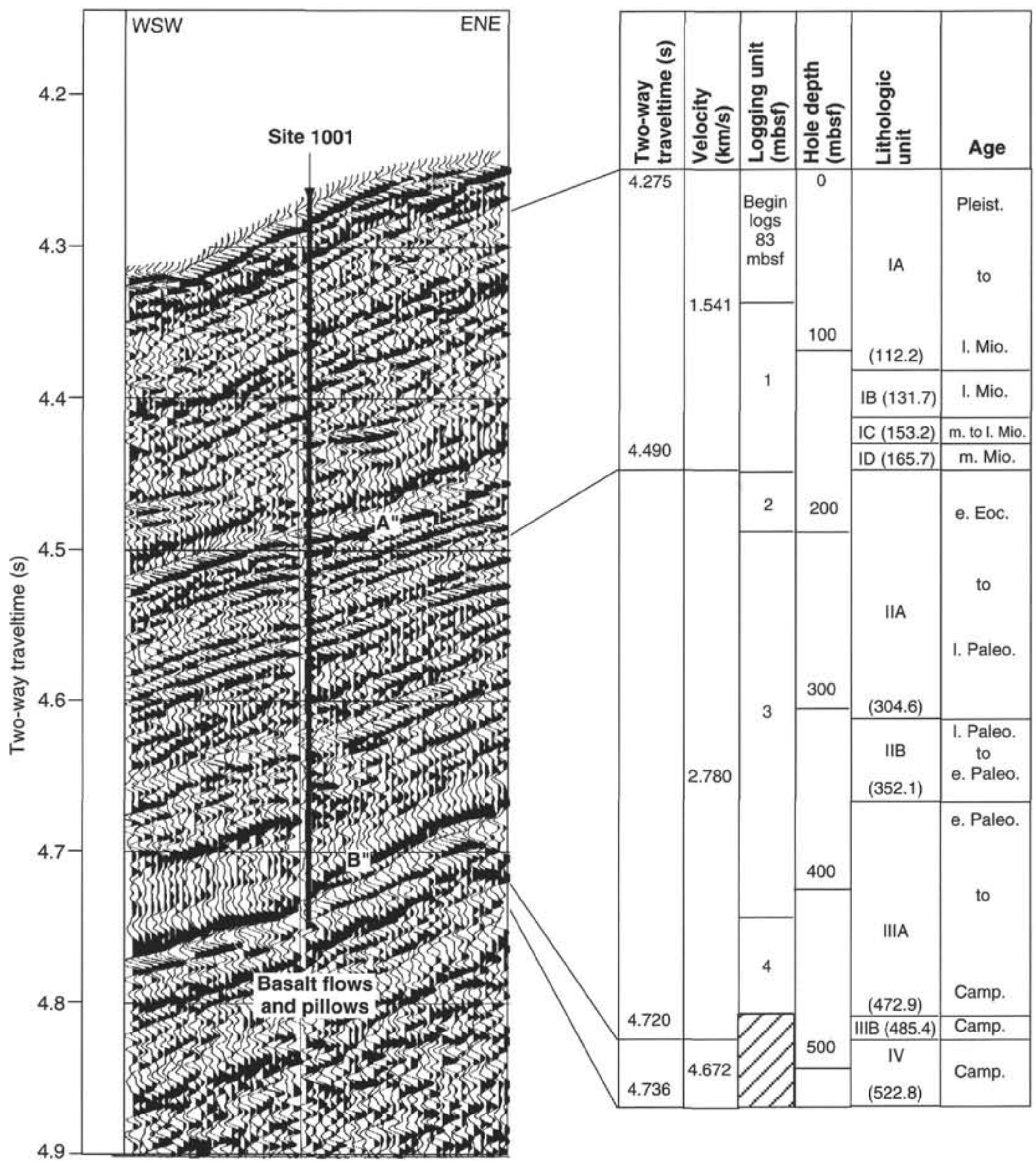

Figure 71. Summary of correlations between seismic stratigraphy, depths, logging units, lithologic units, and ages at Site 1001. Velocities above basement are interval velocities derived from two-way traveltimes to the two prominent reflectors (A″ and B″) and from drilling depths to each of these seismic horizons. In lithologic Unit IV (volcanic basement), the average velocity from laboratory measurements is given (4.672 km/s) and is used to calculate total depth at 4.736 s TWT. An approximately 2-km portion of EW9417 SCS Line 10 is displayed with a vertical exaggeration of 10× (see "Underway Geophysics and Pre-Site Survey" section, "Explanatory Notes" chapter, this volume, for seismic processing and display parameters; see also "Seismic Stratigraphy" section, this chapter).

SHORE-BASED LOG PROCESSING
HOLE 1001A

Bottom felt: 3271 mbrf (used for depth shift to seafloor)
Total penetration: 522.8 mbsf
Total core recovered: 286.2 m (54.8%)

Logging Runs

Logging string 1: DIT/SDT/HLDT/CNTG/NGT
Logging string 2: FMS/GPIT/NGT (main and repeat)
Logging string 3: GHMT/NGT (2 lower sections and 1 upper section)
Wireline heave compensator was used to counter ship heave.

Bottom-Hole Assembly

The following bottom-hole assembly depths are as they appear on the logs after differential depth shift (see "Depth shift" section) and depth shift to the seafloor. As such, there might be a discrepancy with the original depths given by the drillers on board. Possible reasons for depth discrepancies are ship heave, use of wireline heave compensator, and drill string and/or wireline stretch.

DIT/SDT/HLDT/CNTG/NGT: Bottom-hole assembly at ~82 mbsf
FMS/GPIT/NGT: Did not reach bottom-hole assembly
GHMT/NGT: Pipe at ~ 82 mbsf

Processing

Depth shift: Original logs have been interactively depth shifted with reference to NGT from the DIT/SDT/HLDT/CNTG/NGT run and to the seafloor (−3271 m).

Gamma-ray processing: Data have been processed to correct for borehole size and type of drilling fluid.

Acoustic data processing: The array sonic tool was operated in standard depth-derived, borehole compensated, long spacing (8–10 and 10–12 ft) mode. The original sonic log is of good quality in the upper part of the hole, down to about 167 mbsf. In the lower part of the hole, only the 8-ft spacing channel shows reasonable values, only locally affected by cycle skipping. This transit time has been edited and used to calculate compressional velocity. The computed velocity shows very good correlation with the resistivity logs and is therefore considered of good quality.

Quality Control

The density data show a few spikes (121–124, 148, and 220 mbsf) caused by instability of the long spacing detector, possibly due to borehole conditions.

Data recorded through the bottom-hole assembly, such as the gamma-ray data above 82 mbsf, should be used qualitatively only because of attenuation on the incoming signal. Invalid gamma-ray spikes were recorded at 82–87 mbsf during the DIT/SDT/HLDT/CNTG/NGT run.

Hole diameter was recorded by the hydraulic caliper on the HLDT tool (CALI), and the caliper on the FMS string (C1 and C2).

Details of standard shore-based processing procedures are found in the "Explanatory Notes" chapter (this volume). For further information about the logs, please contact:

Cristina Broglia
Phone: 914-365-8343
Fax: 914-365-3182
E-mail: chris@ldeo.columbia.edu

Zhiping Tu
Phone: 914-365-8336
Fax: 914-365-3182
E-mail: ztu@ldeo.columbia.edu

Hole 1001A: Natural Gamma Ray-Density-Porosity Logging Data

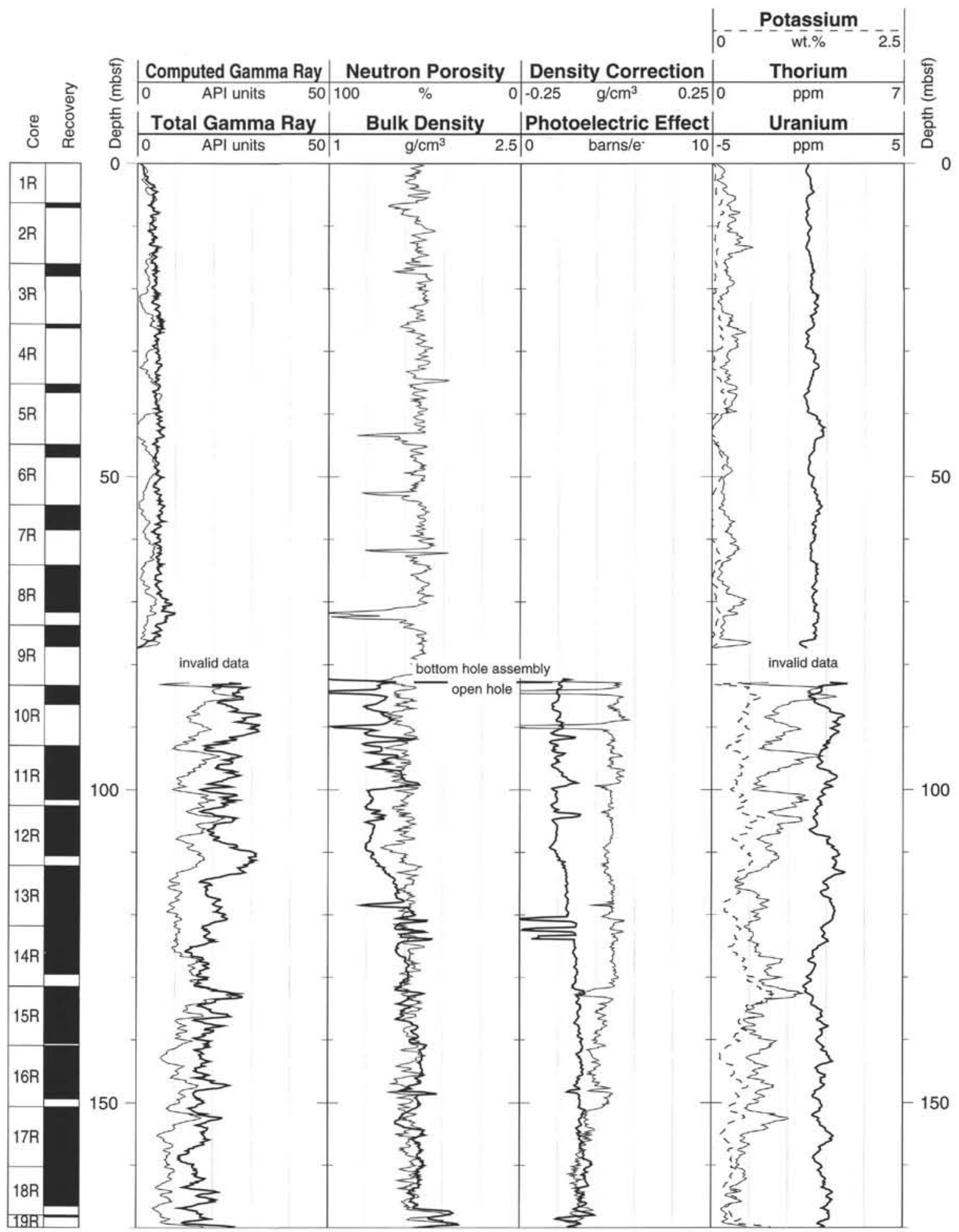

Hole 1001A: Natural Gamma Ray-Density-Porosity Logging Data (cont.)

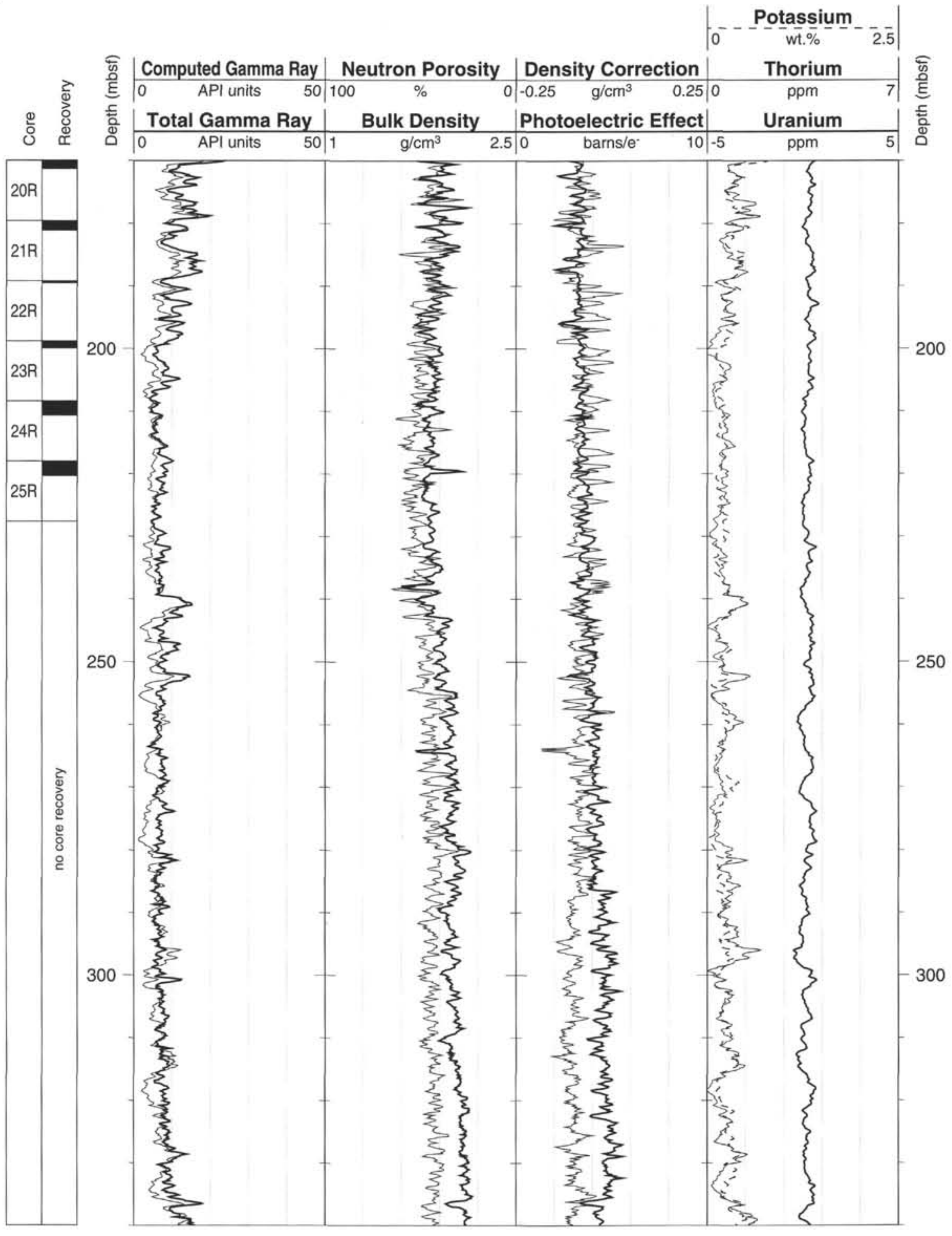

Hole 1001A: Natural Gamma Ray-Density-Porosity Logging Data (cont.)

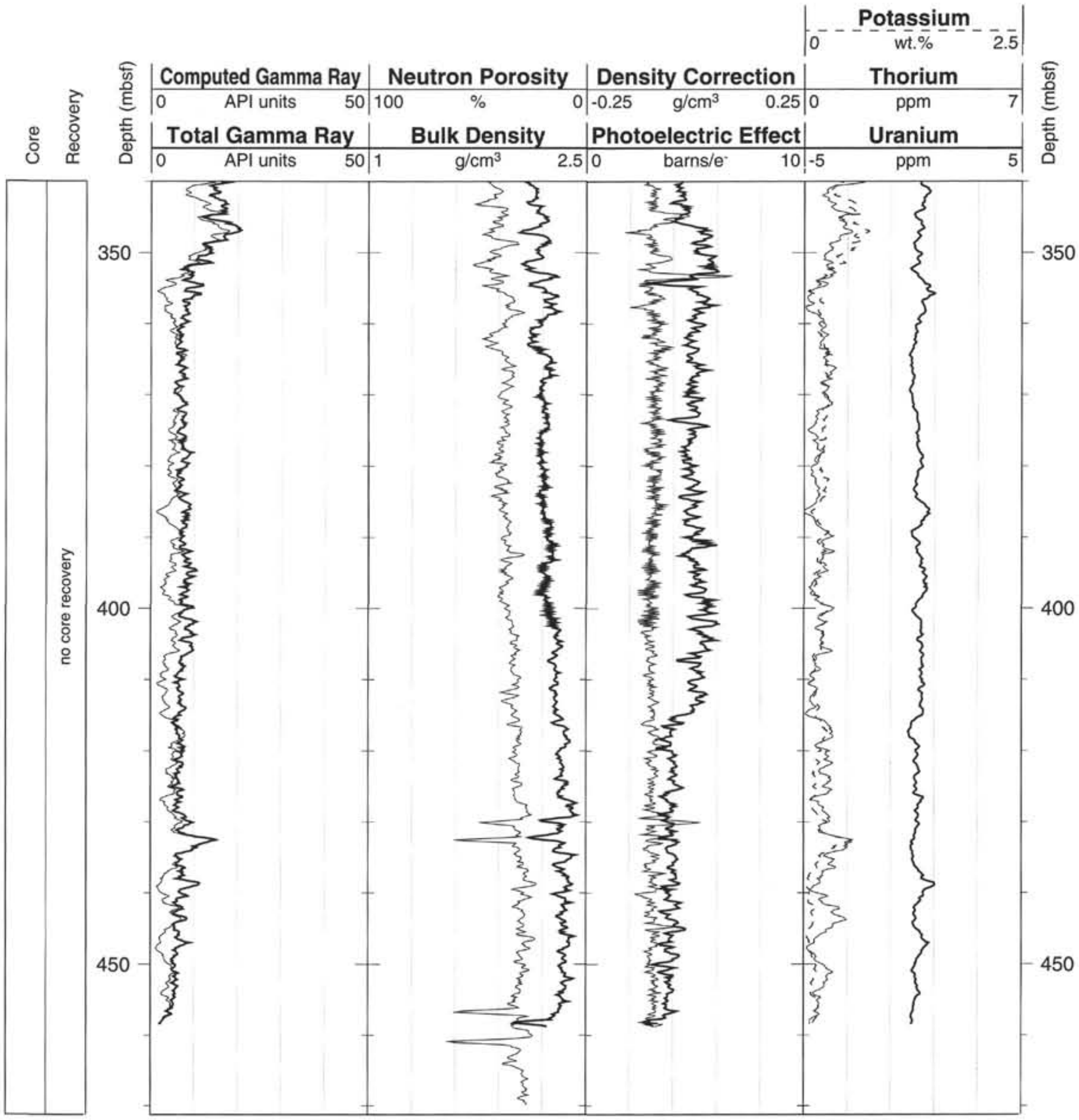

Hole 1001A: Natural Gamma Ray-Resistivity-Sonic Logging Data

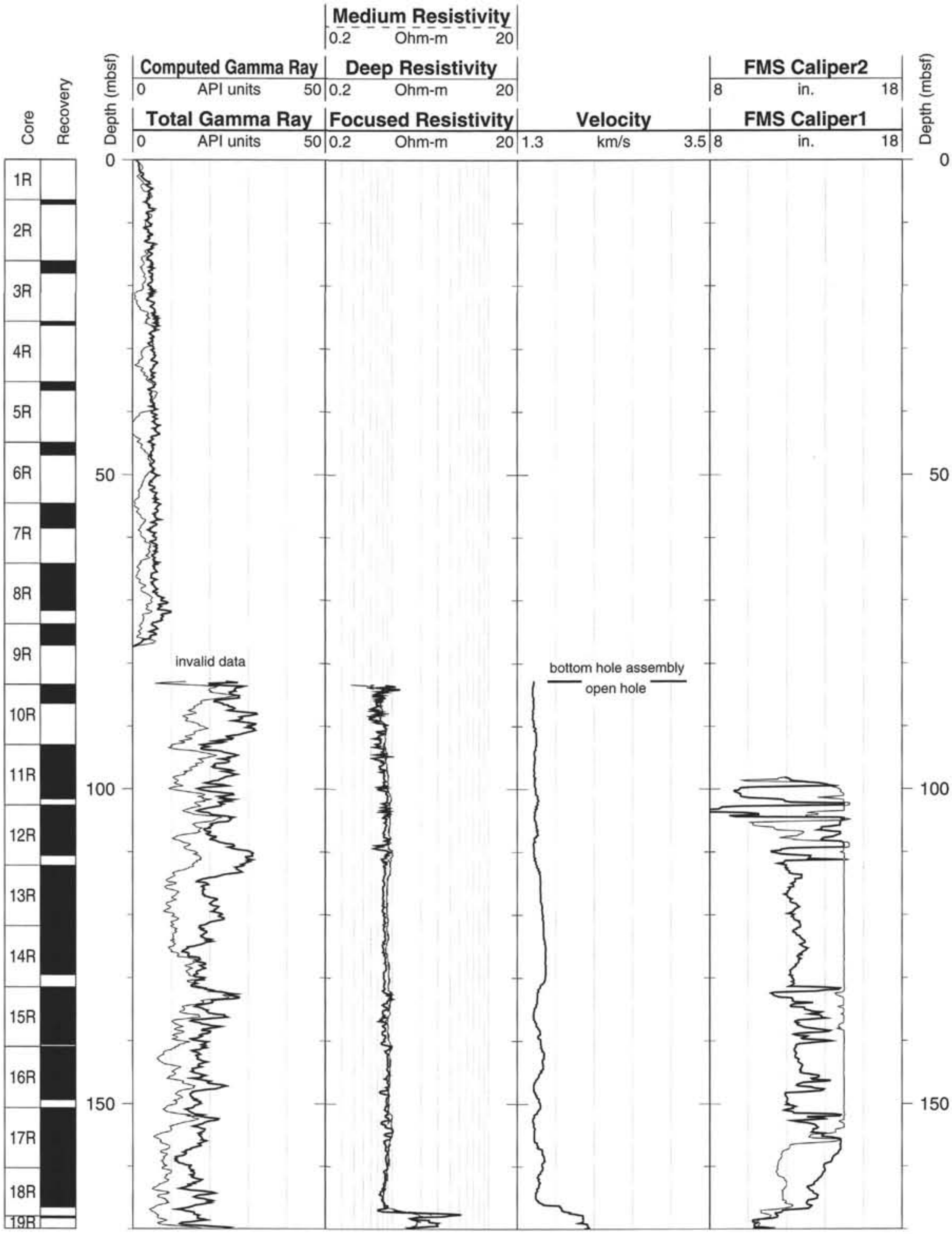

Hole 1001A: Natural Gamma Ray-Resistivity-Sonic Logging Data (cont.)

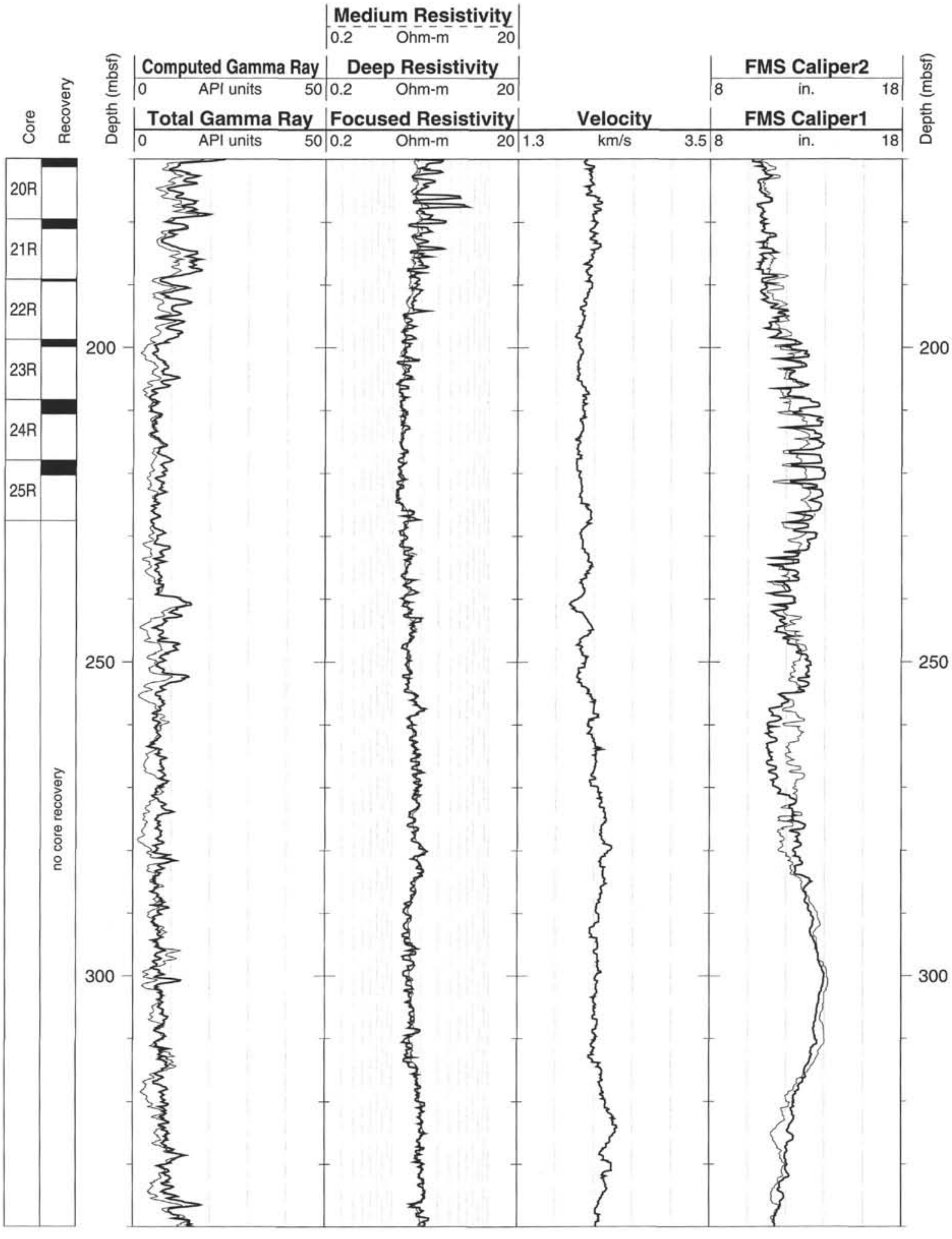

Hole 1001A: Natural Gamma Ray-Resistivity-Sonic Logging Data (cont.)